MULTIPHYSICS MODELING OF SURFACE CHARGE AND PRESSURE-DRIVEN ELECTROKINETIC FLOW IN MICRO/NANO SCALE POROUS MEDIA

A Thesis Submitted to
the Graduate School of Engineering and Sciences of
İzmir Institute of Technology
in Partial Fulfillment of the Requirements for the Degree of

DOCTOR OF PHILOSOPHY

in Mechanical Engineering

by
Tümcan ŞEN

April 2021
İZMİR

ACKNOWLEDGMENTS

I would like to express the deepest appreciation to my thesis supervisor, Assoc. Prof. Dr. Murat Barışık, for giving me the opportunity to work with him and for his guidance and persistent help throughout my studies. I am also grateful to my thesis monitoring committee members, Assoc. Prof. Dr. Ünver Özkol and Prof. Dr. Mehmet Polat for their contibutions to my studies. I would also like to thank The Scientific and Technological Research Council of Turkey (TUBITAK), for allowing us to carry out this research. This work is supported by TUBITAK under the grant number 118M710. This work was also supported by the BAGEP Award of the Science Academy.

I am also thankful to the current and former members of MinaEng research group; Onur Yenigün, Safa Sabet, Gökberk Özçelik, Fetiye Esin Yıldırım, Öykü Alan and Gülce Kalyoncu for giving me the support, courage, joy and help every single day at work. Thank you for being not just colleagues but for being real friends.

I would also like to thank my parents Nurcan and Mustafa Şen, and my sister Çılga Şen for their faith in me and supporting me for every decision I make. Without their love, I would not be the man I am today.

Last but not least, I am very grateful to my wife “Müm” for her endless care, kindness, and support. Thank you for expressing your belief in me any time I feel frustrated. Thank you for helping me to get over the hard times. I could not have done it without you.

ABSTRACT

MULTIPHYSICS MODELING OF SURFACE CHARGE AND PRESSURE-DRIVEN ELECTROKINETIC FLOW IN MICRO/NANO SCALE POROUS MEDIA

Accurate characterization of fluid transport in micro/nano confinements is essential for numerous applications from industrial, agricultural, and medical sciences. In these applications, electrokinetic interactions dominate the fluid behavior, which causes conventional fluid dynamics to become incomplete. Specifically, near-wall hydrodynamics and liquid/solid coupling at the interface varies by electrokinetic effects. Therefore, the current study focuses on characterization of the fluid transport at various porous systems and ionic conditions. The Poisson-Nernst-Planck (PNP) equations were numerically solved coupled with the Navier-Stokes (NS) equations. Charge regulation (CR) boundary condition is employed to calculate the charging behavior of the surfaces. First, the surface charging of nano-scale systems was analyzed by considering the electric double layer (EDL) overlap and inlet/outlet effects. While EDL overlap decreased the surface charge, inlet/outlet effects presented an opposite behavior. Then, transport is characterized by calculating the hydraulic conductivity from Darcy's law under electrokinetic and boundary slip effects. The results showed that electrokinetic effects decrease the hydraulic conductivity with increasing concentrations and decreasing confinement sizes. At slipping condition with a constant slip length applied, velocity slip developing on surface showed strong dependence on porosity and ionic conditions. For low porosities and high concentrations almost no-slip conditions were observed even at high slip lengths. Results showed that the transport in micro/nano-scale porous systems is dominated by electrokinetic interactions depending on porous system parameters and ionic conditions.

Keywords: Hydraulic Conductivity, Electroviscous and Viscoelectric Effects, Velocity Slip, Electric Double Layer Overlap, Inlet/outlet Effects.

ÖZET

MİKRO/NANO ÖLÇEKLERDEKİ GÖZENEKLİ YAPILARDA YÜZEY YÜKÜ VE BASINÇ TAHRİKLİ ELEKTROKİNETİK AKIŞIN ÇOKLU-FİZİK MODELLEMESİ

Mikro/nano ölçekte sıvı taşınımının doğru karakterizasyonu, endüstriyel, tarımsal ve tıbbi bilimlerde kullanılan çok sayıda uygulama için önem arz etmektedir. Bu uygulamalarda, elektrokinetik etkileşimler akışkanın davranışını önemli ölçüde etkiler ve bu da geleneksel akışkanlar dinamiği yaklaşımlarının yetersiz kalmasına neden olur. Spesifik olarak, sıvı/katı arayüzüne yakın bölgelerdeki hidrodinamik, elektrokinetik etkilere göre değişiklik gösterir. Bu nedenle, mevcut çalışma, çeşitli gözenekli sistemlerde ve çeşitli iyonik koşullarda sıvı taşınımının karakterizasyonuna odaklanmaktadır. Poisson-Nernst-Planck (PNP) denklemleri, Navier-Stokes (NS) denklemleriyle birlikte sayısal olarak çözüldü. Yüzeylerin elektrik yüklerini hesaplamak için yük düzenleme (YD) sınır koşulu kullanıldı. İlk olarak, nano ölçekli sistemlerin yüzey yükü, elektriksel çift tabaka (EÇT) çakışması ve giriş/çıkış etkileri dikkate alınarak analiz edildi. EÇT çakışması yüzey yükünü azaltırken, giriş/çıkış etkileri ters bir davranış sergilemiştir. Daha sonra, taşınım, elektrokinetik ve sınır kayması etkileri altında Darcy yasasına göre hidrolik iletkenliğin hesaplanmasıyla karakterize edildi. Sonuçlar, elektrokinetik etkilerin artan konsantrasyonlar ve azalan kanal boyutları ile hidrolik iletkenliği düşürdüğünü göstermiştir. Sabit kayma uzunluğunun uygulandığı kayma koşulunda, yüzeyde oluşan hız kayması, porozite ve iyonik koşullara güçlü bir bağımlılık göstermiştir. Düşük porozite ve yüksek konsantrasyonlar için, yüksek kayma uzunluklarında bile hemen hemen kaymama koşulları gözlenmiştir. Sonuçlar, mikro/nano ölçekte gözenekli sistemlerdeki taşınımın, gözenekli sistemin parametrelerine ve iyonik koşullara bağlı olarak gelişen elektrokinetik etkilerden büyük ölçüde etkilendiğini göstermiştir.

Anahtar kelimeler: Hidrolik İletkenlik, Elektrovizkoz ve Viskoelektrik Etkiler, Hız Kayması Sınır Koşulu, Elektriksel Çift Tabaka Çakışması, Giriş Çıkış Etkileri.

TABLE OF CONTENTS

LIST OF FIGURES

CHAPTER 1

INTRODUCTION

Accurate characterization of fluid transport in porous media is essential to understand the mechanisms of various vital applications such as groundwater treatment[1], shale gas extraction[2], storage of different energy sources[3], storage of mine and nuclear waste[4], controlling possible subsurface dispersion of hazardous contaminations[5]. Besides these large-scale biogeochemical examples, modern technology offers many promising smaller scale applications of porous systems including membrane filtration[6], electrochemomechanical energy conversion[7], gated/functionalized sensing[8], bio-imaging[9], targeted drug delivery[10] and a variety of lab-on-a-chip devices[11]. Human body also includes porous structures such as lungs and kidneys[12]. Even though all these examples are from different disciplines, common ground of all of them is that various chemical reactions originate along their flow path and fundamental changes occur in the transport.

In order the characterize the fluid transport through porous systems, there are two main methods; pore scale method (PSM) and volume average method (VAM). Although PSM yield very accurate results since every pore in the porous system is examined, it is very challenging to use this approach, especially for large domains. Therefore, VAM is mostly preferred over PSM. VAM is based the solution of governing equations in the form of volume integral and average flow parameters are calculated through these equations. The usage of VAM requires additional volume averaged parameters, such as permeability and hydraulic conductivity. These quantities are first described by Henry Darcy in 1856[13] through his experiments in sand beds. Darcy discovered that flow rate and pressure are linearly related to each other by a constant parameter, which was later named as permeability by him. Starting with his definition, various methods have been used to estimate the permeability of porous systems. For example, there are theoretical attempts to define permeability in terms of other known porous structural parameters such as porosity through Kozeny-Carman equation. This relation can only yield intrinsic permeability of a porous system. However, other complications such as chemical reactions occur inside the porous media. At micro/nano scale, these reactions change the ability of the porous media to allow fluid flow to permeate. Chemical reactions may develop as a result of the solid/liquid interactions or between different species inside the fluid. Therefore, fluid properties should also be concerned while characterizing the porous transport. In this regard, hydraulic conductivity is mostly employed, which takes fluid properties such as viscosity and density into account. Although permeability and hydraulic conductivity are very useful definitions to analyze the fluid flow through porous media, experimentally characterizing such quantities is not very easy, especially for the micro/nano scale porous systems in which many chemical reactions occur. Hence, different numerical modeling approaches have been developed along the years. For example, reactive transport models (RTMs)[5, 14] have been commonly used in the last few decades. They enable the integration of chemical reactions to the mass and energy transport in order to estimate the permeability and hydraulic conductivity that are highly dependent on these reactions.

Chemical reactions alter permeability and conductivity of the porous systems differently. For instance, structure of the porous media (i.e. intrinsic permeability) can change over the years as a result of precipitation reactions[15] or swelling of minerals within the porous structure[16] due to the reactions. On the other hand, changes in hydraulic conductivity occur due to varying flow conditions even if permeability of the system remains the same. One of the reasons for such an occurrence is the surface charge developing as a result of association/disassociation reactions at the solid/liquid interface. Surface charge creates a layer of non-homogeneously distributed ions, which is called electrical double layer (EDL). EDL and surface charge are coupled in nature, one determines the other. This behavior is mostly referred as the charge regulation (CR) nature of surface chemistry[17-19]. In the literature, there are closed form theoretical models based on Poisson-Boltzmann (PB) equation to calculate the surface charge[20] by considering the CR nature. However, for micro/nano scale porous systems, EDLs extending from opposite surfaces start overlapping and surface charge deviates from these theoretical models. Moreover, PB based models cannot resolve the axial ionic distribution in the flow conditions. In such cases, the original form of PB, which is Poisson-Nernst-Planck (PNP) equations, are employed[21, 22] coupled with the Navier-Stokes (NS) equations.

As a results of surface charge, electrokinetic effects form in a system. Basically, surface charge creates three major electrokinetic effects on the fluid flow: electroviscous, viscoelectric and velocity slip effects. Electroviscous effect forms due to streaming potential across the porous system and decreases the hydraulic conductivity[23-25] depending on fluid properties. Electroviscous effect is commonly examined in the current literature and the changes in the fluid flow due to this effect is well-resolved for different conditions. Moreover, viscoelectric effect originates due to electric field in flow normal direction created by the charged surfaces. As a result of viscoelectric effect, local viscosity at the near wall regions substantially increase and the motion of the fluid flow is retarded. Although this effect is examined by a few studies for the flows in single pores/channel[26, 27], it is completely overlooked for complex porous systems. Lastly, velocity slip is another dominant effect on the micro/nano scale porous transport. For macro-scale systems, velocity slip is almost negligible and no-slip assumption is frequently used to estimate flow characteristics. As the size of the system decreases down to micro/nano scale, such an assumption yields incorrect results. In such a case, velocity slip is commonly studied through Navier's slip boundary condition, which is a function slip length and velocity gradient at the solid/liquid interface. Both of these parameters vary as a results of surface charge. First of all, although slip length is mostly considered to be dependent only on the solid and liquid coupling, it has been verified that slip length also depends on the surface charge[28]. Moreover, the velocity gradient at the interface is strictly related to the near-wall hydrodynamics, which change due to electroviscous and viscoelectric effects. Hence, slip velocity is altered. Velocity slip and its promoting effects on the fluid flow is well-known in the current literature. More importantly, its effect on the electroviscosity is also studied by different researchers[29, 30]. However, the opposite (i.e. electroviscous effect on the slip behavior) has never been questioned. Just recently, viscoelectric effect on the velocity slip behavior was analyzed by a few studies[31, 32]. Yet, they attributed the changes to the varying slip lengths, not the velocity gradient at the solid/liquid interface. Overall, all these three effects (electroviscous, viscoelectric and velocity slip effects) can be referred as non-Newtonian effects since they create local variations in the flow, which develops different than the bulk behavior. Current literature is lack of providing a complete understanding for the coupled behavior of these effects on the porous transport.

In this regard, this study aims to fill this gap in the literature and provide a solid basis for the porous transport in micro/nano scale. Particularly, this study focuses on the characterization of surface charge in porous media and resulting electrokinetic effects such a electroviscous, viscoelectric and velocity slip effect. Furthermore, the variation in the hydraulic conductivity due to these effects are resolved. The current results will contribute the existing transport modeling studies.

The study is divided into six chapters. In the following chapter, which is Chapter 2, a comprehensive literature review on surface charge behavior in porous systems developing in the EDL overlap cases and the variations due to channel-reservoir interactions are presented along with the electroviscous, viscoelectric and velocity slip effects. In Chapter 3, theoretical background for the PNP and NS equations are introduced. The mathematical models that describe the electrokinetic effects and CR model are also discussed in this section. Moreover, the definitions of porous structural parameters and Darcy equation with permeability and hydraulic conductivity definitions are given. In Chapter 4, numerical methodologies employed in the current study and the validation process are discussed. In Chapter 5, the results of the surface charge and flow conditions developing inside different porous structures are presented and analyzed. Lastly, conclusion is presented in Chapter 6.

CHAPTER 2

LITERATURE REVIEW

In this section, the current knowledge on the micro/nano scale porous transport is thoroughly reviewed. First, the literature on the charge regulation nature of solid surfaces is examined in terms of electric double layer (EDL) overlap and channel/reservoir interactions. Then, experimental and theoretical studies on the electroviscous and viscoelectric effects resulting from charged surfaces are discussed. Additionally, the studies that focus on the hydrodynamic slip and its dependence on the near-wall hydrodynamics in relation with the electroviscous and viscoelectric effects are further analyzed. Lastly, existing works on the characterization of surface electric charge in porous media, modeling attempts of the fluid transport through charged porous systems and their deficiencies are presented.

2.1. The Electric Double Layer (EDL)

When solid surfaces come into contact with aqueous solutions, they develop surface charge as a result of association/dissociation reactions occurring at the interface[33, 34]. Charged surfaces attract counter-ions while they repel co-ions, forming electric double layer (EDL) over the surface. The ionic distribution in the EDL obeys the Boltzmann distribution (BD) and the resulting electric potential distribution over a semi-infinite charged flat surface can be estimated by the well-known Poisson-Boltzmann (PB) equation[34]. However, charged surfaces are not always isolated from other charged surfaces. For example, many nanotechnologic applications, such as DNA analyzers[35], DNA and protein transport[36], drug delivery[37, 38], biological/chemical agent detection[39, 40], micro/nano sized energy production and storage devices[41, 42], micro/nano chip sensors[43, 44], and nano-membranes[45, 46], involve nano-channels/pores that cause the EDLs forming over the opposite parallel surfaces to interact. This is referred as EDL overlap in the literature and applying Boltzmann distribution in the case of EDL overlap and solving PB equation is fundamentally incorrect[47, 48]. Moreover, surface charge is directly associated with the ionic concentration at the solid/liquid interface and the ionic concentration at the interface differs for overlapping EDL cases from the non-overlapping EDL cases, so does the surface charge. Therefore, although applying constant surface charge or electric potential for the surfaces is a common practice in existing literature, they do not properly mimic the nature of real surface charging behavior. Instead, surface charge and resulting electrical potential at the interface develop as a function of local ionic environment. This dependence of surface charge is commonly practiced by active surface charge models in the literature. The so-called "Charge Regulation (CR)" behavior of surfaces is first discovered by Ninham and Parsegian[19], then observed through force measurements by colloids[49-52] and atomic force microscopy (AFM)[53-55]. The charge regulation nature of surfaces has been implemented into numerical studies as a boundary condition by active charge models. These CR models consider the association/dissociation reactions occurring at the interface and relates the ionic conditions at the interface with surface charge through reaction constants, which are empirically determined

In the recent years, a multi-ion CR model[18, 20, 56, 57] is frequently utilized, which relates the surface charging behavior to the ionic aqueous solution properties such as pH and concentration of the solution. Some of these studies focus on the size dependent charging behavior of particles[17] and their interactions with other surfaces in the case of EDL overlap[18], concluding that the surface charge of particles varies with the degree of EDL overlap between charged surfaces. Other studies address the effect of EDL overlap and the resulting surface charge values on the flow conditions of nano-confined fluids[58-60]. Basically, the varying surface charge as a result of EDL overlap cause different effects on the flow depending on the degree of overlap. More particularly, the efficiency of energy conversion in nanofluidic channels depends on the EDL overlap and the highest efficiency is obtained when the EDLs overlap. Therefore, accurate characterization and proper treatment of surface charge in the case of EDL overlap is of prime importance for many promising applications with or without the presence of flow condition.

2.2. Ionic Interactions between Channel and Reservoir

In nanofluidics, overlapped EDLs of opposite surfaces are not the only cause of surface charge variations in a system. Many applications in nanotechnology involve diffusion of ions from large pores/channels/voids to very short and narrow pores/channels in size[61, 62]. This creates an axial variation in the ionic conditions at the inlet and outlet regions of every pore in addition to normal variations due to EDL overlap. As a result, substantial local changes in the surface charge are observed around these regions, especially for short channels. Such geometrical variations in a system also cause further complications in the flow conditions. For example, transport of ions by a pressure gradient creates an electrical potential bias across the pores/channels, which is called streaming potential. This attenuates the fluid flow in axial direction[63-65]. Moreover, hydrodynamic resistances develop as a result of concentration polarization at the inlet and outlet regions of pore/channels[66, 67].

Majority of studies in the literature, which characterize the surface charging behavior of surfaces by CR models, focus on infinitely long straight channels and tubes[47, 68-71]. However, since the surface charge locally varies at the inlet and outlet regions of finite length conduits due to axial ionic equilibrium, strong variations develop in the average surface charge of the pores/channels depending on the length, even in the absence of any flow conditions. In this context, some studies are dedicated to examine the ionic diffusion effects in axial direction for short nano-channels/pores. Such effects form due to the diffusive interactions between the reservoir and channel and they alter the local ionic conditions and surface charge inside the channels/pores as long as 2.7 times Debye length (λ), which is referred as "ionic development length"[72, 73].

In flow conditions, the channel-well interaction in axial direction is mostly studied through simultaneous solution of the Nernst-Planck (PNP) and Navier-Stokes (N-S) equations[74-76]. The length dependence of ionic current is discussed in some studies and it was concluded that shorter length channels develop weaker channel resistances causing the ionic current to increase[77, 78]. Moreover, decreasing effect of concentration polarization on the ionic current occurring at the entrance and exit regions of channels/pores is also frequently studied[75-78]. However, all the results are presented as observations without examining or describing its occurrence. Hence, there is not any proper characterization or explicit solution for the surface charge behavior of short nano-conduits that are interacting with reservoirs connected to their ends.

2.3. Electrokinetic Effects

2.3.1. Electroviscous Effect

When a pressure gradient is applied across a nano-fluidic channel, the counter ions within the EDL are also carried along the channel that causes an "***ionic/streaming current***"[22, 79]. As a result, the counter ions accumulate in downstream region creating a potential bias across the channel that is called as "***streaming potential***"[22, 79]. Resulting streaming potential creates a reserved osmotic flow, referred as "***conduction current***", opposing the pressure driven flow[22, 79]. The ionic and conduction currents behave in a coupled manner in a system such that pressure driven ionic current causes the conduction current, which in return attenuates the ionic current itself. Such a mechanism in nanofluidic systems is of fundamental importance for the above-mentioned applications and many studies are dedicated for an accurate characterization over last decade[47, 77, 80, 81]. Since the pressure driven flow decelerates as if its viscosity is higher, this effect of conduction current in nanofluidic channels has been examined through a new viscosity definition, referred as apparent viscosity. Starting with Elton[82]'s proposal to name this effect as "***electroviscous effect***" in 1948, many studies have been performed to characterize the effect of conduction current under "***electroviscosity***" concept[47, 80, 83, 84]. These studies show that electroviscosity significantly reduces the ionic transport depending on the ionic concentration and confinement heights. Therefore, researcher frequently employ the Debye-Hückel parameter (H/λ) to quantify electroviscosity effects[29, 80]. Such a characterization indicates the importance of EDL overlap on electroviscous effects since this parameter defines the degree of EDL overlap. Moreover, it has been concluded that the electroviscosity increases with wall electric potential until the zeta potential reaches a threshold above which EDL becomes thin and electroviscosity becomes negligible[64].

2.3.2. Viscoelectric Effect

Apart from the apparent increase in the viscosity of the fluid, the fluid viscosity shows actual local variations due to electrostatic interactions within the EDL caused by the surface charge. Unlike electroviscosity, this effect originates independent from any flow conditions. This was first discovered by Dood and Andrade[85], who referred such an increase in the fluid's viscosity as "***viscoelectric effect***"[86]. In 1951, Dood and Andrade originally wanted to name this phenomenon as electroviscosity, but the term was already used to describe the reduction in the flow rate due to conduction current in 1948. They modeled the local viscosity that accounts for the viscoelectric effect as[86],

$$\mu_E = \mu(1 + fE^2) \tag{2.1}$$

where μ is the bulk viscosity of liquid, E is the electric field strength normal to flow direction and f is defined as the viscoelectric coefficient. Such an effect significantly alters the ionic current and fluid flow in nanofluidic systems. Yet, this is mostly overlooked in the current literature and only a few studies tried to characterize the relation between viscoelectric effect and ionic current[26, 27], concluding that the ionic current in pressure driven flows decreases due to the viscoelectric effect.

Even though the electroviscous and viscoelectric effects are observed in flow of Newtonian fluids, both effects are categorized as non-Newtonian effects by some researchers in the literature[87] since they cause the fluid properties and dynamics near the solid walls to show variations compared to the bulk and divergence from continuum behavior.

2.4. Slip Velocity under Electrokinetic Effects

Although there is not a complete study that focus on the combined occurrence of these three major electrokinetic effects (i.e. electroviscous, viscoelectric, and axial electrokinetic development length effects), this is not a major drawback of the current literature since these effects are mostly additive to each other and their dependence on ionic and physical conditions are well explained, separately.

On the other hand, hydrodynamic slip in nano-confinements also substantially alters the fluid flow and the ionic current in addition to above-mentioned electrokinetic effects[29, 88-90]. Advanced nano-technological applications involve extremely smooth surfaces that promote slip depending on solid/liquid coupling at the interface. A number of numerical and theoretical studies concluded that hydrodynamic slip enhances the ionic transport, and increases the efficiency of ionic transport based applications such as electrokinetic energy conversion[74, 90]. More interestingly, it was also found that increased ionic current due to velocity slip results in a higher apparent viscosity (i.e. electroviscosity)[84, 91, 92]. Yet, overall flow rate and ionic current were found to still increase.

For a liquid flow, the velocity slip is most commonly modeled by the partial slip boundary condition, proposed by Navier in 1823[93] as:

$$u_{slip} = L_S \left.\frac{du}{dy}\right|_{wall} \tag{2.2}$$

where L_S is the slip length and du/dy_{wall} is the velocity gradient at the interface.

This boundary condition has been acknowledged and validated by numerous researchers showing that the continuum solutions with Navier's slip condition yields accurate flow calculations for confinements as small as 3-4 nm[28, 90, 94-98]. In above equation, slip length is mostly assumed to be a material property of the solid/liquid coupling in many systems[99-103]. In the recent MD simulations, slip length is found to be also dependent on the surface wetting and it is described as a function of the contact angle[104, 105]. Aside from these findings that are independent of the charging conditions at the interface, researchers also relate the surface electric potential to the slip length[29, 30, 106, 107]. However, according to the proposed relation, the surface electric potential should be relatively higher than the naturally developing surface charge range for such an effect to alter the slip length[108, 109]. Recent molecular dynamic (MD) simulations proved otherwise and presented substantial decrease in slip length with increasing surface charge[31, 32] even at low surface charge values.

In addition to the slip length, slip velocity also depends on the velocity gradient at the surface. This gradient is strongly coupled with the near wall hydrodynamics. Therefore, electrokinetic and viscoelectric effects within the EDL play an important role on the slip behavior at the interface. In the very recent study of Rezaei et al.[31], slip length, hence slip velocity, presents variation when the local viscosity of the fluid is considered, which different than the bulk viscosity of the fluid. According to their results, slip length estimated from the velocity gradient in the bulk is found to be decreasing, whereas slip length remains mostly constant at low surface charge values if the local velocity gradient is considered. Consequently, these studies estimated the slip velocity change as a result of the local viscosity variations in the EDL. Therefore, it is evident that the velocity slip at the surfaces of nanofluidic channels shows variations even for constant slip length and pressure gradient. Similar behavior is also observed in non-Newtonian fluids where velocity slip varies with the viscosity of the fluid near the walls depending on the applied shear rate to the solid walls[110-114]. This should not be confused with electroviscous and viscoelectric effects on the slip velocity, which is mostly overlooked by the current literature. Yet, such physics can be estimated using a Navier's slip boundary condition considering electrokinetic effect on the local hydrodynamics.

In general, electrokinetic effects are expected to become negligible when the confinement sizes increase[29, 47, 80] although they still exist. For such cases, the flow conditions can be resolved by the simple Poiseuille flow estimations. However, electroviscous and viscoelectric effects can alter the velocity slip even in wider channels where the EDL thickness is much smaller than the confinement sizes. Because the slip velocity is dependent on the conditions at the interface or at the close proximity of the interface. Therefore, although these effects are dominant even in a very limited region, they can still play an important role on the fluid flow depending on the ionic environment conditions.

2.5. Internal Surface Charge of Nano-scale Porous Media

Since the pore size has vital important for almost all of the porous structure based applications, porous systems are also categorized depending on their pore sizes in the literature. Recently, scientists draw interest towards mesoporous silica structures whose pore sizes range between 2 to 50nm. They are synthetized in a wide range of morphologies, such as spheres, discs and powders and have exceptionally ordered pore structures, high surface area and pore volume, easily tunable-sizes, chemical stability, and biocompatibility. The interconnected pore structures of mesoporous materials enable diffusion of ions into pores. Therefore, not only outer surfaces but also inner surfaces gain surface charge due to the interactions of ions in aqueous solutions and silanol groups on the internal surfaces. Yet, the current literature on the mesoporous materials mostly focus on evaluating outer surface charge variations in different ionic environments. For certain applications such as transport of mesoporous nanoparticles[115-117] or different filtration processes by mesoporous membranes[118-120], outer surface charge is of prime importance. For instance, the efficiency of many membranes is based on creating strong outer surface charge in order to reject certain ions[121, 122]. Even so, examining solely outer surface charge is insufficient. First, the surface charge and resulting electric potential developing inside the mesoporous materials directly affect the outer charging mechanisms through the pore openings[123]. Second, working principles of many existing and future projected applications are controlled by internal surface charge of mesoporous materials. Drug loading mechanisms of mesoporous nanoparticles[124], liquid transport rates of mesoporous membranes[125], improved control of sorption dynamics of vitamins[126], enzymes[127] and proteins[128] for ultrafiltration dialyzers as the artificial kidney[129]; amplified proton activities for fuel-cells[130] to overcome limited proton conductivity of current polymer membranes, increased ion diffusion for lithium ion pseudocapacitors[131] to satisfy future energy needs, advanced electrochemical sensors or chemical identifiers in vivo and in vitro for biosensors[132] are all directly related to the internal surface charge of mesoporous materials. Therefore, an accurate characterization of the internal charge properties of such materials is mandatory.

Internal surface charge density of mesoporous silica has been evaluated through experimental and theoretical methods in the literature. There are two basic experimental techniques commonly employed by the researchers. First one is based on the streaming potential measurements across the mesoporous systems by creating a pressure driven flow[133-137]. Such methodology is also used by geophysicists to analyze and map the subsurface[138-141]. The second method is to perform potentiometric titration[142-145] and then estimate the internal surface charge from the change in solution conditions as a result of adsorption/desorption of protons and ions. Most of the experimental studies analyze the effects of different types of alkaline chlorides, pH inside the porous system and internal surface potentia[136]. On the other hand, some effort has been given to characterize the effect of the porous structural parameters such as pore shape[45], pore size[134-136] and porosity[146]. It has been concluded by these studies that such parameters play an important role on the internal surface charge properties of porous systems[136]. Yet, most of these experiments serve for specific applications and the results are mostly presented as observations without explaining the underlying physics. Experimentally measuring internal surface charge of mesoporous systems is also very challenging due to both theoretical and experimental restrictions. For example, surface charge estimations through streaming potential measurements is based on the Helmholtz-Smoluchowski and the Gouy-Chapman equations that have certain restrictions and they neglect important effects such as concentration polarization[66] and electroviscosity[29], which are very dominant in highly overlapped tight mesoporous systems. Moreover, potentiometric titrations are very time-consuming and additional operations are needed such as internal surface area determinations.

Internal surface charge of mesoporous systems can also be estimated theoretically. As already discussed, closed formed solutions as a function of ionic environment conditions exist in the literature to analytically calculate surface charge and the resulting electric potential of a surface[20]. These solutions are based on Boltzmann Distribution (BD) and only valid for isolated planar surfaces, which are away from any other charged surfaces. However, mesoporous systems consist of very narrow and short conduits that are comparable with the EDL thickness in size. Therefore, strong EDL overlaps occur in the pore throats between opposing surfaces. Moreover, the ionic equilibrium between the pore voids (reservoirs) and pore throats (channels), which is referred as pore to throat connectivity, also creates additional challenges for the estimation of surface charge in porous systems. This results in divergence of surface charge from theoretical estimations as a function of pore size and porosity.

Existing theoretical attempts on mesoporous systems simplify the porous structure as a combination of infinitely long channels with no EDL overlap[133, 134, 144, 147] although they discuss the dominating effects of EDL overlap. These studies try to update flat surface CR model parameters by curve fitting the experimental results and describe the possible reasons of divergence from the flat surface charging behavior. There are also numerical studies trying to characterize the inner surface charge mechanism of mesoporous silica by using modified-PB along with CR models. Yet, they disregard the EDL overlap[144, 148] and only focus on ionic distributions/conductance[149-151] or some specific cases[152]. Therefore, a complete study on the combined effects of the pore throat EDL overlap and the so-called “pore to throat connectivity” in a mesoporous system as a function of the structural porous parameters is still missing in the current literature.

Another important issue in porous systems is the characterization of the internal structure. Although porous systems are generally characterized by porosity and pore size, these parameters are insufficient for most of the porous systems. Inside these systems, the pore voids are connected to each other through channels, which are called pore throats. These connections cause different ionic equilibrium inside the porous systems, creating connectivity effects. However, the neighboring voids are not always connected the same way. As a result, two porous systems, which have identical porosity and pore size values, can be complete different than each other depending on how these void connections form. This structural difference cause different ionic distributions to form inside mesoporous mediums depending on their pore connections. Hence, connectivity effects also vary as a function of the pore throat size to pore size ratio. This should also be considered for a correct characterization of pore network[153-155] and corresponding charging behavior.

2.6. Transport in Nano-scale Porous Media

Transport in porous media is frequently characterized by Darcy's law, which relates the mass flux to the pressure drop over a distance by volume averaged parameters, such as permeability and hydraulic conductivity. Normally, the permeability of a system is a material property, which is independent of the fluid type that is being transported. This is referred as intrinsic permeability in the literature[156-158]. Yet, the transport through most of the porous systems highly depends on the fluid type since the ionic solutions creates further effects on the transport as a function of ionic concentration in addition to the structural obstacles of the porous media. Therefore, effective/apparent permeability concept has been implemented into the Darcy's law in some studies[159]. However, hydraulic conductivity is still the most commonly employed characterization parameter for the transport of ionic fluids through porous media[24, 160, 161].

In general, estimation of permeability or hydraulic conductivity for a porous system requires experiments. However, experimentally describing these quantities especially for macro-scale systems that include complex occurrences in pore-scale is very challenging since these occurrences make it almost impossible to perform controlled experiments. Therefore, theoretical modeling approaches are commonly employed to predict the variation of permeability and conductivity as a function of different parameters such as porosity[162, 163] and ionic solution conditions[24, 25]. Being one of the well-known modeling approaches for the porous media, reactive transport models (RTMs) have been used instead of experimental methods to analyze transport through porous media at varying time and length scales. Reactive transport modeling considers diffusion, advection and dispersion along with various types of reactions occurring in porous systems. These reactions are generally classified as homogeneous and heterogeneous reactions[5, 164, 165]. Homogenous reactions occur almost instantly between different species within the aqueous environment whereas heterogeneous (surface) reactions originate due to liquid/solid interactions and they are commonly assumed to be much slower than the rate of transport[14]. In RTMs, these are incorporated into solute mass transport equation (i.e. Nernst Planck equation) as source terms[166, 167]. The effects of reactions on the transport are then analyzed through Navier-Stokes equation and Darcy's law[5]. Yet, creating such a link between the reactions and transport is not a straight-forward process.

Ultimately, these reactions alter the transport in porous systems. For example, the chemicals inside rainwater or underground water interact with the rocks or minerals in the aquifer causing chemical weathering that results in changes on the morphology and flow paths of the medium[168]. The solid/liquid coupling in the subsurface also causes clogging of the porous medium due to precipitation reactions[15] or swelling of minerals within the porous structure[16]. Such changes are very important for the propagation dynamics of various substances in Earth's crust. Many human-made applications such as long-term storage of mine or nuclear waste[166] and ground water treatment[169] as well as natural events including landslide[170] or karst formation[171] highly depend on these structural changes due to the chemical reactions.

Apart from the effects the irreversible long-term changes of the porous media's intrinsic permeability on the fluid transport, the transport can also be altered without any structural changes. In such cases, the fluid type that is being transported play a very important role. Most of the surfaces in these porous systems gain surface charge as a result of the interaction between the fluid and solid. This can affect the transport in different ways. It has been proved by many studies that permeability of the clay-rich materials considerably changes since highly negative surface charges developing in the tight pores create inaccessible pore spaces to anions[172-174]. Very recent studies on the reactive transport modeling propose that wetting dynamics of pore surfaces is also dependent on the surface charge[164, 175]. Especially, low salinity waterflooding studies report strong relation with wettability and surface charge; indicating that surface charge induces wetting characteristics of the surfaces and substantially increases in the oil recovery efficiencies at low ionic concentrations[176-178] compared to high salinity brine injection[179]. Other theoretical attempts on the porous transport examine the relation between the ionic concentration of the fluid and hydraulic conductivity of the system in terms of electrokinetic effects. The common conclusion of such studies is that conductivity of the system increases with concentration since the EDL thickness reduces for high concentrations[24, 180].

Transport modeling is essential for applications from many different fields including biochemistry, biology, geochemistry, hydrogeology and geobiology. Therefore, there are diverse range of surfaces, solutes, substances, ions, molecules, chemical reactions, pore sizes and morphologies as well as different physics that needs to be taken into account. Moreover, specific applications require different transport types to be considered. Some requires characterization of transport only by diffusion while others may need advection or even dispersion dynamics to be resolved. This creates quite a few number of combinations for the transport modeling. Consequently, starting with the pioneer reactive transport model by Yeh and Triphati,[167] RTMs have been developing for particular physics as well as the historical development with the advances in technology and knowledge level on the reactive transport through porous media[166, 168, 181-183]. Over the years, researchers have been trying to minimize the discrepancy between the modeling results and field measurements. Most of the early developed RTMs are based on averaging the transport properties over macro-scales. However, porous systems involve both geometrical and chemical heterogeneities in pore scale, which are the main reason of the discrepancies. In this context, pore scale analyses have been adapted to these transport models in the recent years[184, 185] since it is much more easier to modify the parameters and track the responses on the transport in pore scale. Moreover, pore scale porous models require less computational cost and capacity compared to macro-scale RTMs[186]. The results in pore scale are then used to accurately predict macro scale descriptions through different upscaling schemes[165, 187, 188].

One of the sources of chemical heterogeneities is the charging mechanism of solid surfaces in porous systems. First discovered by Reuss and Wiedmann[189, 190] through experiments with porous clay, surface charge varies with the local ionic conditions. Ignoring such variation cause misleading results in transport modeling analyses[191]. To incorporate this dependence of surface charge, surface complexations models are frequently used in RTMs[191-193]. It is well-known that surface charge originates due to solid/liquid interactions at the interface and it is dependent on the ionic concentration and pH of the aqueous environment. However, modeling such a phenomenon is not very easy.

Different models such as one-pK, constant capacitance, two-layer (diffuse layer/ double-layer), triple layer models exist in the literature. Although they are all based on the equilibrium at the interface, each model considers different effects. For example, two-layer model ignores the stern layer effects or constant capacitance model assumes a linear variation within the stern layer while triple layer model treats the stern layer differently that it consists of o- and β- planes over the surface. Yet, it is unnecessary to employ triple layer model where stern layer effects are negligible. Therefore, each models serve for different conditions. Since surface complexation models estimate the surface charge at local conditions, they are also able to capture the EDL overlap effects on the surface charge that are commonly encountered in the porous systems[164, 183, 191]. The ionic distribution in EDL reaches a new equilibrium and can even form co-ion repulsive channels due to overlap and alters the transport[174, 184]. Such effect is studied by coupled models that consider electrokinetic effects along with the transport.[164].

Presence of surface charge creates streaming potential[138] not only in single pores/channels but also in porous systems. Long term mineral dissolutions in the porous systems can also create streaming potential as a result of imbalance in the ionic environment[175]. Streaming potential measurements in porous media are commonly analyzed through streaming potential coupling coefficient by the geophysical researches to characterize and map the porous structure of the subsurface[138, 139]. This coefficient assesses the resulting streaming potential caused by an applied pressure gradient across a system. Similar studies exist for nano-scale channels and the flow is characterized by the ionic conductivity, which is the ratio of ionic flux and applied pressure gradient across the system[58, 194]. Such measurements also help predicting any volcanic or seismic activities[140, 141] or monitoring the underground oil and water reservoirs[141]. Electroviscous effect, resulting streaming potential in porous systems is commonly characterized by effective/apparent permeability or hydraulic conductivity definitions within the Darcy's law[159]. In the literature, it is reported that electroviscous effect decrease at high concentrations due to thinner EDL formation[24, 157, 180]. Therefore, substantial variations of apparent permeability/hydraulic conductivity values are observed due to streaming potential, which emphasizes the importance of electrokinetics in porous transport. The effect of streaming potential on the porous transport is theoretically studied in pore-scale also by using lattice Boltzmann models[191]. Such models are also used in various transport modeling attempts that couple electrokinetic phenomena with reactive transport in pore-scale[178, 187, 195].

Depending on the ionic conditions and pore dimensions, pressure driven flows can be governed by electroviscous effect. Yet, electrokinetic effects in porous media is not limited with the electroviscous effect. Viscoelectric effect also forms in the porous systems and can substantially influence the transport. Although a few studies examine its effect on single pores/channels, it is overlooked in the current literature on the porous transport. Accurately resolving these electrokinetic effects in pore scale is of fundamental importance for the macro-scale reactive transport models since the flow physics in pore scale give a great deal of indication of what happens in much larger scales. That is why, recent advances in transport modeling are towards creating hybrid models that can link the physics in different geometrical scales[185, 196].

Another important aspect of modeling the porous transport is to define correct boundary conditions for the solid/fluid interface. For example, assigning no-slip boundary condition for the fluid at the interface is a common practice in continuum hydrodynamics. This assumption works very well for macro scale porous systems but fails to describe the flow physics in micro/nano scale. At such scales, Navier-slip boundary condition[93] is employed. Ultimately, effective/apparent permeability or hydraulic conductivity will be affected from such behavior. Although velocity slip and its coupled dynamics with the electrokinetics have such a validated importance on the transport through porous media, they are poorly discussed in pore scale RTMs[175, 191], mostly through Helmholtz-Smoluchowski electroosmotic velocity[33], which is derived from Helmholtz-Smoluchowski relation[197] for thin EDL assumption and pure electroosmotic flows. Meakin and Tartakovsky[188] address the importance of implementation of Navier- slip boundary condition to the reactive transport models, they do not consider the electokinetic effects on the slip behavior that can alter the velocity slip even at relatively larger confinement sizes.

CHAPTER 3

THEORETICAL BACKGROUND AND MATHEMATICAL MODEL

3.1. Governing Equations

In order to estimate the ionic, electrical potential and velocity distributions for a system, Poisson-Nernst-Planck (PNP) and Navier-Stokes (NS) equations should be solved simultaneously since these equations are coupled. The velocity field calculated by NS equations is substituted in PNP equations to estimate convective ionic flux. On the other hand, the ionic and electrical potential distributions resulting from the PNP equations are used in NS equations to include electrokinetic effects on the fluid flow.

3.1.1. Poisson-Nernst-Planck (PNP) Equations

As a result of surface charge, electrical double layer (EDL) forms over the surfaces in which the ions are distributed non-homogeneously, as shown in Figure 3.1.

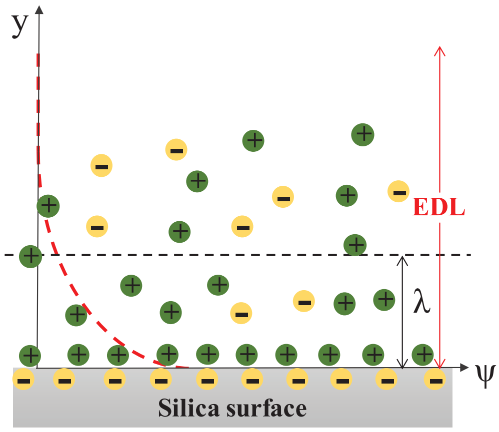

Figure 3.1. Negative electric charge of silica surfaces and electric double layer (EDL)

EDL extends over the charged surfaces until the electrokinetic potential energy becomes equal to the thermal energy[34]. In this regard, EDL can be characterized by Debye length, λ, which can be calculated as:

$$\lambda = \frac{1}{\kappa} = \sqrt{\frac{\varepsilon_0 \varepsilon_r k_B T}{N_A e^2 \sum c_i {z_i}^2}} \tag{3.1}$$

Here; κ is the Debye-Hückel parameter, ε_0 and ε_r are the permittivity of vacuum and dielectric constants of electrolyte solution, k_B is the Boltzmann constant; T is the temperature, N_A is the Avogadro constant, e is the elementary charge, c_i and z_i are the molar concentration and the valence of the i^{th} ionic specie. The current study is based on a liquid medium of a KCl electrolyte solution containing H^+, K^+, Cl^- and OH^- ions (i=1 for H^+; i=2 for K^+; i=3 for Cl^-; i=4 for OH^-), whose bulk concentrations are denoted as c_{10}, c_{20}, c_{30} and c_{40} respectively. These ions are treated as point charges throughout the whole study. In order to ensure electroneutrality condition, the bulk concentration of ions are evaluated as $c_{10} = 10^{-pH+3}$, $c_{40} = 10^{-(14-pH)+3}$, $c_{20} = c_{KCl}$ and $c_{30} = c_{KCl} + c_{10} - c_{40}$ for $pH<7$ and $c_{20} = c_{KCl} + c_{10} - c_{40}$, $c_{30} = c_{KCl}$ for $pH>7$[198, 199].

Electric potential distribution in the EDL is estimated by the Poisson equation presented in Equation 3.2.

$$-\varepsilon_0 \varepsilon_r \nabla^2 \psi = F \sum_{i=1}^{4} z_i c_i \tag{3.2}$$

where ψ is the electrical potential and F is the Faraday constant. Permittivity of vacuum and dielectric constant in this equation may vary as a function of the strength of local electric potential gradient within the double layer[200, 201] but this effect may be negligible compared to the other variations in the most of the systems.

For semi-infinite charged surfaces, the ionic distribution in EDL can be estimated by Boltzmann distribution as:

$$c_i = c_{i\infty} \exp\left(-\frac{z_i e \psi}{k_B T} \right) \tag{3.3}$$

Combination of Equations 3.2 and 3.3 yields the well-known Poisson-Boltzmann (PB) equation, given in Equation 3.4.

$$\nabla^2 \psi = -\frac{e}{\varepsilon_0 \varepsilon_r} \sum_{i=1}^{4} z_i c_{i\infty} \exp\left(-\frac{z_i e \psi}{k_B T} \right) \tag{3.4}$$

For wall potentials below ±25 mV, the PB equation can be linearized and analytically solved by employing Debye-Hückel approximation[202]. For higher potentials, solutions of non-linear PB equation utilizing complex elliptic functions exist in the literature. Yet, they require cumbersome equations to be solved[203, 204].

PB equation cannot be used for all systems, especially in the cases where EDLs of opposite surfaces start overlapping. This can be explained by Figure 3.2, in which the electric potential distributions in a channel for both overlapped and non-overlapped EDL cases are presented for different charging scenarios. First of all, the potential distribution in the case of EDL overlap significantly deviate from non-overlapping case, indicating that the ionic distribution is also different for each case. Therefore, EDL overlap cause ionic distribution to deviate from the Boltzmann distribution. In this case, using PB equation yields inaccurate results and the original form of the Poisson-Nernst-Planck (PNP) equation should be solved for a correct estimation of ionic and potential distributions, as opposed to frequently used PB equation[34, 48]. Another notable argument in this figure is the importance of using the correct boundary condition for the charged surfaces in the case of EDL overlap. In literature, either constant surface charge[205-207] or constant wall potential[64, 208, 209] boundary condition are assigned to the surfaces to solve PNP equations. However, surface charge (σ_w) and electric potential (ψ) are interdependent to each other through Equation 3.5. If constant surface charge density is applied on both surfaces (Case 1 in Figure 3.2), surface electric potential will change by EDL overlap; whereas if a constant wall potential is used (Case 2 in Figure 3.2), EDL overlap changes the surface charge density on the surface. (i.e. slope of the potential distribution at the wall).

$$-\varepsilon_0 \varepsilon_r \vec{n}.\nabla \psi = \sigma_w \tag{3.5}$$

Therefore, neither boundary condition is appropriate for charged walls and charge regulation models should be used to implement this physical response of the surface chemistry to numerical models.

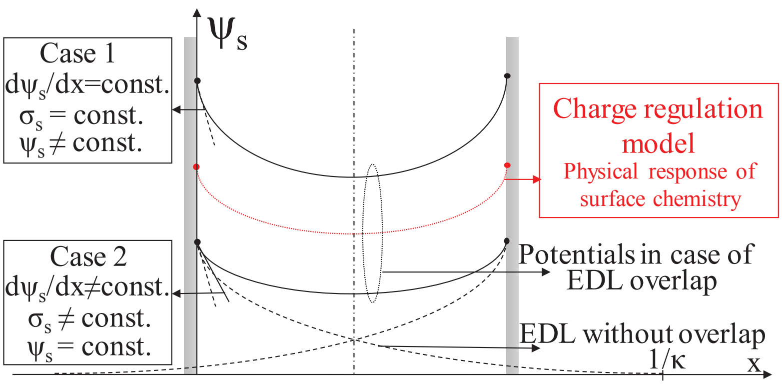

Figure 3.2. Distribution of electric potential with and without EDL overlap. In case of EDL overlap, two generally employed boundary conditions of constant surface charge (Case 1) and constant surface potential (Case 2) in comparison with charge regulation model used in this study.

Moreover, PB equation does not consider the variation of ionic environment in the flow direction[48]. For infinitely long channels, it can be safely used. However, the general form of PB equation, which is PNP equations, should be used for a correct estimation of ionic distribution and transport for channels/pore with finite lengths[21, 22]. In this regard, ionic distribution is governed by Nernst-Planck equation as shown in Equation 3.7.

$$\nabla.\vec{N}_i = \nabla.\left(-D_i \nabla c_i - z_i \frac{D_i}{RT} F c_i \nabla \psi + \vec{V} c_i \right) = 0 \tag{3.7}$$

Here, $\vec{N}_i$ is the flux density, D_i is the diffusivity, R is the universal gas constant and $\vec{V}$ is the velocity field. Combining Equation 3.2 and 3.7 yields PNP equations.

3.1.2. Navier-Stokes (NS) Equations

Assuming incompressible Newtonian fluid subjected to body forces, the velocity field in Equation 3.7 is calculated by Navier-Stokes Equations as:

$$\rho \frac{D\vec{V}}{Dt} = -\nabla p + \mu_E \nabla^2 \vec{V} + \vec{F_B} \tag{3.8}$$

where ρ is the density of the fluid, $D\vec{V}/Dt$ is the material derivative of velocity field, ∇p is the pressure gradient. μ_E and $\vec{F_B}$ are the local viscosity of the fluid and body force term, respectively. μ_E and $\vec{F_B}$ are estimated by using the ionic and electrical potential distributions resulting from the PNP equations to incorporate electrokinetic effects into NS equations, which will be explained in the following section.

3.2. Theoretical Description of the Electrokinetic Effects

3.2.1. Electroviscous Effect

As already explained, electroviscous effect originate due to streaming potential forming across the pores/channels. This effect is incorporated into numerical models through the body force term, $\overrightarrow{F_B}$, of Navier-Stokes equation as shown in Equation 3.8. Body force can be calculated from $\rho_V \, d\psi/dx$ where ρ_V is the charge density and $d\psi/dx$ is the potential variation in the flow direction. It should be noted here that the actual fluid viscosity is not altered and remains at its thermodynamic value, if only the electroviscous effects are considered (i.e. $\mu_E = \mu$).

3.2.2. Viscoelectric Effect

The viscoelectric effect is considered through μ_E in Equation 3.8. This term is calculated from Equation 2.1. The value of viscoelectric coefficient, f, in this equation has been a controversial topic since this viscosity model was first proposed. In 1950, Dood and Andrade performed experiments on polar fluids and suggested that the viscoelectric constant ranges between 1×10^{-16} m^2/V^2 and 3×10^{-16} m^2/V^2 depending on the fluid type[86]. In 1957, Hart[210] argued that this range contains an error of 25% due to Dood and Andrade's incorrect experimental procedure. In 1961, Lyklema and Overbeek[211] theoretically examined electroosmotic flows (EOF) and concluded the value of *f* to be 1.02×10^{-15} m^2/V^2, which is still the most commonly used value for *f* in the literature. However, there are many studies claiming that *f* should be lower, in the order of 10^{-17} m^2/V^2 [212, 213]. Starting with the usage of Molecular Dynamics (MD) simulations for nano-confined fluids in 2000s, studies have been performed for EOF through nano channels[201, 214] and increase in local viscosity has been observed near the charged surfaces up to 5 times of its bulk value[214]. Similarly, Qiao and Aluru[215] studied EOFs and concluded that viscosity increases near the surface as a result of the electric field normal to flow direction. In a very recent MD study by Hsu et al[27], they calculated the viscoelectric constant of 2.3×10^{-16} m^2/V^2, which is also very close to earlier experimental results of Hunter and Leyendekke[216]. Overall, the debate on the accurate value of viscoelectric constant continues within a range of 10^{-17}-10^{-15} m^2/V^2. However, such a range is very likely to include high error margins. The possible reason for this wide range of viscoelectic coefficient is because multiple mechanisms affecting local viscosity are integrated into Equation 2.1 through the viscoelectric coefficient. For instance, finite ion sizes and permittivity of the aqueous solution create charged-induced thickening near the walls. This behavior is modeled by Bazant et al.[217] through a power law equation presented in Equation 3.9 as:

$$\frac{\varepsilon_{local}}{\mu_E} = \frac{\varepsilon_b}{\mu}\left[1-\left(\frac{|\rho_v|}{\rho_{v,\max}}\right)^{\alpha}\right]^{\beta} \tag{3.9}$$

Here, α and β are the exponents as the fitting parameters to model various experimental and simulation conditions. ρ_v is the local charge density and $\rho_{v,\max}$ is the steric constraint of the Modified-Poisson-Boltzmann model proposed by Bikerman.[218] The steric constant can be calculated by ze/a^3 where z is the valance, e is the elementary charge and a is the effective size parameter related to ion diameter (d) through $a^3 = 0.83d^3$[219]. Bazant et al. proposed a hybrid model by incorparating the charged-induced thickening to the viscoelectric effect. Having concluded through MD simulations[201 214] that the variation of permitivity is negligible and selecting α=2, the final form of hybrid equation becomes:

$$\mu_E = \mu\left[1-\left(\frac{|\rho_v|}{\rho_{v,\max}}\right)^{2}\right]^{-\beta}\left(1+fE^2\right)^{\gamma} \tag{3.10}$$

In the above equation, Bazant et al. also introduced a new parameter, γ, to couple the viscoelectric effect and charge-induced thicknening. Very recently, Celebi et al.[220] employed Equation 3.10 in their MD simulations where they estimated β=4 and γ=1.6 in Debye-Huckel region, where surface charge is lower than -0.1 C/m^2.

3.3. Velocity Slip Boundary Condition

In the current study, the slip velocity is calculated by Equation 2.2. This equation models the tangential velocity at the solid/liquid interface based on the slip length and velocity gradient in normal direction to the flow. Slip length in Equation 2.2 is proven to be a material property of the solid/liquid couple by many researchers in the current literature[99, 100]. This knowledge is improved by Lyklema in 1994 by introducing the dependency of slip length on the surface charge[221]. In 2004, Joly et al.[106] proposed an equation for the charge dependent slip length through MD studies where they used the Green-Kubo relation for friction coefficient and separated the Van der Waals and Coulombic contributions on this coefficient. In 2013, Jing and Bhushan[109] concluded by their experimental studies with AFM that the formula proposed by Joly et al. is accurate. However, the proposed equation is a missing factor of *1/d* at the second term in the denominator and corrected the formula as:

$$L_S = \frac{L_{S,0}}{1+\left(1/\alpha\right)\left(\sigma d^2/e\right)^2\left(l_b/d^2\right)L_{S,0}} \tag{3.11}$$

where $L_{s,0}$ is the slip length in the absence of surface charge, α is a numerical factor (≈1), σ is the surface charge, and d is the solid molecular diameter. l_B (Bjerrum length) is the separation at which the electrostatic interaction between two elementary charges is comparable in magnitude to the thermal energy scale. Bjerrum length is defined as $l_b = e^2/\left(4\pi\varepsilon_0\varepsilon_r k_B T\right)$. In water at room temperature, the Bjerrum length can be estimated as $l_b = 0.7$ nm[106]. Equation 3.11 has been employed in many AFM studies for various surface/liquid couples[222, 223]. Equation 3.11 is used also in this study to estimate L_s in the Navier's slip boundary condition, Equation 2.2.

3.4. Multi-ion charge regulation model

Due to the protonation/deprotonation reactions occurring at the solid/liquid interface, silica surfaces present a charge-regulated behavior as a function of the ionic concentration and pH of the electrolyte solution. In order to implement this charge regulated nature into numerical models as a boundary condition, a multi-ion charge regulation model is frequently used[68, 224, 225]. For the case of silica walls, two fundamental dissociation/association reactions are considered at the solid/liquid interface as presented in Equation 3.12 and 3.13, respectively.

$$SiOH \leftrightarrow SiO^{-} + H^{+} \tag{3.12}$$

$$SiOH + H^{+} \leftrightarrow SiOH_2^{+} \tag{3.13}$$

For many systems, the relative time scales of ionic diffusion and the reactions occurring at the interface play a very important role on the distribution of ions and electrical potential in the EDL. In the literature, this relative time scales are compared by Damköhler number[33, 226], Da, presented in Equation 3.14.

$$Da = \frac{diffusion\,time}{reaction\,time} = \frac{L^2}{D\tau_{reaction}} \tag{3.14}$$

In this equation; L is the characteristic length scale, D is the diffusivity of ions and $\tau_{reaction}$ is the reaction time scale. In a system, if the reaction rate is much greater than diffusion, Damköhler number is much higher than unity (i.e. Da>>1) while if the diffusion occurs faster than reaction, Damköhler is smaller than unity (i.e. Da<<1).

The equilibrium constants of the reactions presented in Equations 3.12 and 3.13 are evaluated by using Equation 3.15.

$$K_A = \frac{\Gamma_{SiO^-}\left[H^+\right]_w}{\Gamma_{SiOH}},\ K_B = \frac{\Gamma_{SiOH_2^+}}{\Gamma_{SiOH}\left[H^+\right]_w} \tag{3.15}$$

where Γ_{SiO^-}, Γ_{SiOH} and $\Gamma_{SiOH_2^+}$ are the surface site densities of SiO^-, $SiOH$ and $SiOH_2^+$, respectively. $\left[H^+\right]_w$ is the hydrogen concentration at the solid/liquid interface. In this regard, the surface charge density of the silica walls can be evaluated as:

$$\sigma_w = -\frac{F\Gamma_{total}}{N_A}\frac{K_A - K_B\left[H^+\right]_w^2}{K_A + \left[H^+\right]_w + K_B\left[H^+\right]_w^2} \tag{3.16}$$

where Γ_{total} is the total site density of the surface.

3.5. Porous System Parameters

In order to characterize the intrinsic structure of the porous systems, porosity and pore to throat size ratio is commonly employed. First of all, porous systems are composed of voids through which the fluids pass and solid parts. Such systems is commonly modeled by representative elementary volumes (REV) in the literature[227, 228], which is shown in Figure 3.3. Assuming the aspect ratio of the solid parts as unity, the porosity (ε) of the porous system can be predicted from REV as:

$$\varepsilon = \frac{Void\ volume}{Total\ volume} = \frac{H^2 - 4a^2}{H^2} \tag{3.17}$$

where H is the size of the REV and a is the side length of the solid part.

As already discussed in the previous chapter, porous systems cannot be solely characterized by the porosity. They can have a completely different structure depending on the ratio of the pore size to the throat size. In this context, pore connectivity (R_{pt}) of the REV presented in in Figure 3.3 can be calculated as:

$$R_{pt} = \frac{Pore\,size}{Throat\,size} = \frac{H}{t} \tag{3.18}$$

Here, t represents the throat size, which can vary. Accordingly, R_{pt} takes different values.

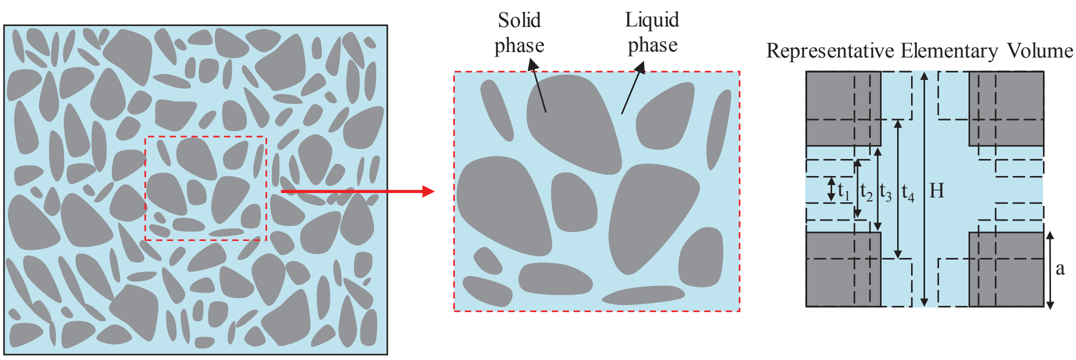

Figure 3.3. Illustration of a porous system and throat size (t) variation at a given pore size (H) and porosity (ε).

3.6. Theoretical Description of the Transport in Porous Media

Characterizing the fluid transport in porous systems are very complex due to heterogeneities in the porous structures, which cause challenges for the estimation of velocity, pressure and temperature distributions. Therefore, volume average method (VAM)[229] is frequently employed by the researchers to overcome the difficulties in solving governing equations for the porous systems. Although VAM equations are easier to solve, additional terms arise in these equations. VAM equations are frequently estimated by using representative elementary volume (REV), which is the smallest volume that can represent the whole porous system.

Darcy's law, which is employed to characterize the transport through the porous system, is also based on the VAM. According to Darcy's law, the pressure drop across a system and the flow are directly proportional to each other via a constant called permeability. Permeability is an intrinsic property of the porous medium, which is independent from the fluid properties[230]. However, the transport in the porous media may also be altered by earlier-mentioned electrokinetic effects, which are strictly related to the fluid properties. In such cases, permeability become insufficient to characterize the transport and hydraulic conductivity is mostly employed.

To estimate the permeability and hydraulic conductivity, Darcy velocity and pressure gradient in the flow direction should first be calculated. In order to calculate these quantities, the representative elementary volume in Figure 3.4 is used.

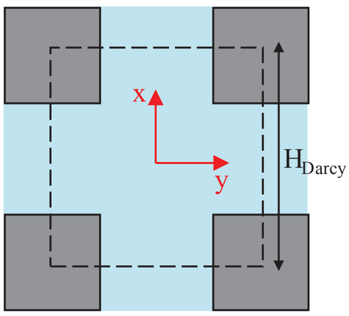

Figure 3.4. Representative elementary volume for the calculation of permeability and hydraulic conductivity

Darcy velocity and pressure gradient for the REV in Figure 3.4 can be evaluated as:

$$\left\langle u_f \right\rangle = \frac{1}{H_{Darcy}{}^2} \int_{-H_{Darcy}/2}^{H_{Darcy}/2} \int_{-H_{Darcy}/2}^{H_{Darcy}/2} u dx dy \tag{3.19}$$

$$-\frac{d\left\langle p_f \right\rangle}{dx} = \frac{1}{H_{Darcy}{}^2} \left[\int_{-H_{Darcy}/2}^{H_{Darcy}/2} p_{x=-H_{Darcy}/2} dy - \int_{-H_{Darcy}/2}^{H_{Darcy}/2} p_{x=H_{Darcy}/2} dy \right] \tag{3.20}$$

Then, the permeability (K) and hydraulic conductivity (k) can be obtained by Darcy's law through Equations 3.21 and 3.22.

$$\left\langle u_f \right\rangle = -\frac{K}{\mu} \frac{d\left\langle p_f \right\rangle}{dx} \tag{3.21}$$

$$\left\langle u_f \right\rangle = -\frac{k}{\rho_f g} \frac{d\left\langle p_f \right\rangle}{dx} \tag{3.22}$$

CHAPTER 4

NUMERICAL METHOD AND VALIDATION

4.1. Silica nano-channels/pores

In the current study, first the ionic and electrical potential distributions in a slit like silica nano channel, which is connected to reservoirs at both ends, are calculated at stationary state. Symmetry boundary conditions are applied to the sides of the reservoirs and the length of the reservoirs are determined to be sufficiently larger than the channel height so that bulk conditions are achieved at the ends. The resulting numerical domain is illustrated in Figure 4.1. Liquid phase is a KCl (*i.e.* symmetric 1:1) aqueous electrolyte solution consisting of 4 types of ionic species namely; H^+, K^+, Cl^- and OH^- ions.

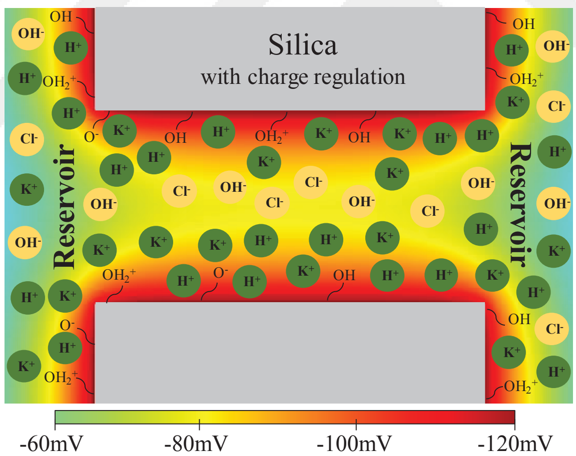

Figure 4.1. Ionic distribution of four different ionic species in silica nano-channels connected to reservoirs at both ends.

PNP equations in 2-D cartesian coordinates are numerically solved by finite element method with COMSOL Multiphysics. To solve these equations, concentrations of ionic species are maintained at their bulk values (*i.e.* $c_i = c_{i0}$) at far ends of the nano-channel and all the reservoir walls are grounded (*i.e.* $\psi = 0$), slip free (*i.e.* $u = v = 0$). No flux of ionic species is allowed through the nano-channel walls (*i.e.* $-n.\vec{N}_i = 0$) and multi-ion charge regulation model presented in Equation 3.16 is applied to the channel walls.

The constants and parameters used in the simulations are taken as: $\varepsilon_0\varepsilon_r$=7.08x10^{-10} F/m, R=8.31 J/(mol·K), F=96485 C/mol, $T=300$ K. The charge regulation parameters are chosen as N_{total}=4.816 sites/nm^2 , $pK_A=-\log K_A$=7, and $pK_B=-\log K_B$=1.9, which are very similar to ones reported in literature in a range of N_{total}=4.6-4.9 sites/nm^2, pK_A=6.3-7.4 and pK_B =0-3 by many studies[194, 231-233]. Moreover, the diffusivities of H^+, K^+, Cl^- and OH^- ions are set to be 9.31x10^{-9}, 1.957x10^{-9}, 2.032x10^{-9} and 5.3x10^{-9} m^2/s, respectively. It should be noted here that these constants and paremeters are used throughout the whole study.

For validation purposes, results of KCl concentrations of 10 mM and 100 mM are compared with the flat surface approximate analytical model proposed by Yeh et.al[20]. In these high concentration cases, EDL fields do not overlap and the resulting surface charge density values can be described by the solution of PB. Figure 4.2 shows the surface charge density values for pH range from 3 to 9. The increasing trend of surface charge density with pH and KCl concentration can easily be distinguished in the figure. The current model (markers) yields identical results with the theory (lines).

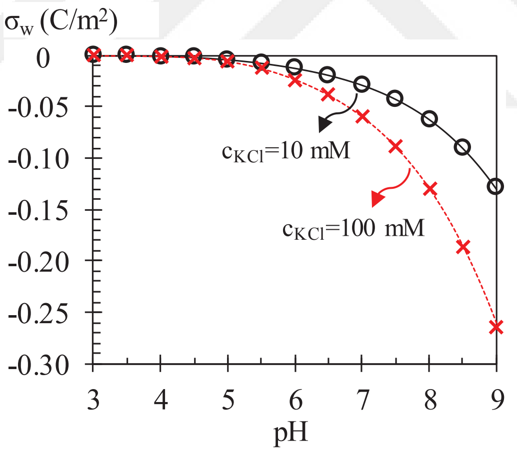

Figure 4.2. Surface charge densities of channel walls. Lines indicate the theoretical results while the markers are the results of the numerical model.

Next, for the same domain presented in Figure 4.1, a fluid flow is created by applying different pressures (i.e. $-\nabla p$) from the opposing reservoirs as shown in Figure 4.2. The channel walls gain a surface charge of σ_w, where $-\varepsilon_0\varepsilon_r\, d\psi/dy=\sigma_w$ and velocity slip boundary condition (i.e. $u=u_{slip}$) is applied on the channel walls. The corresponding ionic, electrical potential and velocity distributions are obtained by solving the PNP and Navier-Stokes (NS) equations simultaneously. For this case where the fluid transport is also considered, the reactions at the solid/liquid interface are assumed to be instantaneous and occur much faster than the transport of ions, which is a consistent assumption since Damkohler number in the current system is greater than 1 (Da>>1).

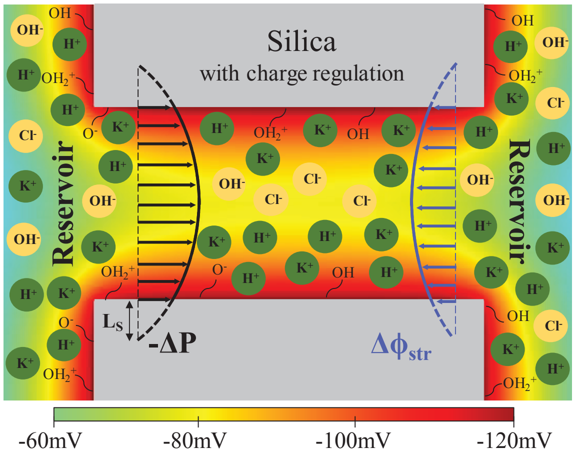

Figure 4.3. Pressure driven fluid flow in silica non-channels connected to reservoirs at both ends

Solution systematic in the flow conditions is validated by the analytical solution from Mei et al.[58] who developed closed form solution for ionic current, starting from non-linear Poisson Boltzmann (PB) and Navier Stokes (NS) equations by considering charge regulation nature of surfaces. Mei et al. simply considers a fundamental system at equilibrium of ionic current, streaming potential and conduction current. Using the current numerical model, a channel with 10nm height and 300nm length is simulated at the conditions employed in the study of Mei et al. It should be noted here that the analytical solution from Mei et al. had no channel length dependence. Hence, 300nm length channel is simulated here, which was found long enough to develop length independent results. Furthermore, both viscoelectric and velocity slip effects are not included in the solution of Mei et al. Therefore, viscosity is kept constant independent from ionic solution conditions and no-slip boundary condition is used on surfaces as $L_{s,0}$=0 for validation simulations. Consequently, only electroviscous effects are considered to validate the current numerical model with the solution of Mei et al. In Figure 4.4(a), the volume charge density and velocity profile results of our model are compared for half of the channel with analytical solution of Mei et al. for 0.1mM salt concentration, *pH* 7.5 and pressure gradient of 20 Pa/nm. Using the ionic distributions and velocity profiles, ionic currents at different ion concentrations of 0.001mM, 0.01mM, 0.1mM, 1mM, 10mM and 100mM are calculated using Equation 4.1.

$$I = 2w \int_0^{h/2} \rho_V(y) u(y) dy \tag{4.1}$$

where $\rho_V(y)$ is the volume charge density in y-direction and $u(y)$ is the velocity in y-direction. Comparison of current simulation results with the results of Mei et al. given in Figure 4.4(b) showed also good agreement.

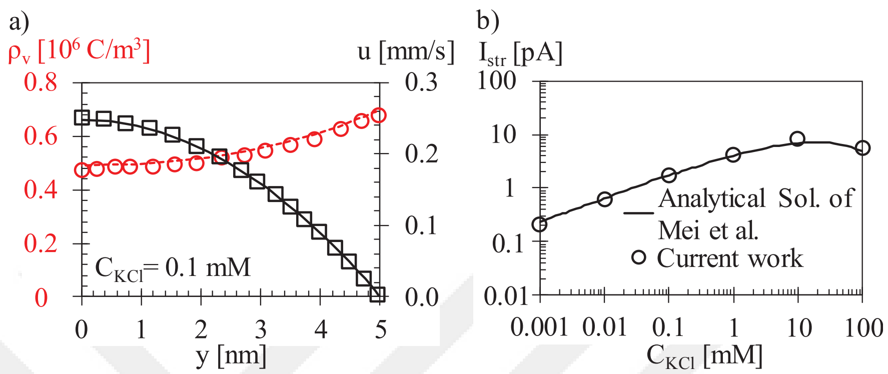

Figure 4.4. Comparison of the current simulation results of (a) velocity and ionic distribution in the channel at 0.1mM salt concentration, and (b) developed ionic currents at varying salt concentration with the analytical solution of Mei et al. Solid lines are the solution of Mei et al. while the markers represent the results of our model.

After validating the current model, another important issue is to determine the viscoelectric coefficient, f. In the current study, Equation 3.10 is adopted with parameters calculated from the MD simulations[217, 220]. In this context, the different mechanisms in the system is incorporated into the single parameter, f, in the Equation 2.1, similar to earlier literature. In order to confirm such a method, PNP equations are solved for a 10 nm height channel at 10 mM salt concentration. In Figure 4.5, local viscosity estimated by Equation 3.10 using corresponding parameters from the MD results[32, 217] (d=0.4 nm, β=4 and γ=1.6) is presented with the most common f=1×10^{-15} m^2/V^2 [211] . In the same figure, local viscosity calculated by Equation 2.1 with f=3×10^{-15} m^2/V^2 is also presented. Consequently, it is found that finite-size ion effects can be indirectly incorporated into viscoelectric model (i.e. Equation 2.1) with f=3×10^{-15} m^2/V^2, which is the value used in the current study.

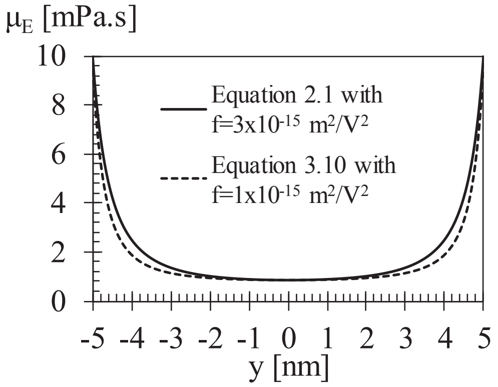

Figure 4.5. Comparison of local viscosity variation calculated by viscoelectric model (Equation 2.1) with f=3×10^{-15} m^2/V^2 and the hybrid model (Equation 3.10) f=1×10^{-15} m^2/V^2.

4.2. Mesoporous silica

Since their discovery, mesoporous silica has been synthesized in various morphologies by different research groups. MCM (Mobil Composition of Matter)[234, 235], KIT (Korea Institute of Technology)[236], SBA (Santa Barbara Amorphous)[237, 238], and FDU (Fudan University in Shanghai)[239] are the most common types of mesoporous silica. These mesoporous structures can be synthesized to have different internal structures by varying the synthesis conditions. For example, MCM-41 (hexagonal), MCM-48 (cubic), MCM-50 (lamellar), KIT-5 (cubic cage-structures), KIT-6 (cubic), SBA-1 (cubic), SBA-11 (cubic), SBA-12 (3D hexagonal network), SBA-14 (lamellar), SBA-15 (2D hexagonal), SBA-16 (cubic cage-structured), FDU-1 (cubic), and FDU-12 (cubic) are just a few example of the different mesoporous families with different structures.

In the recent years, cubic type mesoporous silica has been widely used due to their easily tunable pore and throat sizes. These parameters are mostly controlled by the synthesis conditions. For example, ordered periodic pore arrays of SBA-16 can be modified to have the required pore diameter and pore throat size by changing the temperature and time of the synthesis[240]. Therefore, the surface charge characterization of such a mesoporous system is performed in the current study.

In this context, a simple unit cell description of SBA-16 (Im3m) is presented in Figure 4.6(a), which is similar to the structure obtained by electron crystallography[241] and also by similar studies[242-245]. The variation of pore throat size in SBA-16 synthesis described in the study of Kim et al.[240] is also illustrated in Figure 4.6(a). In the current study, this mesoporous silica is modeled with a simplified two-dimensional geometry as in Figure 4.6(b) to reduce the computational cost.

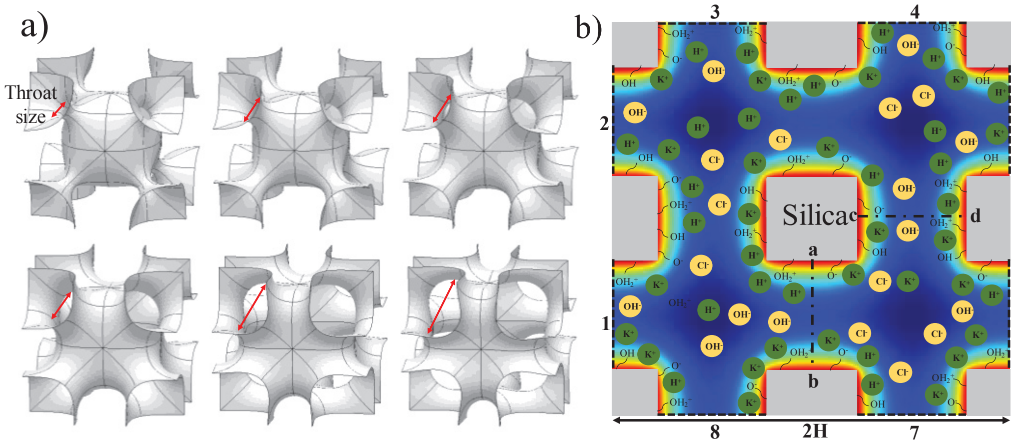

Figure 4.6. a) Three-dimensional cubic-cage structure of SBA-16 (Im3m)[242-245] at various throat sizes[240]. Structures developed by using Surface Evolver[246] b) Schematic illustration of the representative elementary volume for four-unit cells. Here H is the pore size, ab and cd lines denote the cross sections whose electric potential and ionic distributions are used in the iteration procedure.

The two-dimensional representative volume (REV) in Figure 4.6(b) shows four-unit cells of a highly ordered three-dimensional close-packed and cage-like structured mesoporous silica. The pore size of this system is indicated by H in the figure. The ionic and potential distributions are calculated by an iterative method. In the first iteration, bulk conditions are assigned to boundaries numbered from 1 to 8. Then, the electric potential and ionic concentration distributions developing at “ab” and “cd” lines are obtained from the solution of PNP equations with CR boundary condition at the solid surfaces and used as the boundary condition of outer boundaries (numbered as 1 -8) of the next iteration. This procedure is repeated until the ionic and electrical potential distributions measured at internal center lines becomes equal to distributions assigned to outer boundaries.

In order to characterize the fluid transport through a porous media as in Figure 4.7(a) is modeled by the system illustrated in Figure 4.7(b). It should be noted here that the porous system is connected to the reservoirs at both ends for a more accurate characterization of the real porous systems. PNP and NS equations are solved to obtained the ionic, electrical potential and velocity distributions. Pressure bias is applied across the systems to create the flow. Symmetry boundary condition is assigned for all the unknowns at the top and bottom boundaries of the domain so that the porous system in Figure 4.7(b) represents a larger porous media.

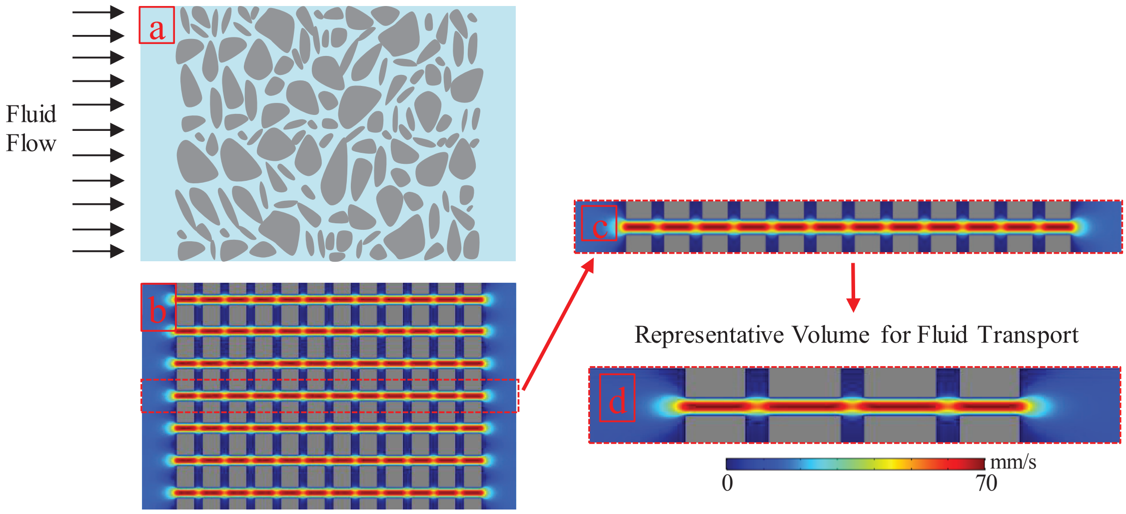

Figure 4.7. Schematic representation of the porous media connected to reservoirs at both ends

In order to characterize the transport in porous media by Darcy's law, its applicability needs to be checked first. According to Darcy's law, Reynolds number ($\mathrm{Re} = \left[\rho \left\langle V_{Darcy} \right\rangle H_{Darcy}\right] / \mu)$ should be sufficiently small (i.e. Re<1) and non-dimensionless pressure presented in Equation 4.2 should be independent from the Reynolds number.

$$\Delta P^* = \frac{H_{Darcy}^2 \Delta P}{\mu V_{Darcy} \Delta x} \tag{4.2}$$

Estimated non-dimensional pressures as a function of Reynolds number for the pressure driven flow for ΔP of 0.2, 0.4, 0.8, 1, 1.5 and 2 bar applied across the reservoirs with and without electrokinetic effects are presented in Figure 4.8(a) for porosity value of 0.5. The results show that dimensionless pressures remain constant for both conditions as Reynolds number increases. Consequently, Darcy's law is applicable for the current system.

Next, the current model and calculation methodology are validated by comparing the dimensionless permeability values of the current model by using Equation 4.3 and available data in the literature[228, 247]. The current study focuses on the liquid flow while available dimensionless permeability values are for the gas flows. However, since Darcy's law is valid both for liquid and gas flows, the current model is solved by using gas properties for validation purposes only. The comparison is presented in Figure 4.8(b) where a perfect match is obtained.

$$K^* = \frac{K}{H_{Darcy}^2} \tag{4.3}$$

Another important issue in numerical modeling is to reduce the computational cost as much as possible. Therefore, the domain in Figure 4.7(b) is further simplified to representative volume illustrated in Figure 4.7(d). While doing so, the domain in Figure 4.7(b) is first simplified to the form in Figure 4.7(c) then to the final form in Figure 4.7(d). Resulting dimensionless permeability values in Figure 4.8(b) prove that such simplification does not cause significant changes, which allows the transport through porous media in the current study to be estimated by using the domain in Figure 4.7(d).

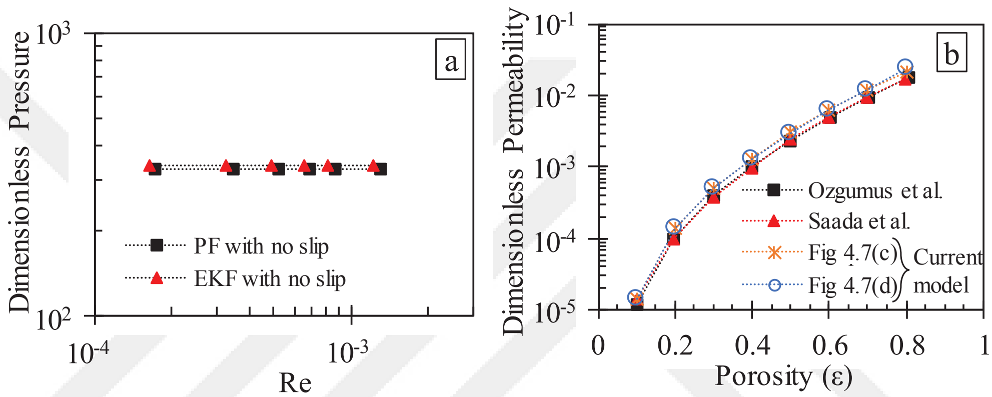

Figure 4.8. Pressure driven fluid flow in silica non-channels connected to reservoirs at both ends

4.3. The Mesh Structure of the Fluid Domain

In order to make sure the fluid domain is composed of sufficient number of elements, the simulation results of the current study are compared with the existing analytical and theoretical estimations as in Figures 4.2, 4.4 and 4.8. The number of elements is increased until the simulation results match with those of analytical and theoretical estimations. It should be noted here that inclusion of different physics requires higher mesh density in the fluid domain. For example, the highest mesh density used in the current study is 40#/nm^2 for no flow conditions and 50#/nm^2 for the flow conditions. Since, surface charge density, electrokinetic effects and velocity slip originate near the solid surfaces, boundary layer elements are created in those near-wall regions and highly structured mesh is used for the rest of the fluid domain as seen in Figure 4.9.

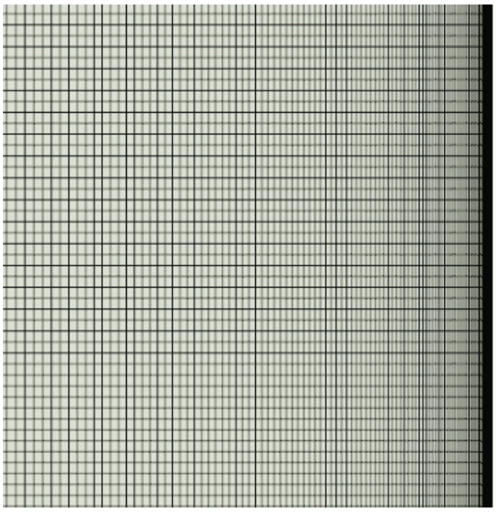

Figure 4.9. Ordered mesh structure of the fluid domain with boundary layer meshing near the walls

CHAPTER 5

RESULTS AND DISCUSSION

5.1. Surface Charge of Silica Nano-channels/pores

The initial step of the current study is to resolve the ionic distribution inside a slit-like silica nano-channel that is connected to reservoir at both ends. First, ionic and electric potential distribution inside a 10nm height and 30nm length nano-channel are estimated. Resulting electric potential contours inside the channel and around the inlet/outlet regions of the channel are presented in Figure 5.1 for salt concentrations of 1mM, 10mM and 100mM, which corresponds to λ/H ratios of 3 nm, 1 nm and 0.1 nm, respectively at pH=4, 6, and 8. Here, H represents the half channel thickness and the degree of EDL overlap is characterized by the non-dimensional number, λ/H. Higher this number is, higher the EDL overlap in the channel. For low EDL thicknesses (*i.e.*, λ/H<<1), ionic distribution and the electric potential reach the reservoir bulk values at the channel center away from the inlet/outlet. As the EDL thickness increases, ionic conditions at the channel center start deviating from the reservoir conditions. Here, two different mechanisms determine these variation: overlapping of EDLs of the opposing surfaces inside the channel and diffusion of ions from reservoir to the channel around the inlet/outlet regions. Second mechanism also induces curvature effects at the corners of the channel ends, which will be further discussed later.

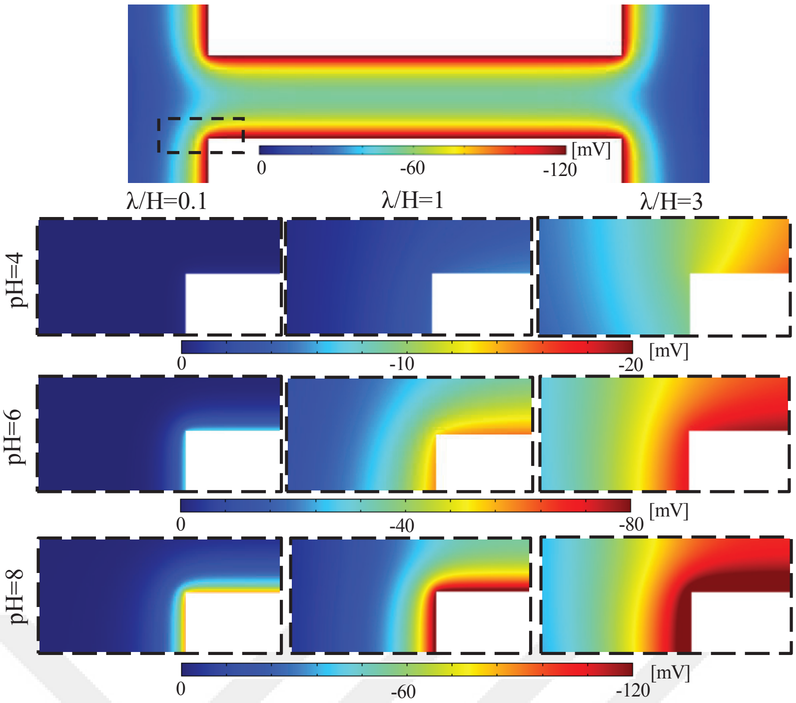

Figure 5.1. Electric potential distribution for different pH and overlapping ratios

As a second step, the local surface charge on the channel surface from the inlet until the channel center (i.e. L=15 nm) is calculated. Results presented in Figure 5.2 show that surface charge varies as a function of overlap ratio and pH due to different ionic concentrations, hence overlap ratios, developing inside the channel. For example, surface charge is almost constant for low values of λ/H, except at the very inlet region of the channel. With the increase of λ/H, this entrance effect further penetrates into the channel and even reaches to middle of the channel for λ/H=1 and 3 at pH=4 and 6. Overall, local surface charge shows an unusual behavior along the channel wall with increasing EDL thickness and a "developing region" forms at both ends of the channel.

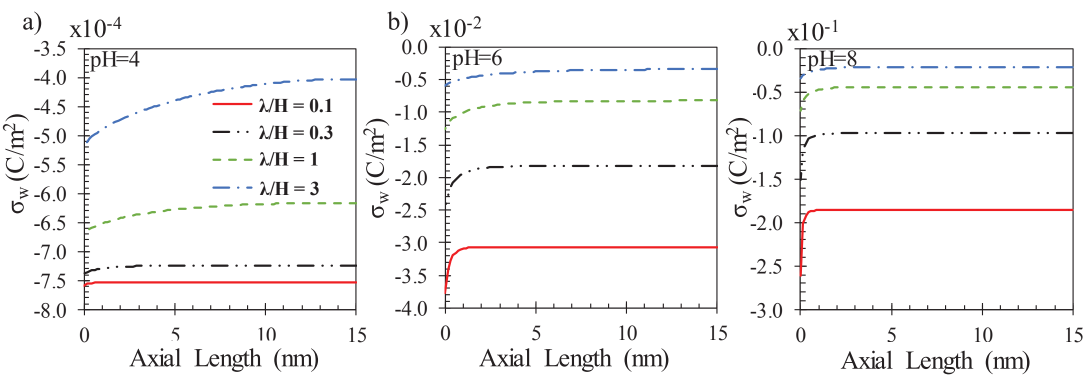

Figure 5.2. Electric potential distribution for different pH and overlapping ratios a) pH=4, b) pH=6, c) pH=8.

To characterize the developing regions, further simulations are performed at different channel lengths. In Figure 5.3, surface charge density values at the mid-length of different length channels normalized with the theoretical estimations at the corresponding concentration and pH values are presented. Results show that the theoretical estimations for the flat surface can successfully predict the nanochannel surface charge at the middle location of the channel for λ/H values of 0.1 and 0.3, which can be regarded as low EDL overlap. Yet, as the overlap ratio increases, significant variations from the theory are observed and lower surface charge develops compared to theoretical estimations. Furthermore, entrance effects become dominant for high overlap ratios and local surface charge along the channel walls cannot reach its equilibrium value even for channel lengths of 50-100 nm, especially at low pH values. Consequently, the effects of the developing region become more significant with increasing EDL thicknesses at low pH values.

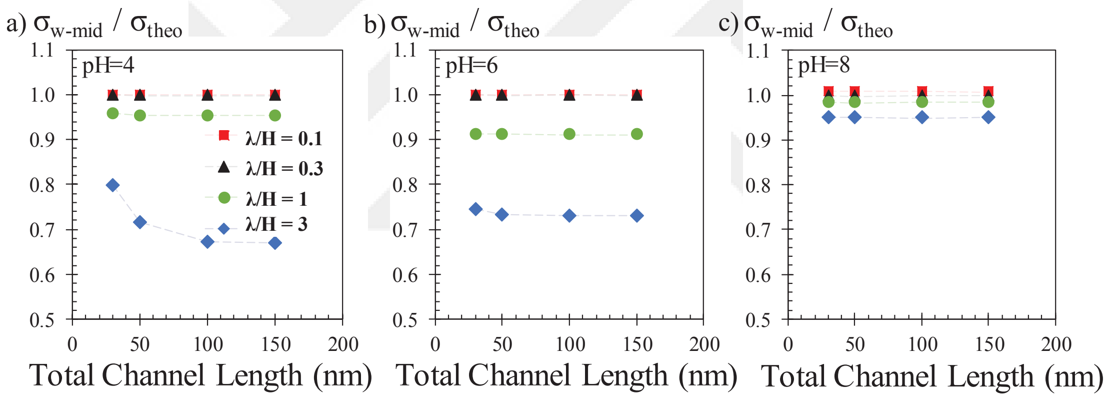

Figure 5.3. Silica surface charge density measured at the middle length of the different length channels. Charge values are normalized with the theoretical calculations for a flat surface.

Based on the conclusion obtained from Figure 5.3, a channel length of 100 nm is used from this point on to make sure that equilibrium of ionic conditions is obtained at least in the mid-length of the channel. For this channel length, local surface charges along the channel wall normalized by the equilibrium charge value (σ_{bulk}) of the corresponding channel are evaluated. They are presented as a function of normalized axial location with the EDL thickness in Figure 5.4 in order to characterize the length scale of the developing region. Except at pH=4, overlap ratio does not cause significantly changes in the developing regions at certain pH values. Yet, significantly higher surface charge values originate at the developing region, which directly affects the average surface charge of the channel.

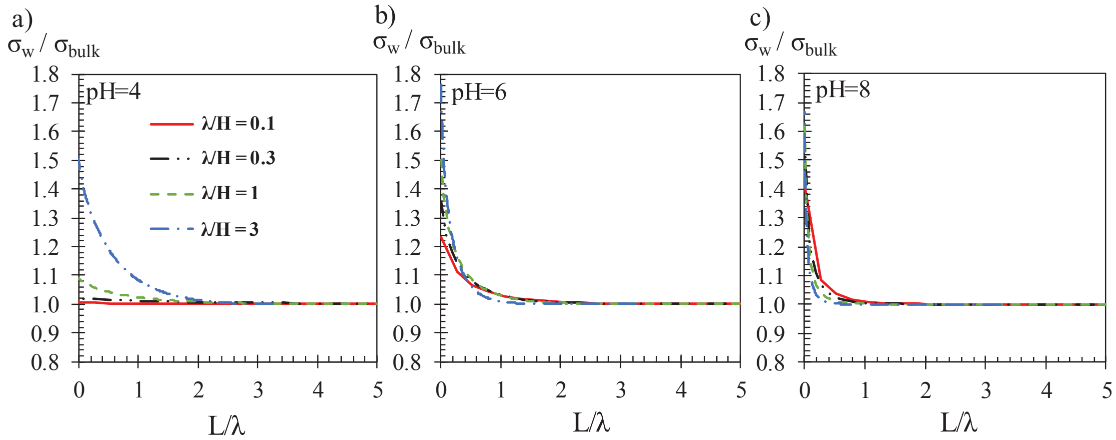

Figure 5.4. Normalized charge density along channel length normalized with Debye length (λ).

As a analogy to the boundary layer in hydrodynamics, the developing length (L_e) is defined where the σ/σ_{bulk} becomes 0.99. In this context, L_e/λ for different λ/H values are presented in Figure 5.5 for different pH values. As a result of this normalization, Figure 5.5 shows solely EDL overlap effect, not the effect of EDL thickness on the developing region. Overall, L_e mainly decreases as the overlap and pH increase. The highest L_e is estimated as 2.7 λ.

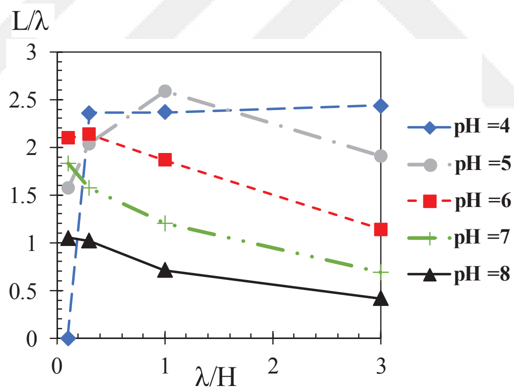

Figure 5.5. Entrance length values normalized by Debye length (λ) of different overlapping cases for different pH values.

In order to develop a model that yields the average surface charge of a nano-channel, the deviations of average surface charge from the theoretical estimations as a function channel height and length, ionic concentration and pH are calculated. This way, the existing theory can be updated in a form that consider the effect of EDL overlap and developing region. For such a purpose, the modeling attempt is separately performed for the developing region and the developed region. Initially, a value for L_e is determined to characterize the average surface charge in the developing region. As depicted from Figure 5.5 that L_e ranges between 0.2λ and 2.7λ. However, the variation is hard to formulate. Therefore, the maximum value of L_e (i.e. 2.7λ) is used as the developing length to include the effects of the developing region for all the cases. Consequently, the final model will be composed of two different models that are developed before and after 2.7λ.

In the developing region, two different mechanisms exist. First, corner effects develop due to curvature at the corners that connect the channel to the reservoirs. Such effect is observed also in other studies where similar curvature effect develops at mesoporous supercapacitors and the ionic conditions diverge from planar surface estimations as the pore size decreases[42, 248, 249]. Second mechanism forms due to the new ionic equilibrium between the developing region inside the channel and the reservoir. However, this effect becomes important only in the cases of strong EDL overlap that causes center ion distribution to become different than the reservoir value. Therefore, these two effects should be distinguished from each other.

As a first step, local surface charge values developing on a simple corner geometry is calculated at varying concentrations and pH to resolve corner effects. The electric potential contour and the illustration presented in Figure 5.6(a) clearly show the corner effect. Moreover, normalized surface charge values for different EDL thicknesses and pH values are given in Figure 5.6(b), (c) and (d). It can be seen that normalized surface charge values almost double in magnitude towards the edges. A very similar occurrence is also observed in nano-particles where the surface charge increases as the particle size decreases[17]. Surface charge reaches its theoretical value away from edges, as predicted. This behavior is limited in a region as long as 2λ. Yet, $L_e = 2.7\lambda$ is employed to be consistent with the developing region length measured earlier.

Next, the corner effects are excluded from the surface charge estimations in developing region by removing the surface charge variations in 5.6(b), (c) and (d) from the results presented in Figure 5.4(a), (b) and (c). The resulting variations of surface charge are depicted in Figure 5.6(e), (f) and (g) where only the effect of channel/reservoir interactions are seen. For example, when λ=0.5 nm in a 10 nm height channel, the overlap ratio, λ/H, becomes 0.1, which means there is no EDL overlap effect in the channel. After removing the corner effect for these conditions, it can be seen in Figure 5.6(e) that the surface charge can be estimated by the flat surface theory. However, this is not the case for Figure 5.6(g) where λ=15 nm and strong EDL overlap results in surface charge values to be lower than the theory. Even after corner effects are removed for this case, there is still a slight variation in the developing length. This behavior is caused by the channel/reservoir interactions resulting due to the different ionic conditions at the mid-length location and reservoir.

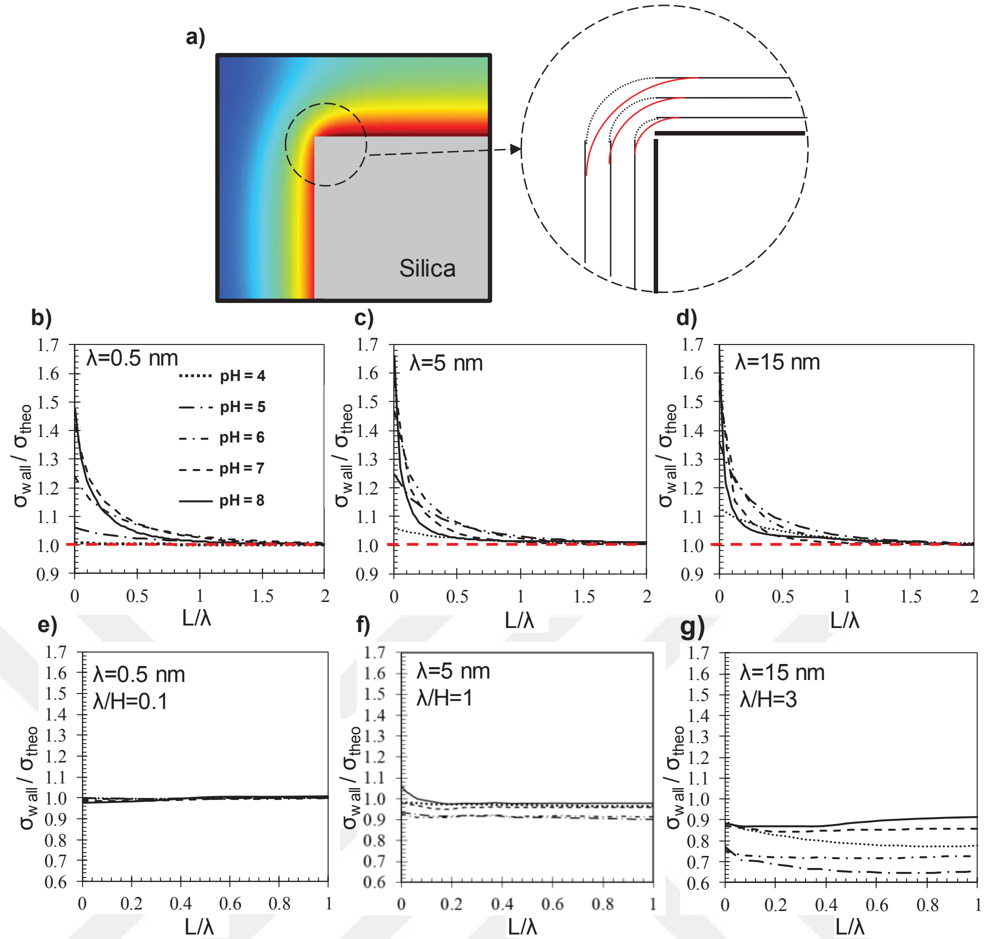

Figure 5.6. (a) Variation of local ionic concentration at a corner and illustration of curvature effects. Normalized surface charge distributions (b), (c) and (d) on a corner at different EDL thicknesses and pH values, and (e), (f) and (g) in the developing region of a 10nm height channel after corresponding corner effects removed.

Having been characterized the EDL, developing length, corner effects, the average surface charge values are calculated for each of these mechanisms inside their own length extends. Therefore, an average charge is estimated for a length of 2.7λ on the corner ($\sigma_{corner-ave}$) by Equation 5.1. Similarly, an average charge for the developing region ($\sigma_{developing-ave}$) is calculated by Equation 5.2. Lastly, an average for the region after 2.7λ until mid-channel length ($\sigma_{developed}$) is calculated by Equation 5.3.

$$\sigma_{corner-ave} = \frac{1}{2.7\times\lambda}\int_0^{2.7\times\lambda} \sigma_{corner}\, dx \tag{5.1}$$

$$\sigma_{developing-ave} = \frac{1}{2.7\times\lambda}\int_0^{2.7\times\lambda} \sigma_{developing}\, dx \tag{5.2}$$

$$\sigma_{developed-ave} = \frac{1}{L/2 - 2.7\times\lambda}\int_{2.7\times\lambda}^{L/2} \sigma_{developed}\, dx \tag{5.3}$$

These average surface charge density values normalized by the flat surface theory are presented in Figure 5.7 for different λ/H and pH values. Sigmoid functions are commonly used to model the pH dependence of quantities in literature[250]. However, a logarithmic function is found to be well-suited for the corner effects.

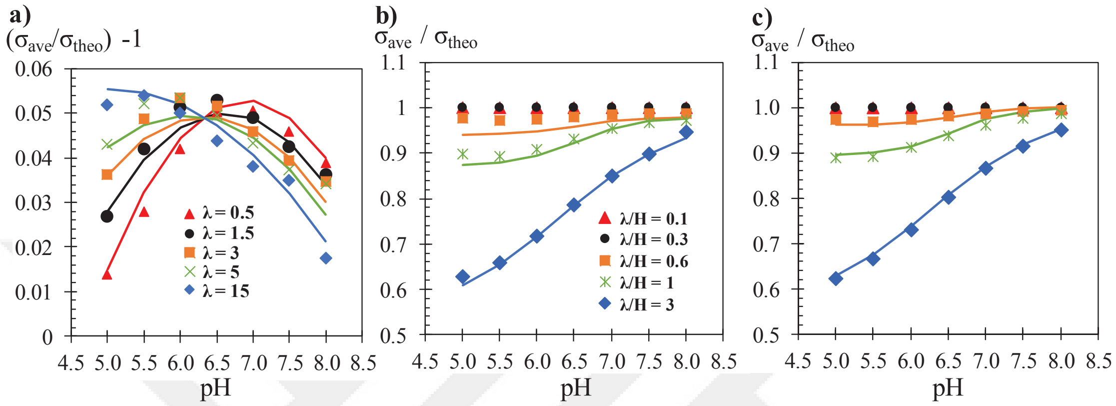

Figure 5.7. Normalized average surface charge densities measured (a) on a corner through 0→2.7λ, (b) in the developing region (0→2.7λ) after removing corner effects, and (c) in the rest of the channel (2.7λ→L). Markers represent numerical data and solid lines are the models.

The logarithmic function in Equation 5.4 provides the best fit for the corner effect behavior at varying pH values. This equation is a combination of two second-order functions of pH presented in Equation 5.5 and the logarithmic dependence is employed through the EDL thickness. The corresponding results of these equation are plotted in Figure 5.7(a), which show good agreement with the numerical data.

$$\sigma_{corner-ave}/\sigma_{theo} = 1 + \left(f[pH] + g[pH]\times\ln(\lambda)\right) \tag{5.4}$$

$$\begin{aligned} f[pH] &= -0.00923\, pH^2 + 0.12431\, pH - 0.36763 \\ g[pH] &= 0.00195\, pH^2 - 0.03113\, pH + 0.11879 \end{aligned} \tag{5.5}$$

On the other hand, sigmoid function in Equation 5.6 is well-suited for the surface charge behavior of both developing and developed regions. This equation has four different parameters that are all dependent on the EDL overlap ratio and serve for the correct representation of the physics in the channel. For example, p_1 is a hyperbolic tangent function that converges to zero for low λ/H and approaches to a constant value as

λ/H goes to infinity. Moreover, p_2, p_3 and p_4 are also functions of λ/H that describe the pH dependence appropriately.

$$\sigma_{developed}/\sigma_{theo} = 1 - \left(p_1 - \frac{p_1}{1+10^{(p_2 - pH)p_3}} \right) \tag{5.6}$$

$$p_1 = 0.58\tanh^2\left(0.54\, \lambda/H\right), \quad p_2 = 6.5307\left(\lambda/H\right)^{-0.034}, \quad p_3 = 0.9806\left(\lambda/H\right)^{-0.519} \tag{5.7}$$

Equation 5.6 is found to be suitable both for developing and developed regions' surface charge as can be seen in Figure 5.7. However, it should be stated that the average surface charge values of the developing region in Figure 5.7(b) are the averages of the charge values presented in Figure 5.6(e), (f) and (g) where corner effect are excluded.

Moreover, average surface charge density values of the developing region and the developed region are almost equal to each other for low values of λ/H after the corner effects are removed since ionic conditions of the channel and reservoirs become similar. With increasing EDL overlap, these conditions differ from each other and a so-called "second overlap" forms at channel inlet and outlet, resulting in different surface charge for the developing and the developed region. Yet, averaging process makes this effect to be almost negligible and only small differences are observed. For such a case, the parameters, p_1-p_3, recover the behavior obtained in both developing and developed regions, yielding good agreements between proposed models and the numerical results as can be deduced from Figure 5.7(b) and (c).

Finally, Equation 5.8 is formed that describes the average surface charge of a nanochannel. Since the charge determining effects are mostly corner and EDL overlap effects, this final equation is composed to be dependent only on these effects.

$$\sigma_{channel,ave} = \left(\frac{2.7\times\lambda}{L/2} \right)\sigma_{developing,ave} + \left(\frac{L/2 - 2.7\times\lambda}{L/2} \right)\sigma_{developed} \tag{5.8}$$

If Equations 5.4-5.7 are substituted into Equation 5.8, the final form of the equation (Equation 5.9) for the average surface charge density of nano-channel is obtained for a given channel height and length. Inlet/outlet and overlap effects are considered to behave in an additive manner. Second term in the parenthesis models the inlet/outlet effect and it is negligible when either double layer is very thin, or nanochannel is very long. Moreover, third term is the contribution from the double layer overlap and it either becomes negligible for weak EDL overlap or converges to a constant for strong

EDL overlap. Both terms vanish if the channel height and length are much larger than the EDL thickness, meaning that the flat surface theory can well-estimate the average charge of the channel.

$$\sigma_{channel,ave} = \left(\begin{array}{l} 1 + \dfrac{5.4\lambda}{L}\begin{pmatrix} (0.00195\,pH^2 - 0.03113pH + 0.11879)\ln(\lambda) \\ -0.00923\,pH^2 + 0.12431\,pH - 0.38763 \end{pmatrix} \\ -\tanh^2\left(0.54\dfrac{\lambda}{H}\right)\left(0.58 - \dfrac{0.58}{1+10^{\left[6.5307\left(\lambda/_H\right)^{-0.034} - pH\right]\left[0.9806\left(\lambda/_H\right)^{-0.519}\right]}}\right) \end{array} \right)\sigma_{theory} \quad (5.9)$$

Above equation can accurately calculate the average charge density of the nano-channels, which are longer than 5.4λ since the developing region is as long as 2.7λ from both side of the channel. In Figure 5.8, the proposed model in Equation 5.9 and the numerical results are compared for varying L/λ and λ/H to check the accuracy of the model. It can be seen that the results of Equation 5.9 and numerical model present a good match except for $L/\lambda<5.4$, which is expected.

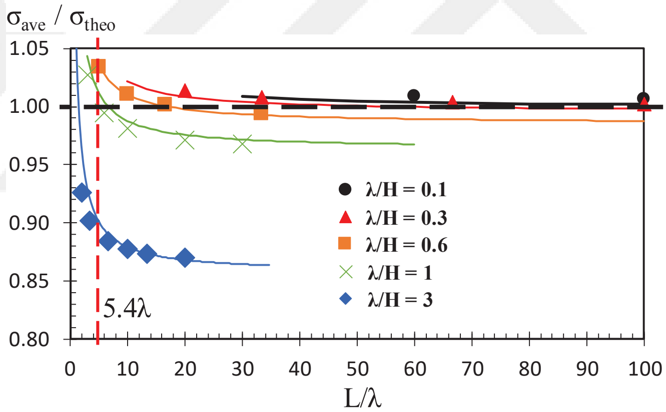

Figure 5.8. Nanochannel average surface charge results (for pH=7) from the extended theory (solid lines) given by Equation 5.9 in comparison with numerical calculations at different channel lengths.

Figure 5.8 also shows that the effects of electrokinetically developing region becomes can be safely ignored for channels with $L>50\lambda$ and the average surface charge of the nano-channel only depends on the overlap ratio regardless of the channel length. As the overlap ratio increases indicating that channel height is comparable with the EDL thickness in size, the average charge of the channel substantially deviate from the theoretical estimations. On the other hand, the effect of developing region on the surface charge becomes dominant for shorter channels, resulting in higher surface charge values that may be even higher than the theoretical estimations.

5.2. Flow Rate and Ionic Current through Silica Nano-channels/pores

After validating the current model in Section 4.1 as presented in Figure 4.4, viscoelectric and velocity slip effects are incorporated into the model by using Equation 2.2 and Equation 2.3, respectively. As a first step, the affected velocity profiles for each case are presented for a 10 nm height and 100 nm length channel. The flow is generated by applying a pressure gradient of 92 Pa/nm across the channel. The normalized velocity profiles away from inlet and exit regions are presented in Figure 5.9 for salt concentrations of 0.42 mM, 0.94 mM and 10 mM. While Figures 5.9(a)-(c) are normalized with the average velocity estimations of simple Poiseuille flow (PF) that are not subjected to any electrokinetic or slip effects, Figures 5.9(d)-(f) are normalized with their own averages. First of all, only electroviscous effect is considered. As discussed, this effect is commonly characterized by the EDL overlap. For the concentration range in the current study, EDL thickness varies between 1.5 nm to 15 nm where channel height is 10 nm. The corresponding overlap ratio range does not create a significant variation in the velocity with concentration change due to electroviscous effect for no-slip cases. Then, viscoelectric effect in incorporated into the model through Equation 2.1. The resulting velocity profiles showed significant local variations due to viscoelectric effect near the charged surfaces, especially at 10 mM salt concentration where the velocity profile becomes almost flat near the walls. Moreover, overall velocity profiles present strong deviations from the PF estimations. Finally, slip velocity presented in Equation 2.2 is included with $L_{s,0}$=5 nm. As expected, slip velocity increases the overall velocity profile inside the channel and promotes the transport. Yet, the enhancement in the flow rate is much less compared to simple PF cases with and without velocity slip. This is mainly because electrokinetic effects, which alters the near-wall hydrodynamics affecting the velocity gradient at the charged wall. Both conduction current that cause the electroviscous effect and viscoelectric effect decrease the velocity gradient, hence the slip velocity. Naturally, this behavior is concentration dependent and velocity slip decreases as the salt concentration increases in the aqueous solution. Yet, primary reason is the viscoelectric effect that cause 30% decreases in the velocity even at low concentration (i.e. 0.42 mM) and almost no-slip (~80 % decrease) occurs on the walls at 10 mM salt concentration.

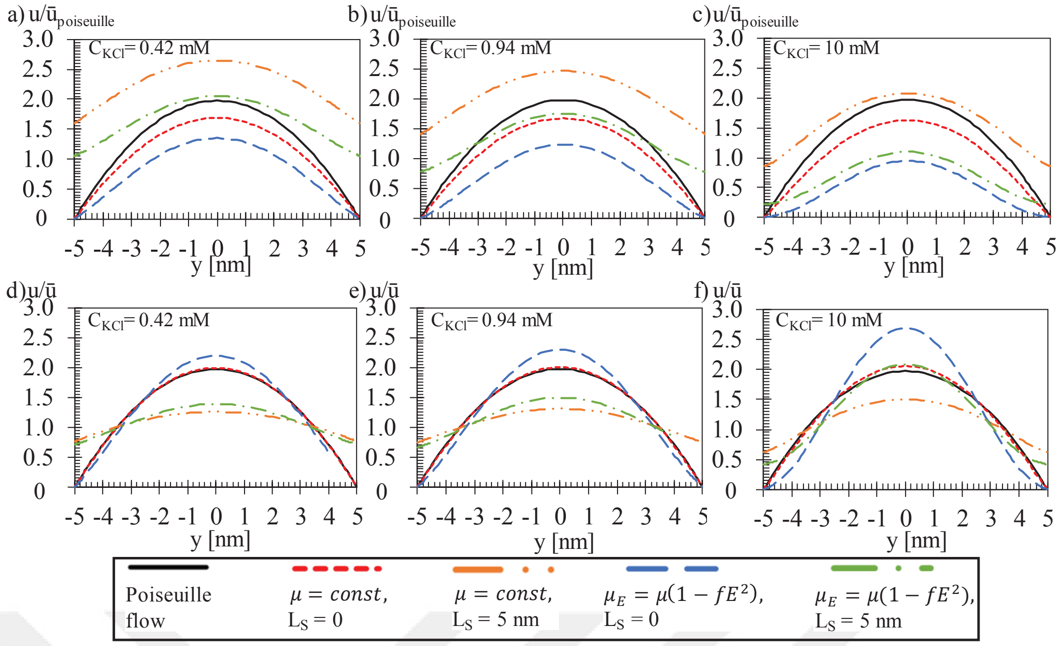

Figure 5.9. Velocity profiles along the channel height under different effects and at different salt concentrations. Velocities were normalized (a), (b) and (c) with the average velocity of the simple pressure driven (Poiseuille) flow solution and (d), (e) and (f) with the average velocity of corresponding case.

Moreover, the normalized results in Figures 5.9(d)-(f) show the deviations from PF estimations through shape change of the velocity profiles. Normally, a perfect parabolic velocity profile form for a fully developed PF flow. This shape is almost preserved when only electroviscous effect is considered for all concentrations. However, velocity profiles are no longer in parabolic shape when viscoelectric and slip effects were considered.

To resolve the viscoelectric effect, the volume charge density and resulted electric field strength at the channel center are estimated and presented in Figure 5.10(a) and (b), respectively. Charge concentration near the charged walls exponentially increase as a result of the ionic layering inside the EDL. As the concentration increases, surface charge and resulting counter-ion accumulation and electric field strength increase while both reach the bulk conditions sufficiently away from the surface. This is expected since thick EDL formation in diluted solutions originates weak effects on the fluid flow while strong electrostatic interactions occur for thin EDL thicknesses. For example, the volume charge density is almost 5 times higher at 10 mM compared to 0.42 mM and 0.94 mM salt concentrations causing the electric field strength to double as a result of highly condensed and strong ionic layering near the charged walls. The resulted electric field causes the viscosity of the fluid to increase in those regions as shown in Figure 5.10(c). It can be seen in this figure that the local viscosity near the surface can be as high as 10-12 times of its thermodynamic value depending on the concentration.

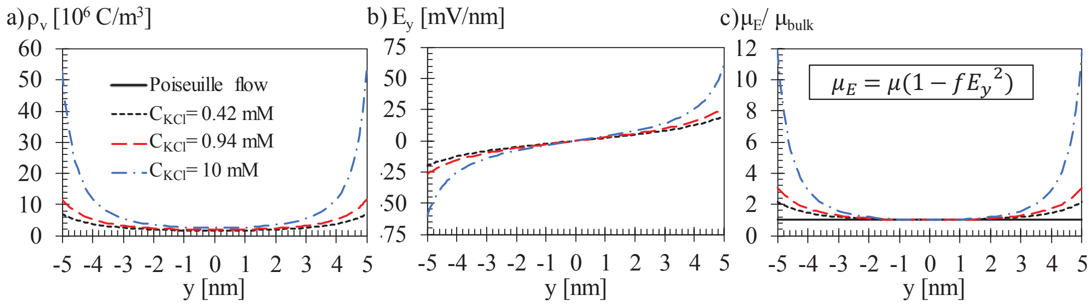

Figure 5.10. Distribution of (a) volume charge density, (b) electric field, and (c) normalized local viscosity along the channel.

As a next step, slip velocities on the charged walls are calculated at varying ionic concentration for constant slip length and pressure gradient. First, slip velocities for the electrokinetic flow are normalized with the slip velocities developing for a pressure driven flow with no ionic interactions involved. The results are presented in Figure 5.11(a) for both ionic flows with electroviscous effect and constant viscosity, and for ionic flows with both electroviscous and viscoelectric effects. In either case, lower slip velocities develop compared to PF slip velocity. Moreover, slip velocity decreases as the salt concentration increases for both cases. Conduction current in the EDL caused by the electroviscous effect reduces the velocity gradient at the interface. As a result, velocity slip decreases even if the slip length is kept constant. Also, pressure driven flow is further inhibited due to viscoelectric effect that forms higher local viscosity near the surface creating higher shear force. As expected, the slip velocities are much lower when both electroviscous and viscoelectric effect are considered. Since these effects are stronger for thin EDL thicknesses, velocity slip becomes lower with elevated concentrations. When both electroviscous and viscoelectric effects are incorporated into the model, almost no-slip condition is achieved at 10 mM salt concentration. However, the concentration dependence ceases after 7 mM at which the overlap ratio (i.e. λ/H) becomes 0.73. Therefore, the concentration range is kept in limited between 0.42 mM and 10 mM. These results indicate that the boundary slip should not be studied based solely on the slip length value. In Figure 5.11(b), the slip velocity values are normalized with the values developing at the lowest concentration (i.e. 0.42 mM) at which lowest deviation from PF slip velocity is observed. While almost 40% decrease is observed under electroviscous effects due to concentration, a decrease of 80% occurs when both electroviscous and viscoelectric effects are considered. Moreover, the surface charge values developing at these concentrations are presented in Figure 5.11(c) in order to create an understanding for the dependence of slip velocity on the surface charge variation.

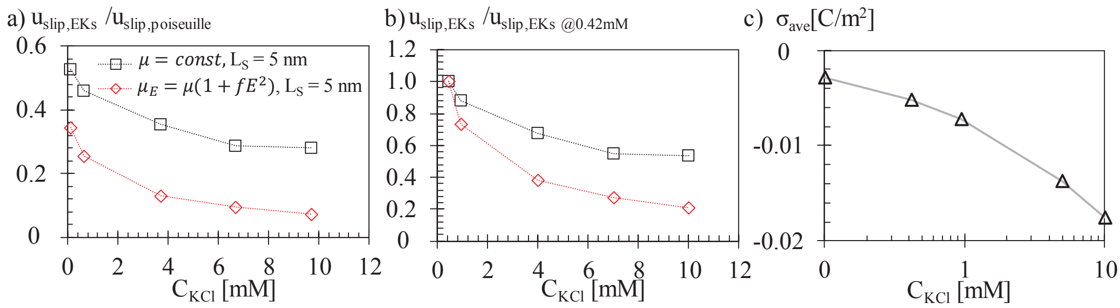

Figure 5.11. Variation of velocity slip on surface normalized by (a) the Poiseuille flow velocity slip, and (b) velocity slip measured at 0.42mM case. (c) Silica surface charge as a function of salt concentration based on charge regulation.

The observations gained from the current results are very similar to those obtained by the MD studies in the literature. Yet, the velocity slip variations are explained by the slip length change in those studies. Even if slip length is dependent on the surface charge as in Equation 3.11, this dependence is due to the change in electrostatic forces altering interfacial coupling and vanishes at low surface charges within the charging range of natural surface chemistry. Therefore, the variation in slip velocity in the current study is not due to the surface charge. Instead, the affected near wall electrohydrodynamics alter the slip velocity. In a very recent study of Rezaei et al.[31], they estimated different slip lengths based on the local and bulk velocity gradients in the MD simulations of shear driven flows. These slip lengths are presented in Figure 5.12(a) as a function of surface charge in comparison with the predictions of Equation 3.11. Results show that local slip length stays almost constant, similar to the predictions of Equation 3.11. On the other hand, bulk slip length decreases as the surface charge increases. Similar results are obtained also by Celebi et al.[32] through their MD studies in which slip velocity change is attributed to the viscoelectric effect by Equation 3.10. They also related the measured slip velocity and slip length for low surface charge values where there is no significant variation in the slip length is observed as shown in Figure 5.12(b). Therefore, the change in slip velocity is not due to the slip length but it is caused by the variation in the near wall electrohydrodynamics.

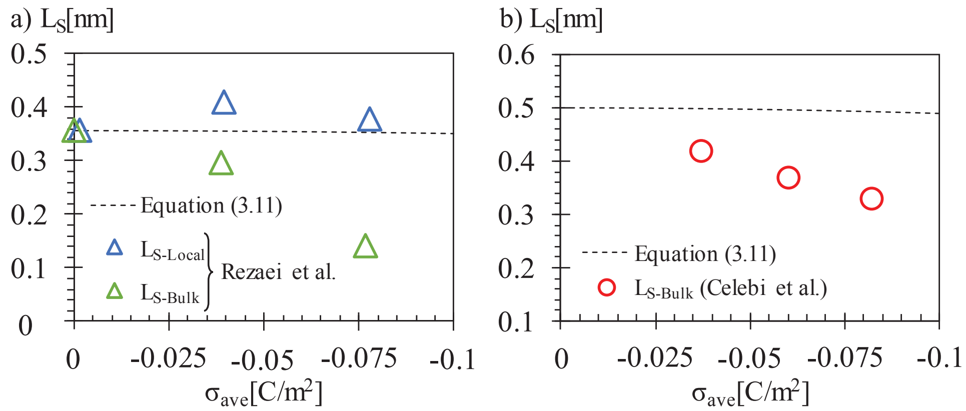

Figure 5.12. Variation of slip lengths by surface charge measured by MD simulations (markers) from (a) Rezaei et al. [31]and (b) Celebi et al.[32] compared with the estimation of Equation 3.11 from Joly et al.[106] (dashed lines)

MD simulations model the interface coupling and the near-wall hydrodynamics without requiring any special models for the quantities. In the current study, the variation of viscosity and velocity slip condition are described by models. Yet, similar findings are obtained. This indicates that the momentum coupling at the interface measured by MD simulations can also be calculated using a continuum solution with Navier-type boundary condition if the electrohydrodynamics based on electroviscous and viscoelectric effects are included.

As a next step, the ionic currents are calculated by using Equation 4.1 for KCl concentrations of 0.1 mM, 0.42 mM, 0.94 mM, 5mM and 10 mM at pH=7.5. Electroviscous, viscoelectric and slip effects are systematically included into the numerical model in order to examine each effect compared to the existing theoretical study of Mei et al.[58] Therefore, the model parameters are chosen the same with their study. As can be seen in Figure 5.13, the results of the current model coincide with those of Mei et al. when no viscoelectric and slip effects are included into the current model. Moreover, ionic current increase with the salt concentration when only electroviscous effect is considered since this effect diminised at high concentrations. With the addition of viscoelectric effect, ionic current decreases upto 30%, compared to the case with only electroviscous effect, especially for high concentrations since viscoelectric effect become dominant. Hence, the difference between the square and the circle markers are solely due to viscoelectric effect.

Then, velocity slip boundary condition is assigned to channel walls. Even though the charge dependent slip length (i.e. Equation 3.11) is considered in the current study, slip length does not show significant variation for the the current range of surface charge according to natural CR behavior. This can be supported by the results of earlier studies in the literature that conclude that surface charge should be higher than 10^{-1} C/m^2 in order for the slip length to vary[108, 109]. Since the highest surface charge in this study is in the order of 10^{-2} C/m^2, a constant slip length value of 5 nm is chosen for the cases with slip condition. As expected, the ionic transport significantly increases even if a moderate slip length is employed in the current study. Similar to electroviscous effect with no-slip condition, ionic current increases with the concentration. As already discussed, slip velocity decreases with increasing concentration. More interestingly, this also decreases the electroviscous effect since ionic transport reduces. Therefore, concentration dependence of the ionic current is the same as no-slip cases even if slip velocity reduces. When the viscoelectric effect is also considered, the enhancement in the ionic current significantly altered at elevated concentrations since velocity slip decreases due to viscoelectric effect. Such an outcome is expected since the velocity slip strongly depends on the velocity gradient at the interface, which can substantially change as a result of electrokinetic effects. This is mostly overlooked in the current literature since most of the studies examine the velocity slip through the change in slip length. Therefore, the current study aims to contribute to the current literature by resolving such effects on the slip behavior at the interface.

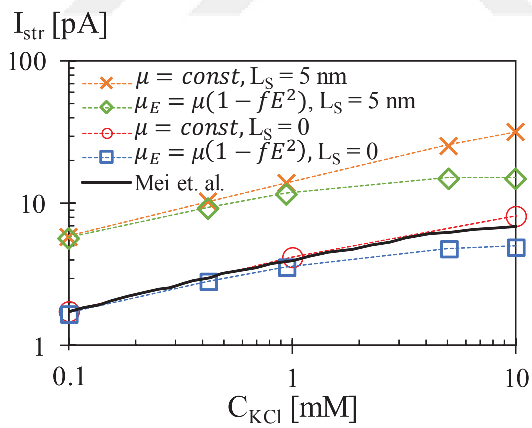

Figure 5.13. Ionic current of the electroviscous flows with and without viscoelectric and velocity slip effects as a function of salt concentration.

Current literature is also missing a complete knowledge on the length dependence of ionic transport in combination with the electrokinetic effects. There are various studies that focus on the short channels concluding that electrokinetics inside these channels differentiate from those of long channels for which inlet/outlet effects are ignored[75, 76, 78]. In this context, the length dependence is also examined for different conditions in the current study. Velocity profiles at the mid-channel location of nano-channels for channel lengths of 5 nm, 10 nm, 20 nm, 50 nm and 100 nm are presented for salt concentrations of 0.42 mM, 0.94 mM and 10 mM are calculated and presented in Figure 5.14. In the first row (i.e. Figures 5.14(a)-(c)), the resulting velocity profiles under electroviscous effect is compared with PF estimations with no slip condition. At the same concentration value, the overall velocity profile increase with decreasing channel length since the ionic concentration difference across the channel decreases, causing a weaker electroviscous effect. Also, the ionic concentration difference between the channel and reservoir decreases for shorter channels, creating lower resistance due to channel/reservoir equilibrium. In such a case, channel length and ionic concentration are the determining parameters of the ionic transport. Therefore, the axial electric potential distribution and resulting electric field along the center line are presented in Figures 5.15(a) and (b) for L=5 nm, 50 nm and 100 nm at 10 mM salt concentration. It can be seen in Figure 5.15(a) that lower electric potential difference forms between the channel and reservoir for short channels and as a result, lower electric field originates as presented in Figure 5.15(b). Consequently, shorter channels create less resistance to ionic current[77]. As a next step, the concentration dependence of channel/reservoir equilibrium is presented in Figures 5.15(c) and (d) for a 100 nm-length channel. These figures shot that smaller electric fields originate at higher concentrations since the EDL thickness reduces and reservoir bulk conditions are obtained inside the channel, creating lower potential bias between the channel and the reservoir. Moreover, high osmotic pressures build up at the inlet and outlet regions at low bulk concentrations that makes the nano-channels to be so called ion selective[78].

Next, the velocity profiles of the pressure driven flow under both electroviscous and viscoelectric effects are presented in the second row (Figure 5.14(d)-(f)). Stronger length dependence is observed for 10 mM KCl concentration where velocity increases almost 40% from 100 nm channel length to 5 nm channel length. However, flow velocity becomes more flat near the walls for short channels due to higher surface charge developing at the inlet/outlet regions, which increases the local viscosity around those regions. Such a consequence in short channels cause interesting outcomes at slip conditions whose velocity profiles are presented at the third row (Figure 5.14 (g)-(i)). It would be expected that these velocity profiles shifted upwards due to velocity slip. Yet, slip velocity presents a dependence also on the channel length in addition to the concentration. This is mainly because electroviscous and viscoelectric effects are altered by the varying channel lengths. Moreover, huge divergences from PF flow are observed.

When viscoelectric effects are not considered (i.e. last row of Figure 5.14), the slip velocity at the walls slightly increase, especially at 10 mM where viscoelectric effects are dominant.

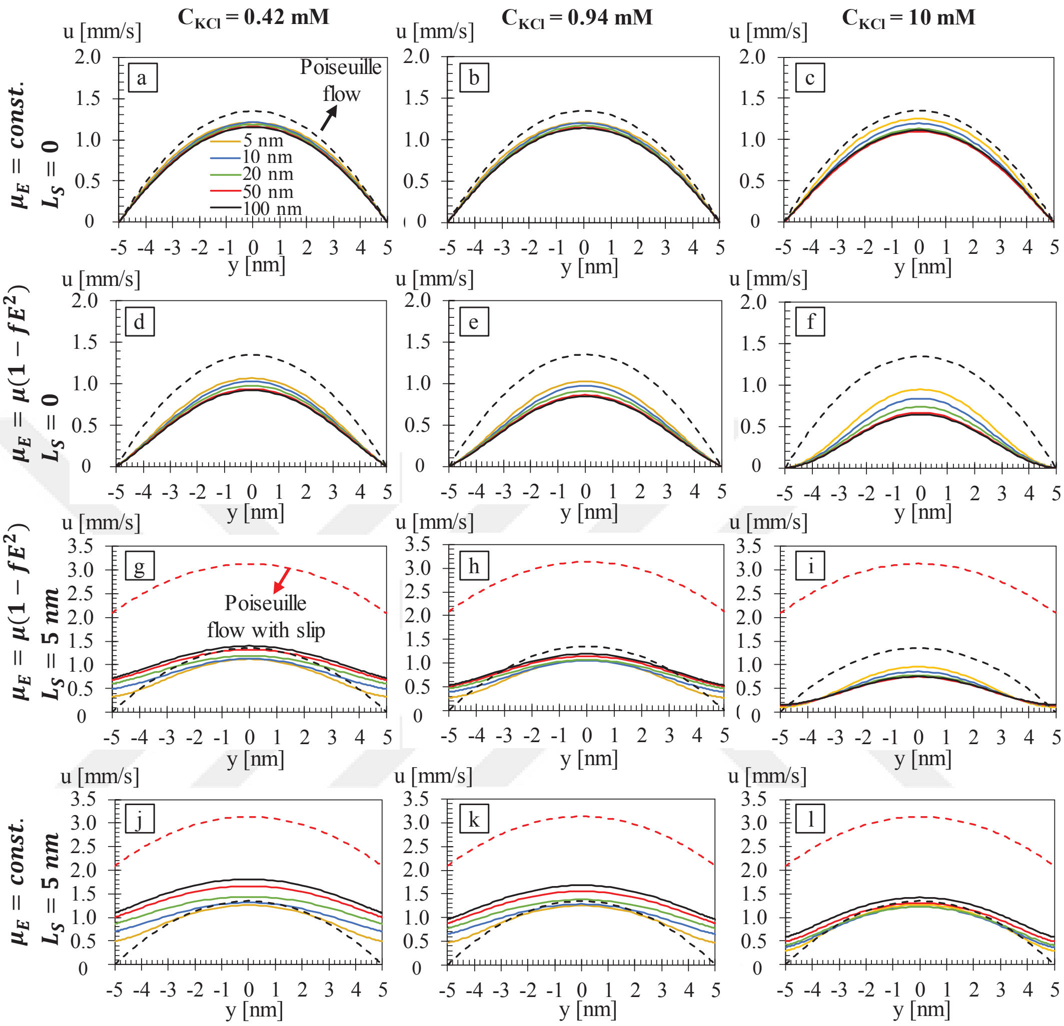

Figure 5.14. Velocity profiles along the channel height measured at the middle of 5 nm, 10 nm, 20 nm, 50 nm and 100nm length channels at KCl concentrations of 0.42 mM (a, d, g, j), 0.94 mM (b, e, h, k) and 10 mM (c, f, i, l) in the cases different electrokinetic effects were considered.

In order to see the variation of slip velocity at different channel lengths, the slip velocities of the flows under only electroviscous effect and under both electroviscous and viscoelectric effects are calculated and presented in Figure 5.16(a) and (b), respectively for different KCl concentrations. As seen in both figures that the slip velocity decrease with channel length, which is even more evident at lower concentrations. With the viscoelectric effects, overall slip values decrease around 40%. Moreover, the length dependence of slip disappears for channel lengths higher than 20 nm.

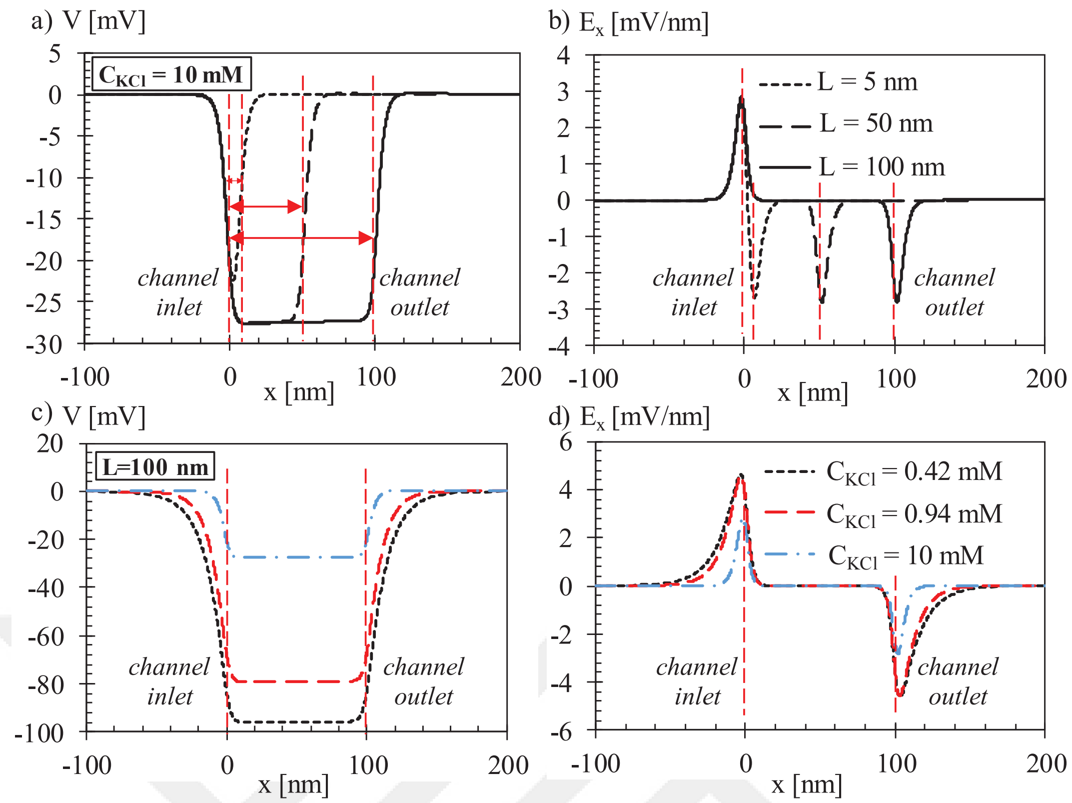

Figure 5.15. (a) Electrical potential and resulted (b) electric field strength variation along the centerline for different length channels at salt concentration of 10 mM. (c) Electrical potential and resulted (d) electric field strength variation along the centerline for different salt concentrations in 100 nm long channel.

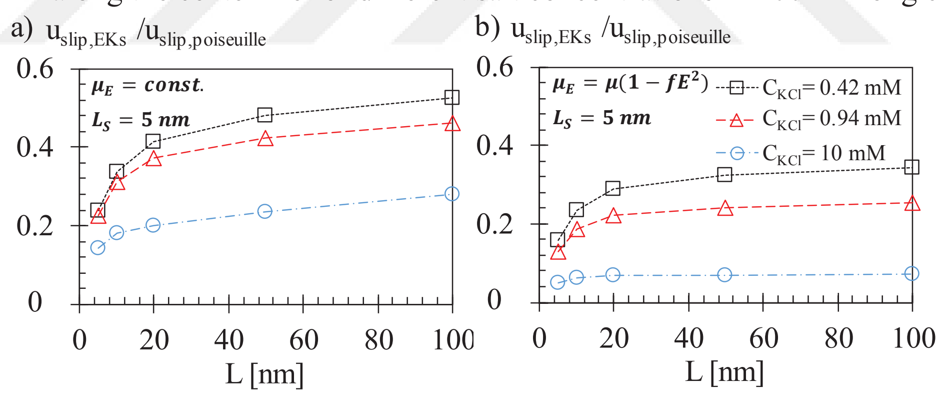

Figure 5.16. Velocity slip at the wall (a) without and (b) with inclusion of viscoelectric effects

Finally, ionic current (Equation 4.1) and flow rates (Equation 5.10) are calculated for different channel lengths, varying concentrations and under different electrokinetic effects.

$$Q = 2w\rho \int_0^{h/2} u(y)\,dy \tag{5.10}$$

Results are presented in Figure 5.17. Mass flow rates are normalized by the PF flow estimations and by the mass flow rate of the longest channel length in Figures 5.17(a) and (b), respectively. If only electroviscous effect are considered, the flow rates become lower than PF estimations while length and concentration dependences are very weak. For a channel length of 5 nm, the flow rate approaches to PF estimations since conduction current is almost negligible in short channels. With the addition of viscoelectric effects, flow rates further decrease and stronger length and concentration dependences are observed. Overall, both effects become negligible on the flow rate as the salt concentration and channel length decrease.

When velocity slip in introduced, flow rate increase, as expected and the flow rates become even 70% higher than the PF estimations for 100 nm channel length in the case where only electroviscous effect is considered at concentration of 0.42 mM. When the concentration increases or the channel length decreases, the flow rate converges back to PF estimations. When viscoelectric effect is also considered, slip velocity at the interface reduces, causing the flow rate to decrease. The flow rate becomes even lower than the PF estimations for 10 mM concentration since the viscoelectric effect is dominant. It should be noted here that a slip length of 5 nm, which is employed for these simulations, is an average value for a hydrophobic surface with wetting contact angle around 90°[251]. Even for such a small slip length, flow velocity increase almost 3 times and mass flow rate almost 5 times for a simple PF case. Yet, when electrokinetic effects are introduced, such enhancements cannot be achieved, especially for short channels and high concentrations. For example, there is almost 50% decrease in the flow rate for 10 mM case with electroviscous and viscoelectric effects even if boundary slip is applied on the channel walls. On the other hand, velocity slip only balances the flow rate reduction caused by the electroviscous and viscoelectric effect, causing the flow rate to be equal to PF estimations.

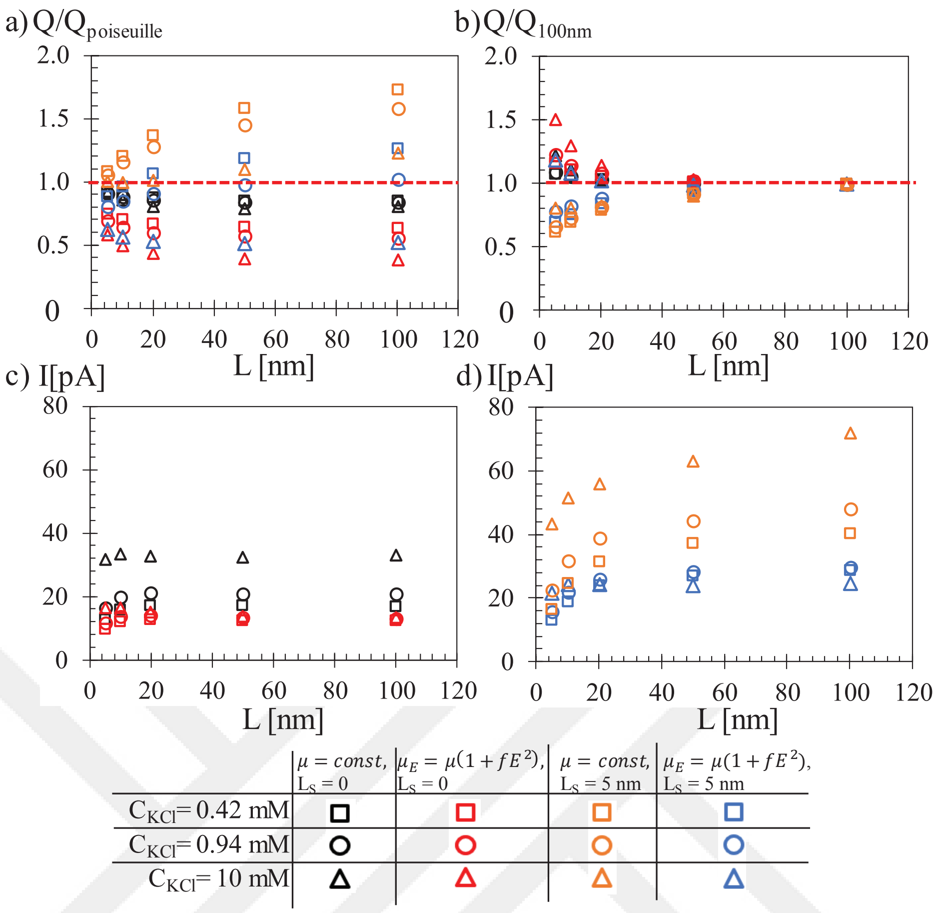

Figure 5.17. Flow rates of different length channels (a) normalized by Poiseuille flow (PF) calculation (b) normalized by the results of 100 nm length channel. (c) Ionic currents without slip effect and (d) ionic currents with slip effect.

To further resolve the channel length effects on the flow rate, the flow rates are normalized by those developed in 100 nm length channels in Figure 5.17(b). It can be seen in this figure that flow rate almost stays constant for channel lengths of 50 nm and 100 nm, indicating that length dependence disappears for longer channels. Decreasing the channel length causes the flow rate to increase for no-slip case. Yet, an opposite behavior is observed for slip cases. This is caused by the fact that electrokinetic effects become weak for short channels but boundary slip is lower for short channels, resulting in lower flow enhancements for short channels.

Moreover, ionic currents are also presented in Figures 5.17(c) and (d) for no-slip and slip conditions, respectively. For the cases where only electroviscous effect considered, ionic current increases with salt concentration since lower conduction current forms in the channel. This behavior is opposite to the concentration dependence of flow rate. However, ionic current also accounts for the number of ions carried across the system and more ions are carried for higher concentrations. Therefore, ionic current enhances. Similar behavior is observed also in other studies where ionic current increases with concentration[19, 77, 252]. When viscoelectric effect is included, the concentration dependence of ionic current diminishes, except very short channels at low concentrations. Basically viscoelectric effect represses the enhancement due to concentration increase. Another important conclusion that can be deduced from these figures is that there is almost no channel length dependency in the case of no-slip whereas velocity slip increases the ionic current as the channel length increases. Similar behavior is observed also with viscoelectric effect but less concentration and length dependences are observed. These results show that electroviscous and viscoelectric effects have not only direct impact on the ionic current but they also create length dependence through the slip velocity variation for different length channels.

5.2.1. Velocity Slip in Larger-scale Liquid Systems

As concluded, velocity slip is highly dependent on electroviscous and viscoelectric effects in nanochannels where the overlap ratio, λ/H, is larger than unity. Yet, how the velocity slip develops for channels when this ratio is much smaller than the unity (i.e. λ/H<<1) is another missing knowledge in the literature. Therefore, a pressure driven fluid flow in wider channels are further examined in the current study. In Figure 5.18, the potential contours are presented for channels with 10 nm and 250 nm heights, respectively. It is clearly seen that the electric potential inside the channel with 10 nm height is far from bulk conditions (i.e. V=0) while almost the entire channel is in bulk conditions for 250 nm height channel. Therefore, it is expected that the electrokinetic effects should play no role on the fluid flow for the latter case.

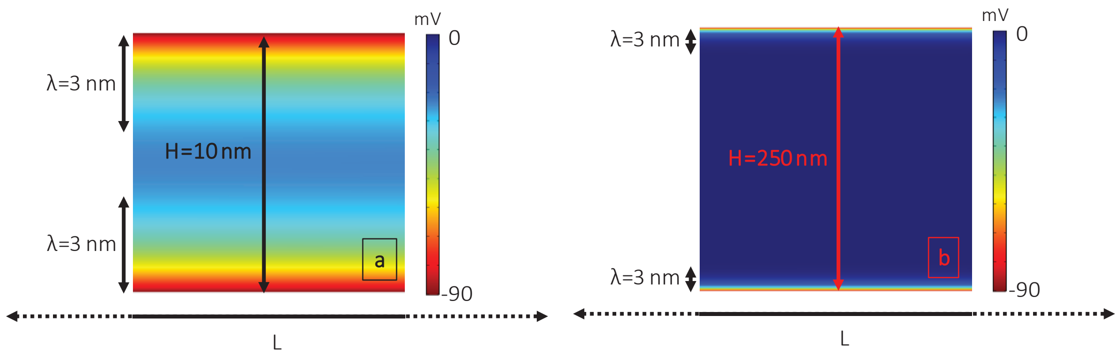

Figure 5.18. Electric potential contours in a) 10 nm height channel b) 250 nm height channel.

In this context, the velocity profiles and flow rates developed for varying channel heights with no-slip condition are calculated for a flow under electroviscous effect only and both electroviscous and viscoelectric effects. The results are presented in Figure 5.19 for channel heights of 10 nm, 50 nm, 100 nm and 250 nm at C_{KCl}=50 mM and pH=7.5. While the velocity profiles are normalized with the maximum velocity of PF estimations, y-locations are normalized with the channel height for a better comparison. Moreover, flow rates are normalized with the PF estimations to determine the channel height at which electroviscous and viscoelectric effects are negligible. It can be concluded from these figures that although both effects still exist, they are limited only in a limited region. Therefore, neither effect have influence on the flow velocity when the channel height is 250 nm under no-slip condition. Yet, this is an expected outcome.

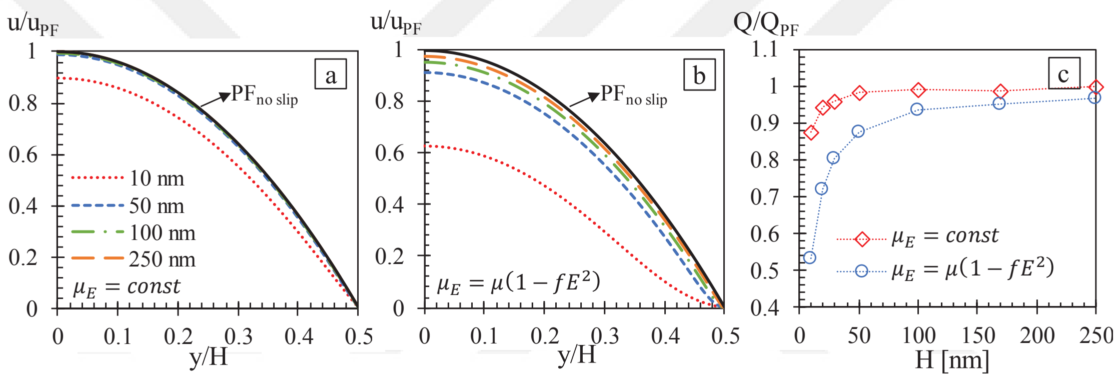

Figure 5.19. Velocity profiles for channel heights of 10 nm, 50 nm, 100 nm and 250 nm at C_{KCl}=50 mM and pH=7.5 when a) only electroviscous effect is considered b) electroviscous and viscoelectric effects are considered; c) and their normalized flow rates.

As a next step, we introduced velocity slip into calculations for varying channel heights. Slip length, L_S, is kept constant at 50 nm while channel height is varied as H=150 nm, 200 nm, 250 nm, 300 nm, 400 nm and 500 nm. The results are presented in Figure 5.20. The velocity profiles are normalized with the maximum velocities of the Poiseuille flow estimations with velocity slip. This way, general height dependence of the Poiseuille flow velocity can be eliminated and the pure electrokinetic effects on the velocity slip can be observed. Basically, electrokinetic effects cause changes at inner and outer scales. With the addition of velocity slip, electroviscous effect starts dominating the flow at the outer scale even though it is negligible without the slip condition. Yet, its impact on the velocity slip is saturated at the inner scale that the normalized slip velocity becomes independent of the channel height. This fact can be clearly observed in Figure 5.20(a). Similarly, although velocity slip further decreases with viscoelectric effect, it does not change with the channel height as observed in Figure 5.20(b). The variation of the velocity at the outer scale in Figure 5.20(b) is solely caused by the electroviscous effect. Corresponding flow rates are also presented in Figure 5.20(c). It can be observed from the flow rates that height dependence occurring at outer scale also start converging to a certain value as the channel height increases.

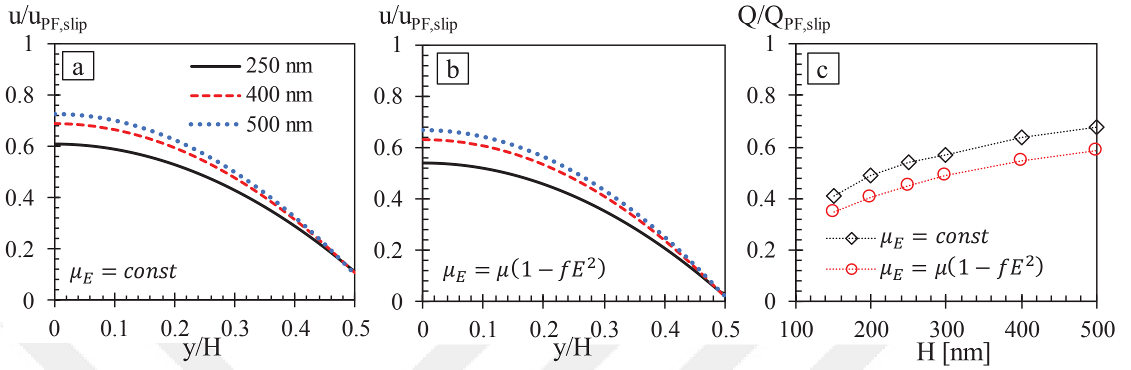

Figure 5.20. Normalized velocity profiles for channel heights of 250 nm, 400 nm and 500 nm when a) only electroviscous effect is considered b) electroviscous and viscoelectric effects are considered; c) and their normalized flow rates for channel heights of 150 nm, 200 nm, 250 nm, 300 nm, 400 nm and 500 nm.

In order to resolve the concentration dependence of velocity slip in these larger scale systems, the normalized velocity profiles in 250 nm height channel are estimated for 0.42 mM, 10 mM, 100 mM and 300 mM salt concentrations with and without viscoelectric effect. The slip velocity is included with a slip length of 50 nm, which is a moderate slip length. Figure 5.21(a) shows that electroviscous effect creates variation in the hydrodynamics of the flow both at inner and outer scales at different concentrations. However, such effect becomes only limited at inner scale as the concentration increases. Therefore, the overall flow velocity increases at elevated concentrations. Including the viscoelectric effect changes the near-wall hydrodynamics, especially at high concentrations and strong variations in the velocity slip is observed compared to the cases where only electroviscous effect is considered. Hence, velocity profiles start coinciding as observed in Figure 5.21(b) and almost no-slip conditions are obtained even for a moderate slip length of 50 nm. In Figure 5.21(c), the corresponding flow rates are presented for increasing concentrations. It can be concluded from these flow rate results that electroviscous effect becomes weaker and viscoelectric effect becomes dominant as the concentration increases, which is an expected behavior.

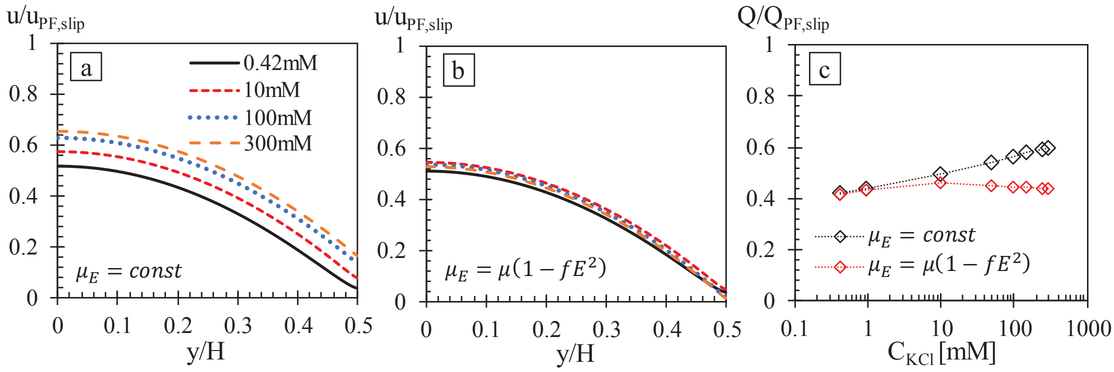

Figure 5.21. Normalized velocity profiles for 0.42 mM, 10 mM, 100 mM and 300 mM salt concentrations when a) only electroviscous effect is considered b) electroviscous and viscoelectric effects are considered; c) and their normalized flow rates for channel heights of 0.42 mM, 0.94 mM, 10 mM, 100 mM, 150 mM, 200 mM and 300 mM.

Lastly, the slip length dependence is examined for a 250 nm height channel at 50 mM salt concentration for slip lengths of 5 nm, 15 nm, 25 nm, 50 nm, 100 nm and 150 nm. The results are presented in Figure 5.22. First, it is deduced from Figure 5.22(a) that increasing slip length not only cause changes at inner scale but also at outer scale. Electroviscous effect starts dominating the flow at both scales as the slip length increases. Therefore, strong variations are observed in the velocity profiles with slip length variations. With the inclusion of viscoelectric effect in Figure 5.22(b), the dependence of velocity slip on the slip length starts disappearing and almost no slip condition is observed regardless of the slip length. This causes decreasing normalized flow rates with increasing slip lengths as observed in Figure 5.22(c).

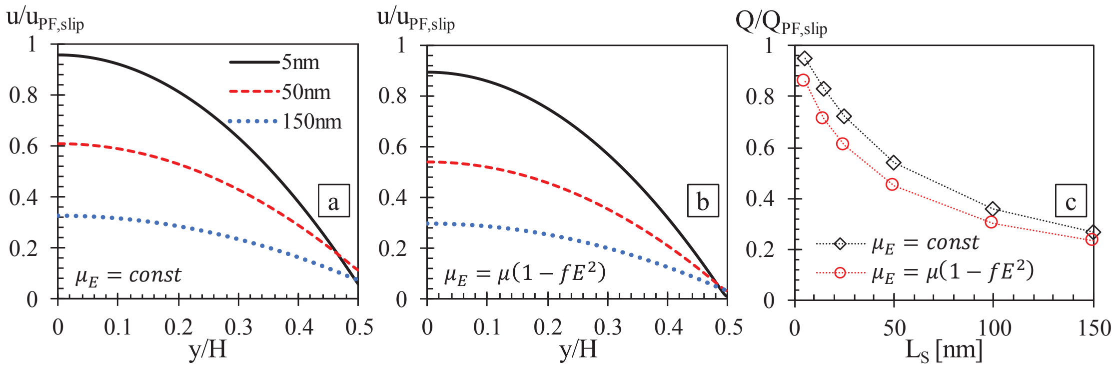

Figure 5.22. Normalized velocity profiles for slip lengths of 5 nm, 50 nm and 150 nm when a) only electroviscous effect is considered b) electroviscous and viscoelectric effects are considered; c) and their normalized flow rates for slip lengths of 5 nm, 15 nm, 25 nm, 50 nm, 100 nm and 150 nm.

These results suggest that even if electrokinetic effects are negligible on the flow in the absence of velocity slip in larger scale systems, they become dominant again once velocity slip is introduced. Moreover, velocity slip at the wall develops independent from the channel height since channel height variations does not affect the inner scale physics. With that in mind, velocity slip is highly dependent on the slip length and concentration since these parameters directly affects the near-wall hydrodynamics, hence the inner scale flow physics.

5.3. Internal Surface Charge of Mesoporous Media

The mesoporous silica is defined as in Figure 4.6 with a pore size (H) and porosity (ϵ). As this stage, aspect ratio of the solid phase is kept as unity. In Figure 5.23, the resulting electric potential contours are presented for varying H, ϵ and λ. First, different pore sizes (H=20nm, 50nm, 100nm and 200nm) and EDL thicknesses (λ=1.5nm, 5 nm and 15nm) are examined at constant porosity of 0.8 and pH=6, whose contours are shown in Figure 5.23(a). In this figure, each row is at the same salt concentration and each column is at the same pore size. As can be depicted from this figure, bulk conditions (i.e. V=0) are achieved at low EDL thicknesses or high pore sizes. For example, electric potential at the pore centers are all in bulk conditions for all pore sizes for λ=1.5 nm and for all EDL thicknesses for H=200 nm. As the concentration decreases resulting in thicker EDL in the system, EDLs of the opposite surfaces overlap and electrical potential at the pore center for those case diverge from bulk conditions. Moreover, potential distributions vary along the pore surfaces due to the interactions of pore throat and pore center. Therefore, the ionic environment in the pore is affected by the H and λ of the system.

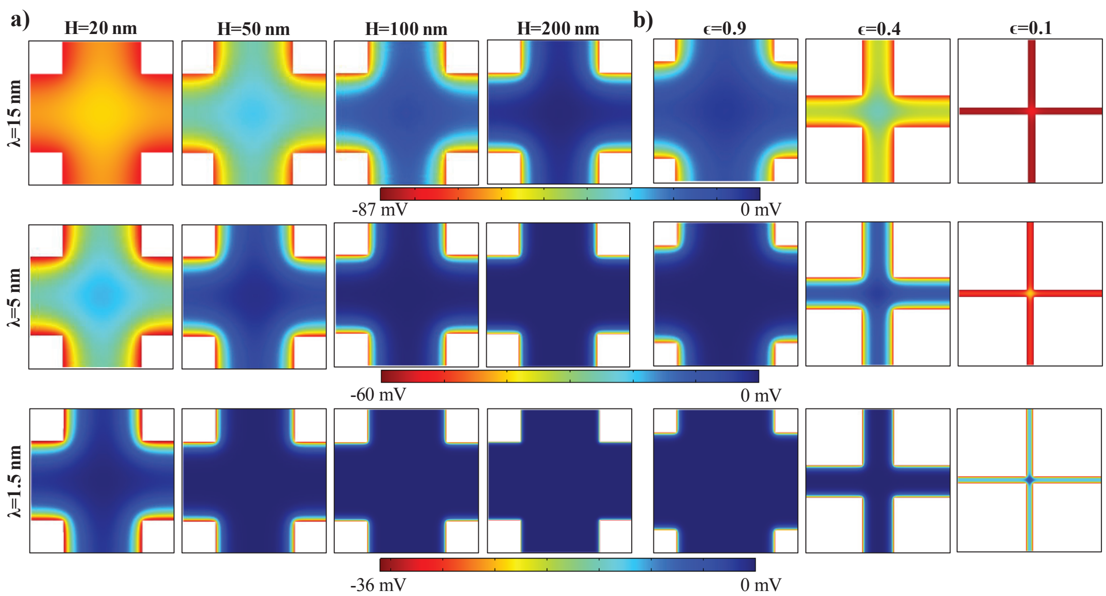

Figure 5.23. (a) Electric potential contours of varying EDL thickness and pore size at the constant porosity of 0.8. (b) Electric potential contours of varying EDL thickness and porosity at the constant pore size of 100nm.

Second, the electric potential contours for porosities of 0.9, 0.4 and 0.1 and for EDL thicknesses of 1.5 nm, 5 nm and 15 nm at constant pore size of 100 nm are presented in Figure 5.23(b). Decreasing the porosity of the system results in longer and narrower pore throats which cause strong EDL overlap but reduced pore to throat connectivity effects. In this context, the surface charge along the pore throats are estimated and presented in Figures 5.24(a), (b) and (c) where surface charge values are normalized by the flat surface theory. It can be noticed at a first glance that surface charge remains constant away from the corners. However, strong variations are observed around the corners due to axial interactions of pore center and pore throat. These local variations can propagate in the pore throats as a function of the throat length and EDL thickness. Such a mechanism is described earlier in Section 5.1. where electrokinetic development length is discussed. Figure 5.24 shows that there are two dominant mechanism defining the charge a porous system: EDL overlap that decreases the normalized charge density and pore to throat connectivity shows an opposite behavior. For example, EDL overlap can cause up to 40% decrease the charge density as in the 0.1 porosity case in Figure 5.24(c) and connectivity increase the charge density around the corners by almost 60% as in the 0.9 porosity case of the same figure. In order to resolve this increase, the charge density values along the pore throat length (l_t) are estimated and presented in Figures 5.24(d), (e) and (f). In order to separate the EDL overlap effect from the results, the charge density values at the center of pore throat are subtracted from the charge density values along the pore throat. The remaining values show that pore connectivity effects increase with EDL thickness, which is consistent with the earlier proposed 2.7λ long development length. When EDL thickness is 1.5 nm, which yields a non-overlapping case, porosity has almost no effect on the surface charge variation. As the EDL overlap starts, decreasing porosity augments overlap effects but pore connectivity effects become more dominant at high porosity values. This can be clearly seen in the 0.9 porosity case in Figures 5.24(f).

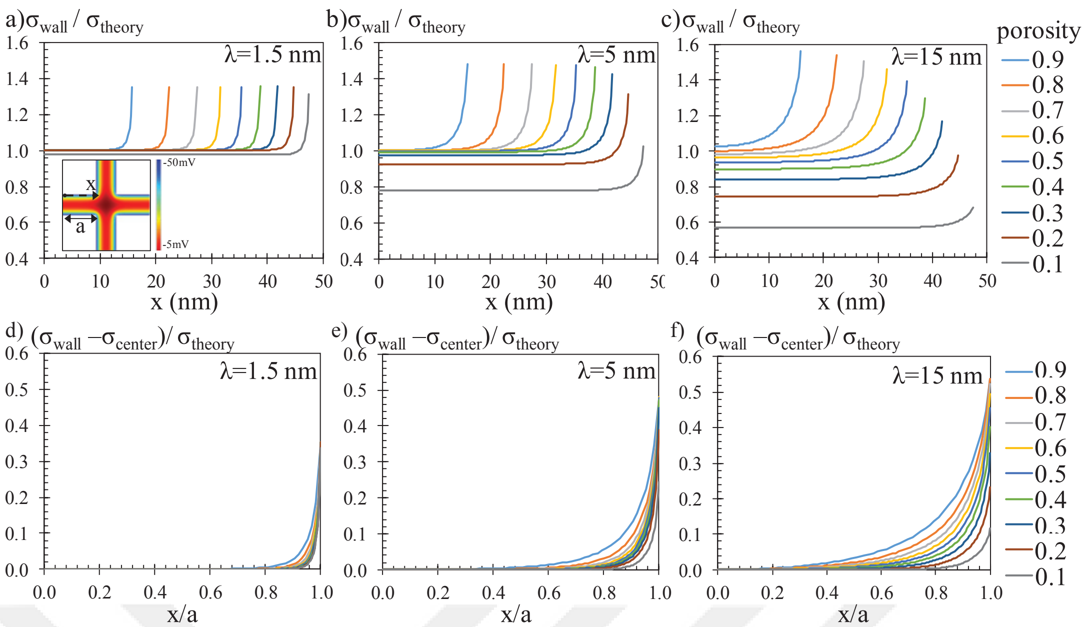

Figure 5.24. Surface charge density distribution on pore surface normalized with flat surface theory at different porosities and at different EDL thicknesses of (a) λ=1.5nm, (b) λ=5nm, and (c) λ=15nm for pore size of H=100nm. (d), (e), and (f) Same charge distributions along axial direction normalized with pore throat length (l_t) when the corresponding center equilibrium charge values were subtracted from the local charge variation.

Next, the average surface charge values and their normalized values with the flat surface theory are calculated and presented in Figures 5.25(a) and (b), respectively; for different porosities, pore sizes and EDL thicknesses. As seen in Figure 5.25(a), the magnitude of the surface charge increases with salt concentration (i.e. thin EDL) and porosity. However, the variations are more significant for smaller pore sizes. More importantly, for low porosities (ϵ=0.1-0.5) the magnitude of the surface charge is lower for small pore sizes than for higher pore sizes. Yet, an opposite behavior is observed for high porosities (ϵ=0.5-0.9). Moreover, normalized charge densities in Figure 5.25(b) show that up to 80% deviations from the flat surface theory are observed high EDL thickness, small pore size and low porosity. As the porosity increases, the average surface charges are higher than the flat surface theory due to the connectivity effects.

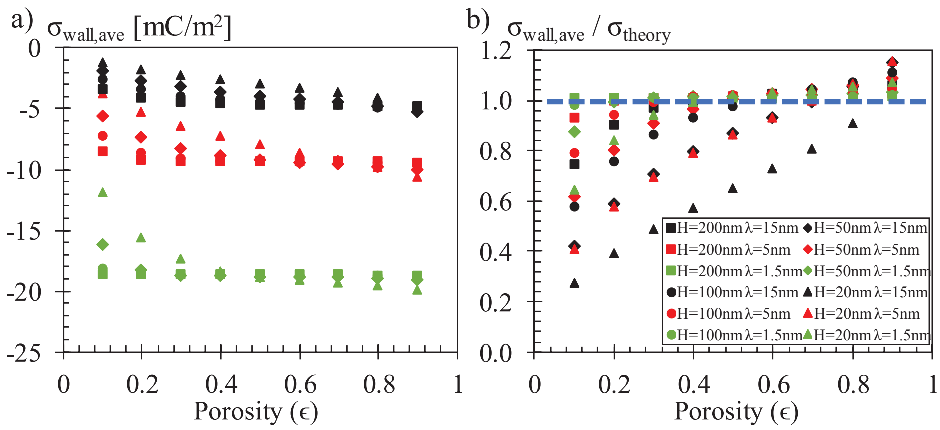

Figure 5.25. (a) Average charge on pore surface as a function of porosity at different pore sizes and EDL thicknesses. (b) Same results when the average surface charge is normalized by the theoretical calculations.

In order to distinguish the EDL overlap and connectivity effects, the surface charge values developing away from corners and average values of the surface charge around the corner regions (as in Figures 5.24(d)-(f)) are estimated. Both effects vary as a function of the pore size to EDL thickness ratio. It should be noted here that porous systems are commonly examined by creating a two dimensional representative volume, which has equal pore height and length. Therefore, if the pore throat is narrow, higher pore lengths form in the representative volume. As a result, EDL overlap effects become dominant compared to the connectivity effects. On the other hand, if wider pore throat is wider, connectivity effects become the charge determining factor. This means that both effects can be described by the ratio of H/λ. Yet, porosity change affects EDL overlap and connectivity in a different manner. Decreasing the porosity yields higher EDL overlaps and weak connectivity effects while an opposite behavior develops for elevated porosity values. Hence, the surface charge developing at the pore center is well-represented by $(H/\lambda)\times\epsilon$ whereas the average of the remaining charge distribution after subtracting the equilibrium center value develops as a function of $(H/\lambda)\times(1/\epsilon)$. Such behaviors can be clearly observed in Figures 5.26(a) and (b) where the results of more than 100 different cases are presented. The general behavior of pore center surface charge in Figure 5.26(a) shows that flat surface theory can accurately predict the surface charge for values of $(H/\lambda)\times\epsilon$ higher than 8. For values lower than 8, the normalized charge decrease exponentially by decreasing $(H/\lambda)\times\epsilon$. Moreover, Figure 5.26(b) shows that connectivity effects can be safely ignored for $(H/\lambda)\times(1/\epsilon)>100$. However, for the case where pore size is 20 nm and EDL thickness is 15 nm, the data diverge from the bulk data. This is because the pore length becomes much shorter than the electrokinetic development length (i.e.

2.7λ) and surface charge at the pore throat center cannot reach an equilibrium. Similar divergence is observed also in Figure 5.26(a) for pore size of 20 nm and EDL thickness of 15 nm.

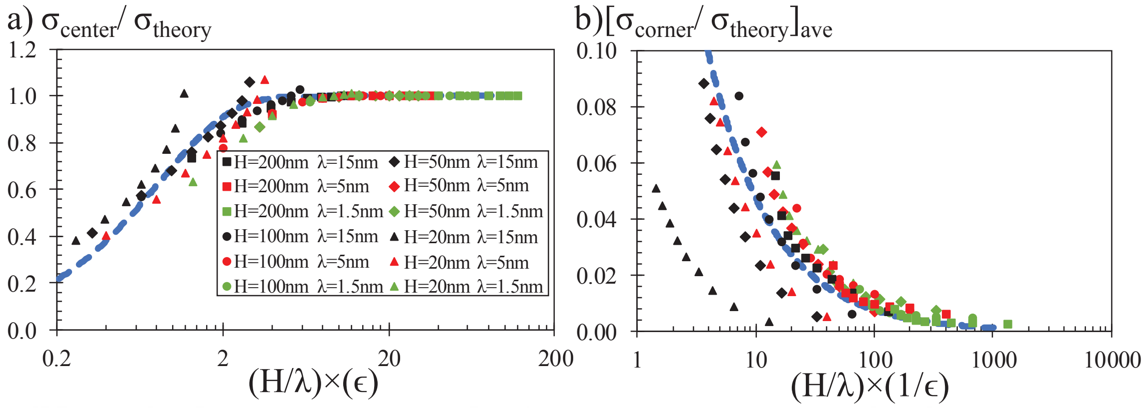

Figure 5.26. (a) Center charge and (b) average of the remaining charge distribution through pore surface as a function of non-dimensional groups of pore size, EDL thickness and porosity.

Finally, an empirical model is developed that can provide a general description for both of these occurrences in mesoporous systems. While an exponential behavior is observed in Figure 5.26(a), where the two asymptotes of the curve is zero and one, the general trend develops as an inverse power of non-dimensional group of $(H/\lambda)\times(1/\epsilon)$. Both mathematical fits are also presented in Figures 5.26(a) and (b) with dashed blue lines. The combination of these mathematical fits forms the equation presented in Equation 5.11, which is a function of pore size, EDL thickness and porosity.

$$\left[\frac{\sigma}{\sigma_{theory}}\right]_{ave} = 1 - \exp\left(-\frac{H\times\varepsilon}{\lambda}\right) + 0.3\left(\frac{H}{\lambda\times\varepsilon}\right)^{-0.8} \qquad (5.11)$$

Above equation is compared with the numerical data in Figure 5.27, where symbols are the results of numerical model and lines are the results of the proposed model. It can be concluded from this figure that this model can well-predict the average surface charge of a mesoporous system for varying EDL thickness, porosity and pore size.

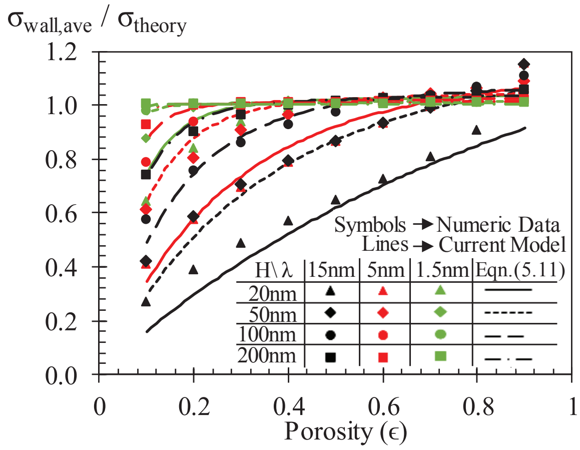

Figure 5.27. Comparison between predictions of new model (Equation 5.11) and numerical calculations.

However, the porous systems cannot be solely characterized by pore size and porosity as discussed earlier in Section 2.5. Therefore, the model proposed in Equation 5.11 should be extended in order to take into account the effects of pore to throat size, R_{pt}. In this context, further simulations are performed at pH=6 and C_{KCl}=0.4 mM, which corresponds to λ=15 nm, to ensure EDL overlap in all cases. First, electrical potential contours for pore sizes of 50 nm and 100 nm with pore the throat size ratios of 2.5, 3, 5 and 10 at ϵ =0.5 are presented in Figure 5.28. For these parameters, corresponding throat sizes vary between 5 nm and 20 nm for a pore size of 50 nm while this variation is between 10 nm and 40 nm for a pore size of 100 nm. In this figure, R_{pt} decreases at the same pore size in each row. In the first row, strong EDL overlap can be observed for H=50 nm, especially when R_{pt} is high. When the pore size is 100 nm, bulk conditions are achieved at the pore center when R_{pt}=2.5. It should be reminded here that all these eight cases are at the same porosity, which validates the idea that porous systems cannot be characterized only by porosity.

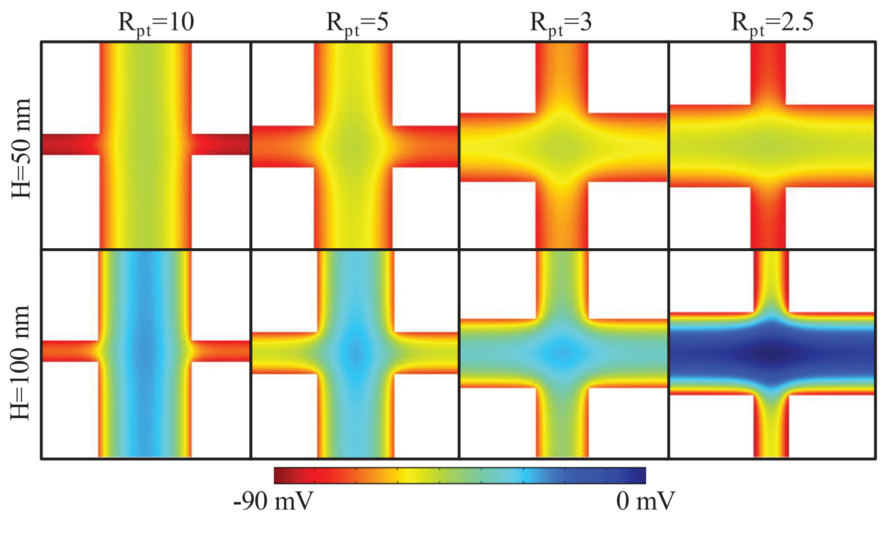

Figure 5.28. Electric potential contours for different pore sizes (H) and pore to throat size ratios (R_{pt}) at ϵ=0.5.

In order to assess the effects of pore to throat connectivity and pore size, normalized charge density values are estimated along the pore throats both in x and y directions. The results are presented in Figure 5.29 for constant porosity of 0.5. Decreasing the pore to throat ratio cause wider pore throats to form in x-direction whereas narrower pore throats are observed in y-direction. Hence, the variation of the surface charge acts in an opposite manner with R_{pt} for x and y directions. Similar to the cases where the aspect ratio of the solid parts is kept unity, EDL overlap and pore to throat connectivity effects have opposite influence on the magnitude of the charge density. As the R_{pt} decreases and H increases, weaker EDL overlap occurs and surface charge density values approach the estimations of the flat surface theory. With increasing R_{pt}, connectivity effects become dominant and charge density reaches above the theoretical predictions around the corners. Such effects present themselves in an opposite behavior on the charge density for the pore throats in y-direction. While the connectivity effects are stronger for low R_{pt}, overlap effects govern the charge density at high R_{pt} values. These results show that connectivity effects are damped for longer throat lengths since the normalized charge density reaches a plateau in a very short distance from the edge. For example, the charge density becomes almost constant for x/a=0.8 at R_{pt}=2.5. However, it propagates into x/a=0.4 at R_{pt}=10 for the pore throats in axial direction. Moreover, the overall charge density behavior also needs to be considered. It can be seen in the first row of Figure 5.29 that the average value of the charge density increases as the R_{pt} increases due to weaker EDL overlap. For high values of R_{pt}, stronger EDL overlap results in an overall decrease in the charge density values.

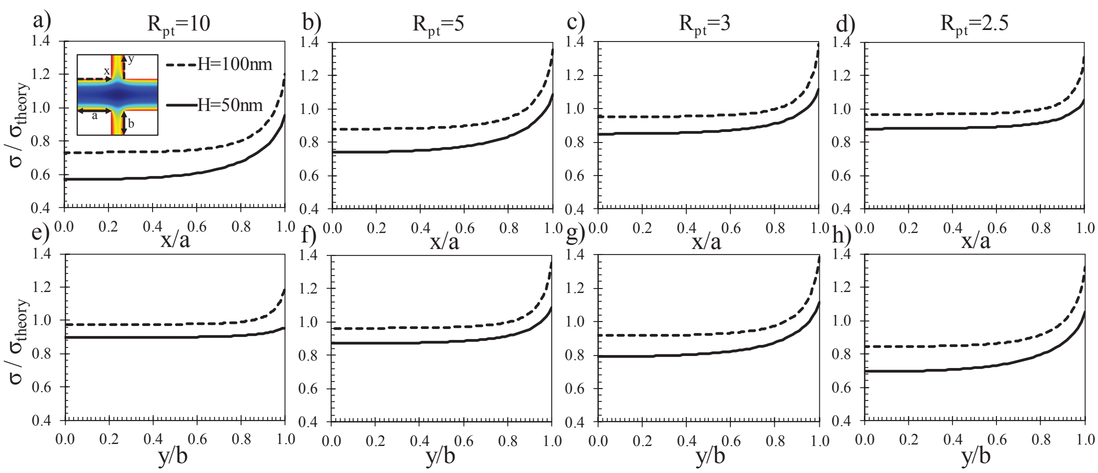

Figure 5.29. (a, b, c, d) Normalized surface charge density distribution along the pore throats in axial direction (x-direction), and (e, f, g, h) in normal direction (y-direction) at porosity, ϵ=0.5.

Next, the average surface charge densities are evaluated for different porosities, pore to throat ratios and pore sizes as presented in Figure 5.30. Due to geometrical constraints, each pore size allows a maximum limit for the value of R_{pt}. For instance, one can achieve a maximum R_{pt} of 10 for a pore size of 50 nm. Therefore, the pore size is increased up to 800 nm to reach an R_{pt} of 200 so that there is enough R_{pt} data for a proper characterization. It should also be noted here that the minimum value of R_{pt} is chosen to be 1.7 to avoid possible molecular size effects. This R_{pt} corresponds to a throat thickness of 4 nm. In Figure 5.30, the results of the cases, where the aspect ratio (AR) of the solid parts are unity, are also presented. For those cases, different R_{pt} values are obtained for each porosity, which makes it impossible to assess the R_{pt} dependence of the charge density. Therefore, different R_{pt} values at certain porosities are defined to form Figure 5.30. Nevertheless, there are particular cases where the results at AR=1 and at AR≠1 coincide due to geometrically similar behavior of mesoporous systems for these cases.

In Figure 5.30(a), average surface charge values for different porosity and R_{pt} values are presented for 50 nm pore size. For the same R_{pt}, the normalized charge density increases with porosity while it decreases with increasing R_{pt} at constant porosity. More importantly, these normalized values reach above unity for some cases due to pore to throat connectivity since connectivity effects increase the magnitude of charge density. Moreover, a stronger dependence on R_{pt} develops and the variation due to porosity decreases as the pore size increases, which can be depicted from Figures 5.30(a)-(d). For instant, the average charge density stays almost constant as the porosity increase at H=800 but almost a 30% decrease is observed due to R_{pt} change. This is because higher R_{pt} values result in long and narrow pore throats that promotes EDL overlap and weakens the connectivity effects.

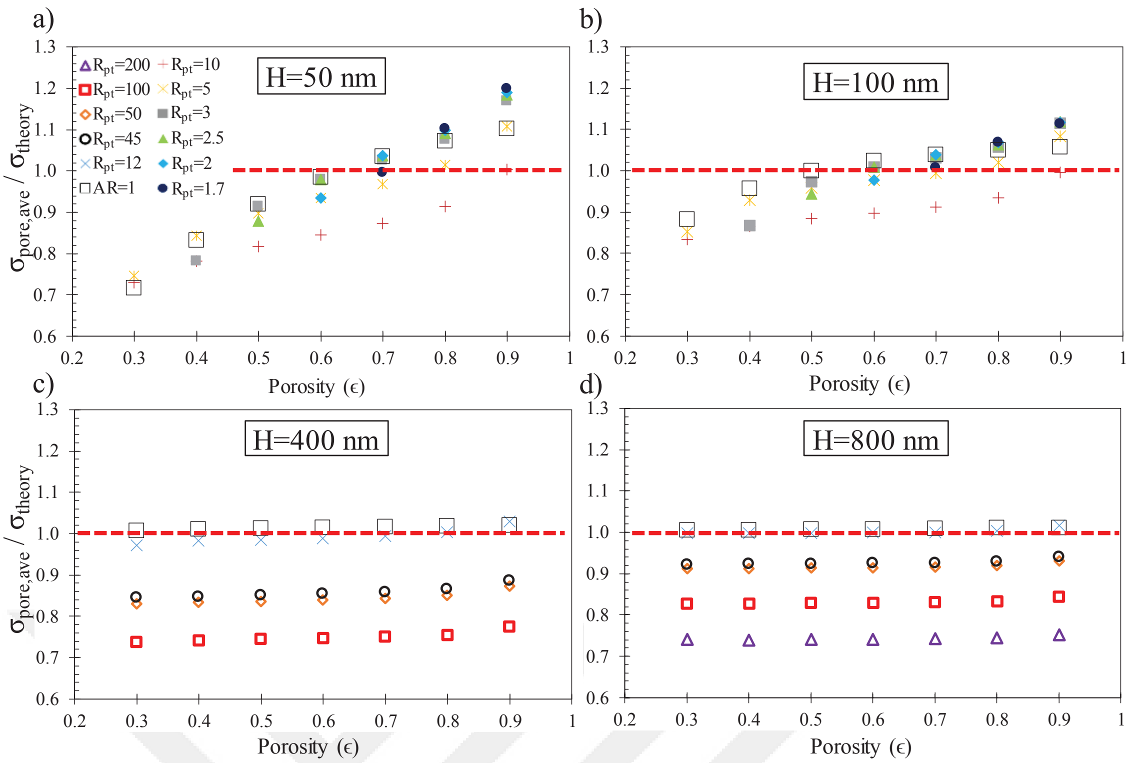

Figure 5.30. The averaged surface charge density of mesoporous silica at pore sizes of a) 50nm, b) 100nm, c) 400nm, d) 800nm for different porosity and pore to throat size ratios. Surface charges were normalized by the theoretical calculations for a flat surface at the corresponding ionic conditions. Results of unity aspect ratio systems (AR=1) for each case are also given.

These findings show that pore to throat connectivity plays an important role on the internal surface charge of mesoporous systems. Therefore, Equation 5.11 is further extended to include the connectivity effects as well. All the results in Figure 5.30(a)-(d) are summarized in Figure 5.31 where the average surface charge values are normalized with those estimated by Equation 5.11 for the corresponding λ/H and ε values. This way, deviation due to connectivity can be calculated. It can be seen in the figure that the resulted values of normalized charge density present an exponential decay as a function of R_{pt}. For low values of R_{pt}, connectivity effects are negligible and Equation 5.11 yields accurate results. As the R_{pt} increases, normalized average surface charge decreases up to 75% from the predictions of Equation 5.11. Consequently, the general trend in Figure 5.31 can be modeled by the following equation.

$$\frac{\sigma_{pore,ave}}{\sigma_{pore,ave(AR=1)}} = 0.25e^{-0.02R_{pt}} + 0.75 \tag{5.12}$$

For R_{pt}<10, Equation 5.12 results in unity indicating that connectivity effects are negligibly small while the average of internal surface charge inside the mesoporous silica decreases with R_{pt} for R_{pt}>10.

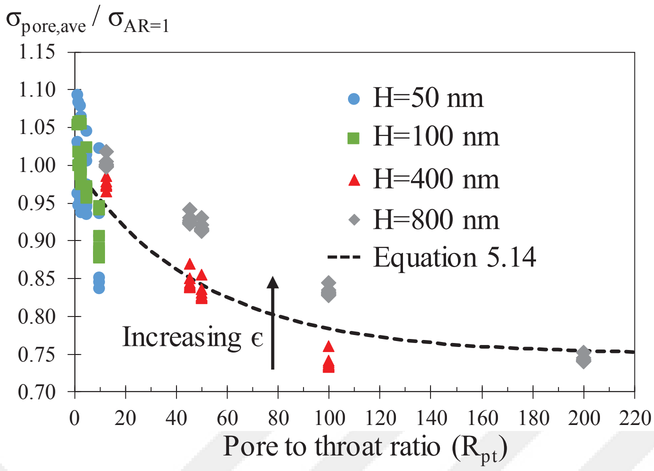

Figure 5.31. Average surface charge densities of mesoporous system (at AR ≠1) normalized by the predictions of Equation (5.14) for the corresponding porosity, pore size and ionic condition.

5.4. Fluid Transport in Mesoporous Media

After resolving surface charge behavior inside the porous systems and accurately characterizing the flow conditions by considering the electroviscous (EV), viscoelectric (VE) and velocity slip effects, the fluid flow through a porous system is examined as a last step of the current study. Hence, a pressure driven fluid flow is created in the system presented in Figure 4.7(d) by applying a pressure difference of 1 bar across the reservoirs.

As a first step, the velocity distributions inside the representative elementary volume are presented in Figure 5.32 for porosity values of 0.1, 0.2, 0.3, 0.4, 0.6 and 0.8 that correspond to throat thicknesses of 5 nm, 10.5 nm, 16 nm, 22 nm, 29 nm, 36 nm, 44 nm and 54 nm. The distributions are calculated first for a simple Poiseuille flow with no electrokinetic effects (first row), then by including only electroviscous effect (second row) and lastly by including both electroviscous and viscoelectric effects (third row). The latter two cases are calculated for a KCl solution of 10 mM at pH=7, which corresponds to an EDL thickness of 3 nm. For such an EDL thickness, both electroviscous and viscoelectric effect play important roles on the flow depending on the porosity and corresponding pore throat sizes. Two major conclusion can be drawn from these velocity contours. First, velocity increases with porosity for the same applied pressure since the resistance to flow decreases at higher porosity values and the porous structure allows the fluid to permeate through the system more easily. Second, if electokinetic effects are considered, the flow velocity decreases due to both electroviscous and viscoelectric effects.

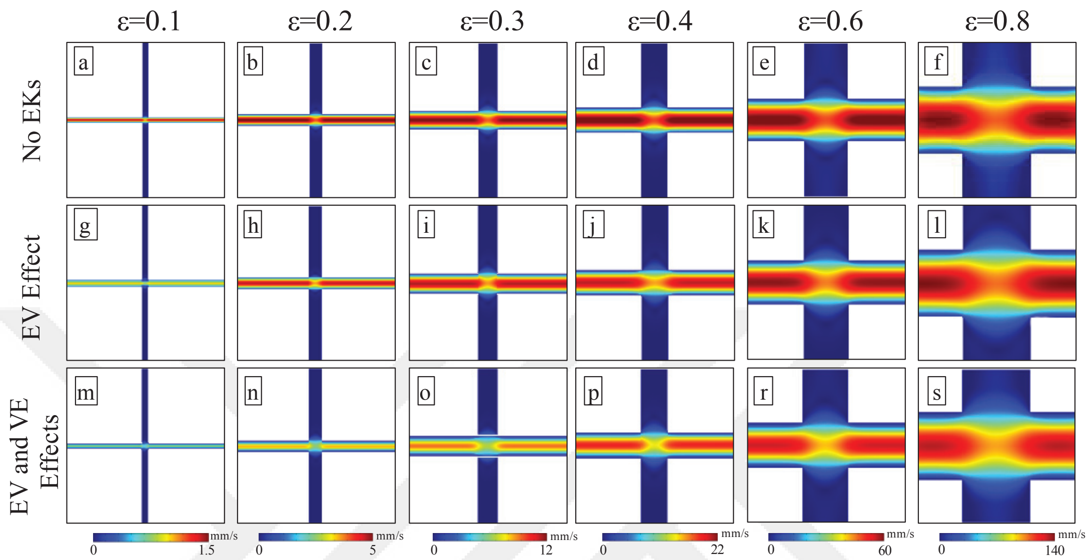

Figure 5.32. Velocity contours at porosity values of 0.1, 0.2, 0.3, 0.4, 0.6 and 0.8 for simple Poiseuille flow conditions (a)-(f), for the flow under electroviscous effect only (g)-(l) and for the flow under both electroviscous and viscoelectric effects (m)-(s).

For the cases in Figure 5.32, the hydraulic conductivity values are then estimated in full porosity range (i.e. ε=0.1-0.8) by using Equation 3.22. In Figure 5.33(a), it can be seen that hydraulic conductivity decreases at certain porosity if electrokinetic effects are introduced into the numerical model although a general increasing trend of conductivity is observed with increasing porosity. Yet, the deviations cannot be clearly captured due to high range of the conductivity. Therefore, the conductivity values for the cases, where electrokinetic effects are considered, are normalized with those of no electrokinetics cases and presented in Figure 5.33(b). The results show that the electroviscous effect is almost negligible on the conductivity, except at very low porosities where small variations are observed. On the other hand, viscoelectric effect is very dominant on the conductivity especially for low porosities. This is because the local viscosity is higher than the bulk viscosity even at the center of the pore throat due to comparable EDL thickness and channel sizes at low porosities. For example, the pore throat thickness is only 5 nm at ε=0.1 where the EDL thickness is 3 nm. As a result, bulk viscosity cannot be achieved at the center of the throat and higher local viscosity is observed, which causes almost 50% decrease in the overall conductivity of the porous system.

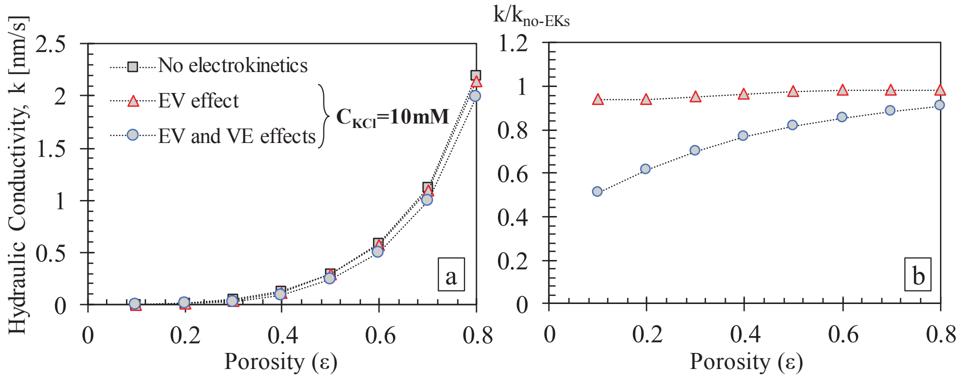

Figure 5.33. a) Comparison of hydraulic conductivity values with and without EK effects and b) hydraulic conductivity values of the EK cases normalized with the no-EK cases.

Next, the velocity distributions for the flows under electokinetic effects are estimated at salt concentrations of 0.94 mM, 10 mM and 93 mM, which yield EDL thicknesses of 10 nm, 3 nm and 1 nm, respectively. The results are presented in Figure 5.34 where decrease in velocity can be clearly observed at high concentrations especially at low porosities.

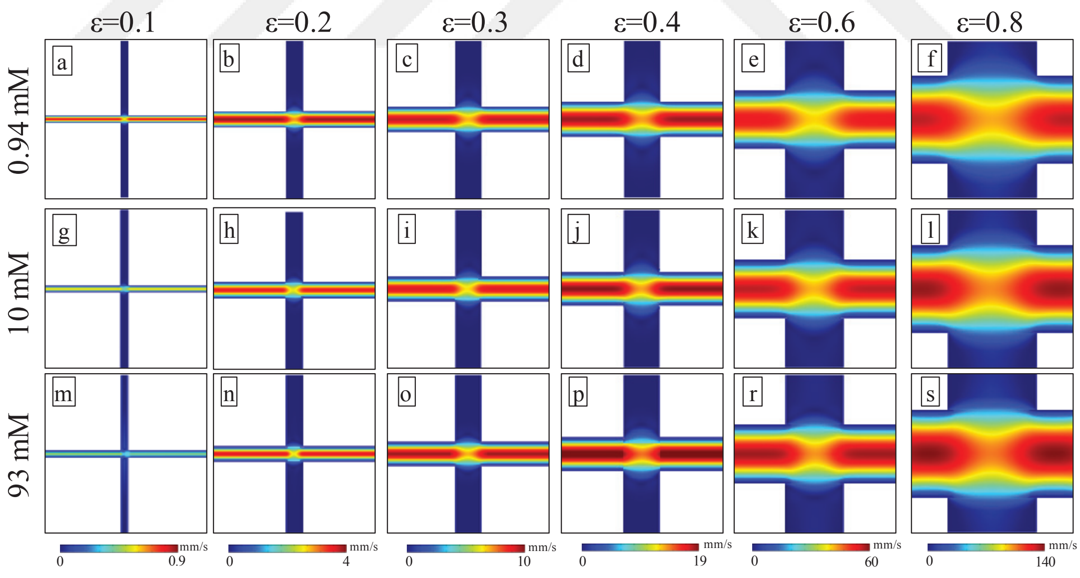

Figure 5.34. Velocity contours at porosity values of 0.1, 0.2, 0.3, 0.4, 0.6 and 0.8 for the flow under both electroviscous and viscoelectric effects (a)-(f) at 0.94 mM (g)-(l) at 10 mM (m)-(s) at 93 mM.

The normalized conductivity values for the cases in Figure 5.34 are presented in Figure 5.35. First of all, the conductivity increases with KCl concentration when only electroviscous effect is considered as in Figure 5.35(a). This is due decreasing λ/H ratio at high concentrations, for which electroviscous effect weakens. Similar findings are also presented in the literature where salt concentration dependence of hydraulic conductivity is examined[25, 157, 158, 161, 180]. However, none of these studies take viscoelectric effect into account, which governs the flow at high concentrations and low porosities. This fact can be clearly seen in Figure 5.35(b). For instance, almost 80% deviation from no EKs cases are observed at 93 mM and ε=0.1.

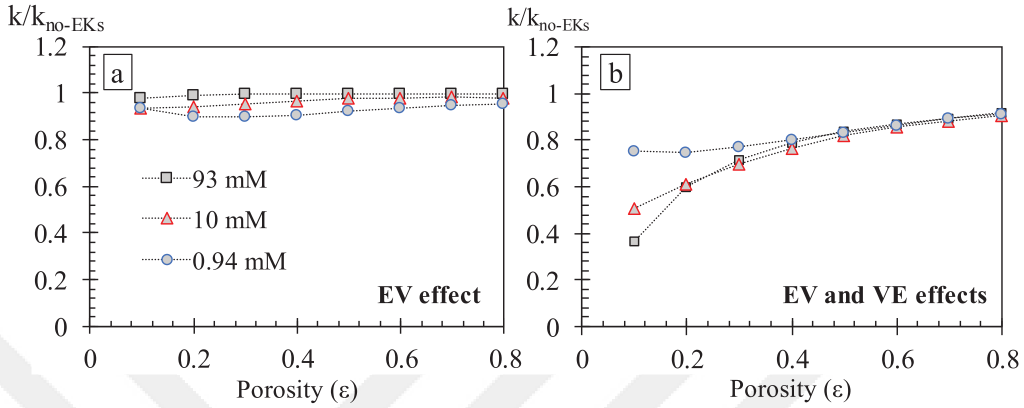

Figure 5.35. Normalized hydraulic conductivity values at porosities 0.1-0.8 for the flow under a) electroviscous effect b) electroviscous and viscoelectric effects

As a final step, velocity slip with slip lengths of 5 nm and 15 nm is applied on the solid walls and the resulting velocity distributions are compared in Figure 5.36 for porosities of 0.1, 0.2, 0.3, 0.4, 0.6 and 0.8. Moreover, the slip length is normalized with H_{Darcy}. The results show that overall velocity increases in the system as the dimensionless slip length, β, increases.

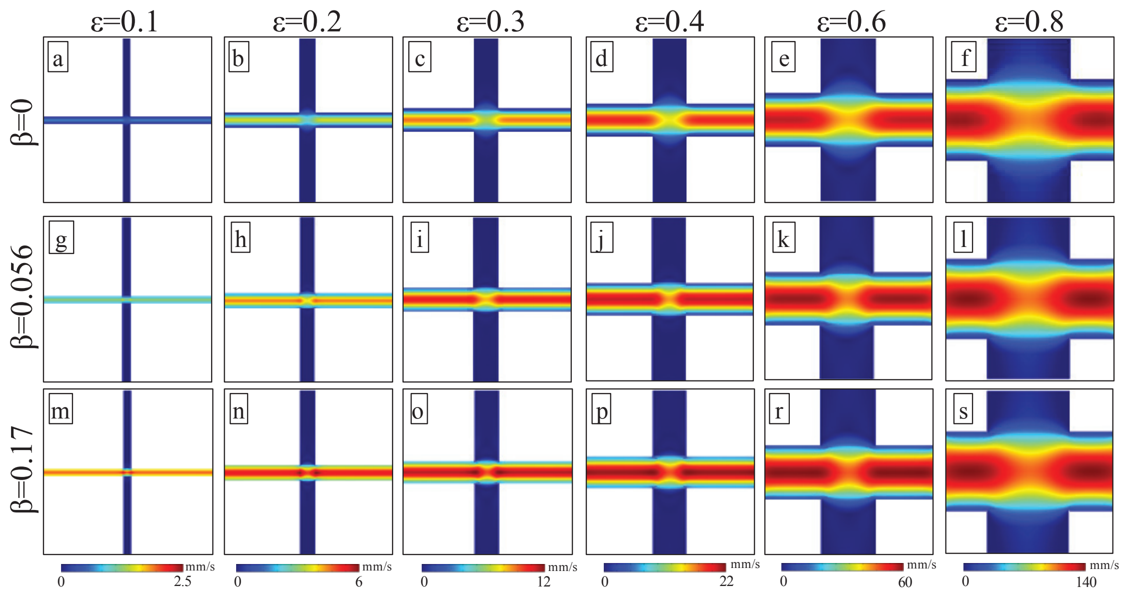

Figure 5.36. Velocity contours at porosity values of 0.1, 0.2, 0.3, 0.4, 0.6 and 0.8 at 10 mM for (a)-(f) β=0 (g)-(l) β=0.056 (m)-(s) β=0.17.

In order to see the effect of velocity slip, the normalized conductivities are calculated and presented in Figure 5.37(a) and (b) for varying normalized slip lengths

(β=0, β=0.056 *and* β=0.17) at constant concentration of 10 mM and for varying concentrations (0.94 mM, 10 mM and 93 mM) at constant slip length of β=0.17, respectively. As expected, the divergence from the no-EKs cases increases with the slip length since velocity slip promotes the fluid flow. Moreover, the porosity dependence is similar to no-slip cases (i.e. 5.38(b)) and conductivity increases with the porosity. At low porosities, electrokinetic effects on the velocity slip become more dominant. Therefore, variation due to concentration decreases for low porosities even if slip length is tripled as can be seen in Figure 5.37(a). On the other hand, since the electroviscous and viscoelectric effects on the velocity slip weakens for decreasing concentrations, the normalized hydraulic conductivity values start approaching back to unity as the porosity decreases. This can be clearly observed in Figure 5.37(b) where almost 90% divergence is observed for 93 mM and this values decreases down to almost 50% at 0.94 mM.

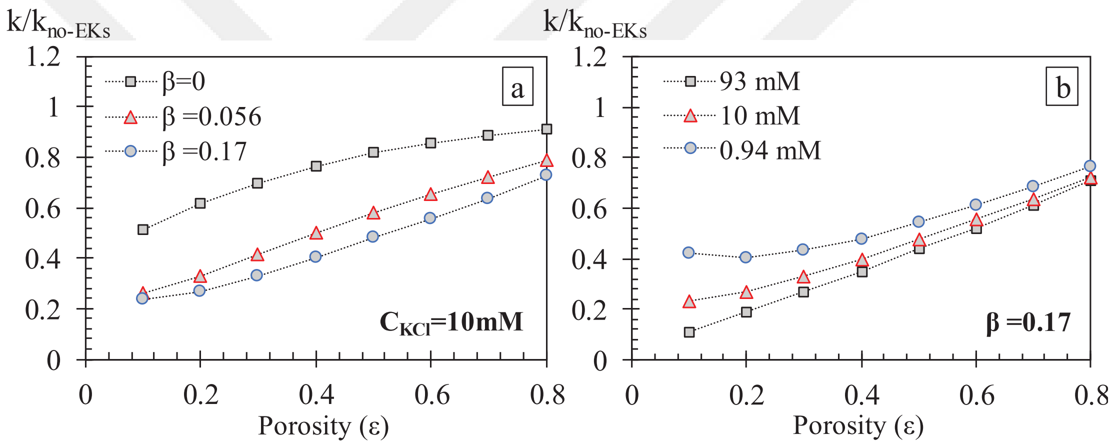

Figure 5.37. Normalized hydraulic conductivity values at porosities 0.1-0.8 for a) slip lengths of β=0, β=0.056 *and* β=0.17 at constant concentration of 10 mM and b) concentrations of 0.94 mM, 10 mM and 93 mM at constant slip length of β=0.17

Another important issue in the current study is to emphasize the importance of employing CR models to the solid surfaces in order to model the porous transport. Therefore, the hydraulic conductivity values at constant surface potential and constant surface charge conditions are calculated for no-slip condition and for β=0.056 case. The results are normalized with the numerical model results with CR boundary condition in order to see the variations for the CP and CC cases. As seen in Figure 5.38(a), almost 5% of difference in hydraulic conductivity is observed when β=0 and the difference increases up to 15% at β=0.056 in Figure 5.38(b). The reason for such a variation is explained in Figure 3.2. Basically, the EDL overlap increases as the porosity decreases. Therefore, ionic conditions at the interface and the resulting surface charge vary. Yet, imposing constant conditions instead of CR behavior yields wrong estimation of surface charge. This cause hydraulic conductivity to be over-predicted by CP condition and under-predicted by CC condition that can be clearly seen in Figure 5.38.

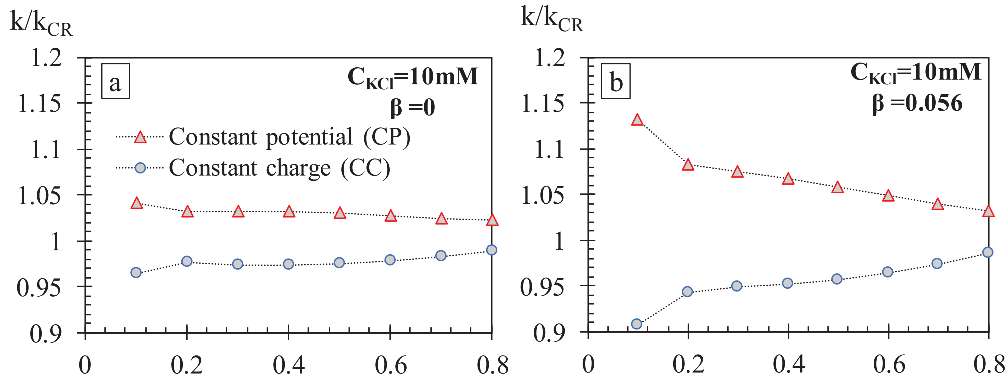

Figure 5.38. Normalized hydraulic conductivity values at porosities 0.1-0.8 for constant potential (CP) and constant charge (CC) cases with a normalized slip length a) β=0 and b) β=0.056.

In this context, a non-dimensional number is proposed that can characterize electroviscous, viscoelectric and slip effects on the hydraulic conductivity. Basically, this non-dimensional number considers EDL overlap ratio through the parameters λ, H_{Darcy}, ε and velocity slip through, β. The normalized conductivity values as a function of this non-dimensional number is presented in Figure 5.39. For constant λ and β, as porosity increases, pore throat size increases causing lower EDL overlaps. Similarly, lower EDL overlaps occur also for decreasing λ at constant ε and β. In both cases, the normalized conductivity values approaches unity, indicating that electrokinetic effects become negligible. Yet, such behavior is very predictable from earlier findings in the current study. More interestingly, for β=0, the dependence of conductivity on the porosity decreases with increasing porosity since the EDL overlap ratio presents an exponential decay with increasing porosity. As β increases, this dependence shows an opposite behavior, especially at thin EDL thicknesses where viscoelectric effect is dominant on the velocity slip. Moreover, strong EDL overlap at low porosities results in dominant electroviscous effect on the slip velocity. Hence, slip velocities are substantially altered at low porosities and then gradually increases at moderate and high porosities. These two mechanisms appear in an exponential term in the proposed equation. For β=0, the exponential function yields a logarithmic increase in the normalized conductivity values while the conductivity increases almost linearly as function of the non-dimensional number for higher β values.

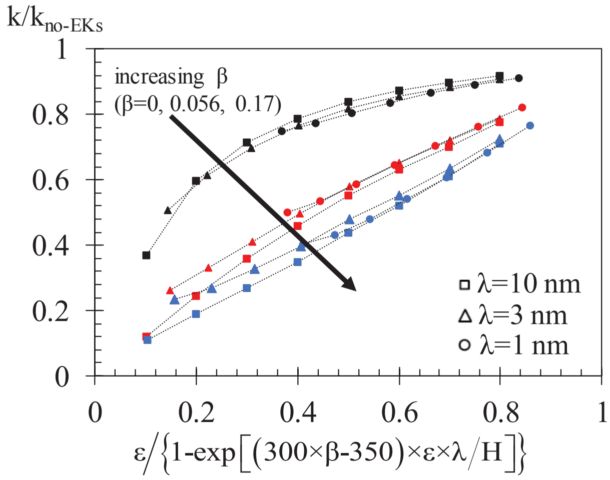

Figure 5.39. Normalized hydraulic conductivity as a function of the proposed non-dimensional number for the flow under electroviscous and viscoelectric effects with EDL thicknesses of 1 nm, 3 nm and 10nm and non-dimensional slip lengths of 0, 0.056 and 0.17.

CHAPTER 6

CONCLUSION

Accurate estimation of fluid transport in micro/nano scale porous media is of prime importance for many promising applications from various fields. Although electrokinetic effects originating due to surface charge play a crucial role on the porous transport through such systems, they are not well-resolved in the current literature. Hence, the current study aims to contribute the community to fill the lacking knowledge on the micro/nano scale porous transport.

Since electrokinetic effects form as a result of surface charge, first step of this study was to characterize the surface charge density at stationary conditions inside a single pore/channel that is connected to reservoirs at both ends. This way, the effects of surface charge and flow conditions can be distinguished. Different channel dimensions and solutions conditions were studied. The results showed that surface charge density develops as a function of not only material properties but also confinement sizes and solution conditions. Local and average charge densities were calculated and the effects of EDL overlap and inlet/outlet effects are analyzed on the surface charging behavior of silica surfaces. It was concluded that surface charge density decreases as the EDL overlap increases. Moreover, the local surface charge values at the inlet/outlet regions of the pore/channel were doubled due to curvature effects and EDL overlap between reservoir and channel in axial direction. These effects were found to be limited within a length of 2.7λ, which was later referred as electrokinetic development length. By using the numerical model results, a phenomenological model for the average surface charge density was proposed, which is a function of EDL thickness, pH, channel length and channel height.

As a next step, a pressure driven flow through this single pore/channel is studied for different salt concentrations and channel lengths. Velocity slip boundary condition, which is mostly studied independent from surface charge, is analyzed by considering its coupled behavior with electroviscous and viscoelectric effects. The results showed that both of these effects reduce the transport due to streaming potential and increase in local viscosity. More interestingly, it was proved by the velocity slip values developing on the charged walls that these effects alter the slip behavior by simply changing the near-wall hydrodynamics inside the pore/channel. When only electroviscous effect was considered, 70% lower velocity slips are observed compared to Poiseuille flow predictions. Further adding viscoelectric effects created almost no-slip condition at high salt concentrations. By considering these results, the slip behavior in wider channels were then analyzed. It was found that although both electroviscous and viscoelectric effects were negligible on the fluid flow for no-slip boundary condition, these effects were found to alter the velocity slip and cause almost no-slip conditions even for a slip length of 100 nm.

Once the surface charge and flow behavior were resolved for a single pore/channel, porous systems were then analyzed. In this regard, internal surface charge density of nanoscale porous systems was calculated for different pore sizes, porosities and ionic concentrations, at stationary conditions. Surface charge decreased as the overlap ratio increased. Moreover, the interaction between pore throat and pore volume increased surface charge. This opposite impact of EDL overlap and pore to throat connectivity was then analyzed for more than 100 different cases and a phenomenological model was proposed that can yield the average surface charge of a porous systems as a function of EDL thickness, pore size and porosity. Yet, these parameters are insufficient to describe the porous structure and pore to throat size also affect the internal charge mechanisms even at constant pore size and porosity. Therefore, the model was further improved to include pore to throat size, R_{pt}.

Lastly, pressure driven fluid flow through a porous system was analyzed. The change in hydraulic conductivity due to electroviscous, viscoelectric and slip effects are characterized for different porosities, ionic conditions and slip lengths. The results showed that the dependence of hydraulic conductivity on the slip length decreases at high concentrations since electrokinetic effects are very dominant on the slip velocity. Moreover, the porosity substantially affects the conductivity, especially at high concentrations. This is mainly because strong electrokinetic effects form due to the increasing EDL overlap as the porosity decreases.

REFERENCES

1. Walter, A. L.; Frind, E. O.; Blowes, D. W.; Ptacek, C. J.; Molson, J. W., Modeling of multicomponent reactive transport in groundwater: 1. Model development and evaluation. *Water Resources Research* **1994,** *30* (11), 3137-3148.

2. Middleton, R. S.; Carey, J. W.; Currier, R. P.; Hyman, J. D.; Kang, Q.; Karra, S.; Jiménez-Martínez, J.; Porter, M. L.; Viswanathan, H. S., Shale gas and non-aqueous fracturing fluids: Opportunities and challenges for supercritical CO2. *Applied Energy* **2015,** *147*, 500-509.

3. Steefel, C. I.; Appelo, C. A. J.; Arora, B.; Jacques, D.; Kalbacher, T.; Kolditz, O.; Lagneau, V.; Lichtner, P. C.; Mayer, K. U.; Meeussen, J. C. L.; Molins, S.; Moulton, D.; Shao, H.; Šimůnek, J.; Spycher, N.; Yabusaki, S. B.; Yeh, G. T., Reactive transport codes for subsurface environmental simulation. *Computational Geosciences* **2014,** *19* (3), 445-478.

4. Spycher, N. F.; Sonnenthal, E. L.; Apps, J. A., Fluid flow and reactive transport around potential nuclear waste emplacement tunnels at Yucca Mountain, Nevada. *Journal of Contaminant Hydrology* **2003,** *62-63*, 653-673.

5. Steefel, C.; Depaolo, D.; Lichtner, P., Reactive transport modeling: An essential tool and a new research approach for the Earth sciences. *Earth and Planetary Science Letters* **2005,** *240* (3-4), 539-558.

6. Ryzhkov, I. I.; Minakov, A. V., Theoretical study of electrolyte transport in nanofiltration membranes with constant surface potential/charge density. *Journal of Membrane Science* **2016,** *520*, 515-528.

7. Daiguji, H.; Yang, P.; Szeri, A. J.; Majumdar, A., Electrochemomechanical Energy Conversion in Nanofluidic Channels. *Nano Letters* **2004,** *4* (12), 2315-2321.

8. Zhang, B.; Wood, M.; Lee, H., A silica nanochannel and its applications in sensing and molecular transport. *Anal Chem* **2009,** *81* (13), 5541-8.

9. Prabhakar, N.; Nareoja, T.; von Haartman, E.; Karaman, D. S.; Jiang, H.; Koho, S.; Dolenko, T. A.; Hanninen, P. E.; Vlasov, D. I.; Ralchenko, V. G.; Hosomi, S.; Vlasov, II; Sahlgren, C.; Rosenholm, J. M., Core-shell designs of photoluminescent nanodiamonds with porous silica coatings for bioimaging and drug delivery II: application. *Nanoscale* **2013,** *5* (9), 3713-22.

10. Rosenholm, J. M.; Sahlgren, C.; Linden, M., Towards multifunctional, targeted drug delivery systems using mesoporous silica nanoparticles--opportunities & challenges. *Nanoscale* **2010,** *2* (10), 1870-83.

11. Medina-Sanchez, M.; Miserere, S.; Merkoci, A., Nanomaterials and lab-on-a-chip technologies. *Lab Chip* **2012,** *12* (11), 1932-43.

12. Khanafer, K.; Cook, K.; Marafie, A., The Role of Porous Media in Modeling Fluid Flow within Hollow Fiber Membranes of the Total Artificial Lung. *J Porous Media* **2012,** *15* (2), 113-122.

13. Darcy, H. P. G., *Dètermination des lois d'ècoulement de l'eau à travers le sable*. 1856.

14. Steefel, C. I.; Lasaga, A. C., A coupled model for transport of multiple chemical species and kinetic precipitation/dissolution reactions with application to reactive flow in single phase hydrothermal systems. *American Journal of Science* **1994,** *294* (5), 529-592.

15. Xie, M.; Mayer, K. U.; Claret, F.; Alt-Epping, P.; Jacques, D.; Steefel, C.; Chiaberge, C.; Simunek, J., Implementation and evaluation of permeability-porosity and tortuosity-porosity relationships linked to mineral dissolution-precipitation. *Computational Geosciences* **2014,** *19* (3), 655-671.

16. Jullien, M.; Raynal, J.; Kohler, É.; Bildstein, O., Physicochemical Reactivity in Clay-Rich Materials: Tools for Safety Assessment. *Oil & Gas Science and Technology* **2006,** *60* (1), 107-120.

17. Barisik, M.; Atalay, S.; Beskok, A.; Qian, S., Size Dependent Surface Charge Properties of Silica Nanoparticles. *The Journal of Physical Chemistry C* **2014,** *118* (4), 1836-1842.

18. Atalay, S.; Barisik, M.; Beskok, A.; Qian, S., Surface Charge of a Nanoparticle Interacting with a Flat Substrate. *The Journal of Physical Chemistry C* **2014,** *118* (20), 10927-10935.

19. Ninham, B. W.; Parsegian, V. A., Electrostatic potential between surfaces bearing ionizable groups in ionic equilibrium with physiologic saline solution. *Journal of Theoretical Biology* **1971,** *31* (3), 405-428.

20. Yeh, L.-H.; Xue, S.; Joo, S. W.; Qian, S.; Hsu, J.-P., Field Effect Control of Surface Charge Property and Electroosmotic Flow in Nanofluidics. *The Journal of Physical Chemistry C* **2012,** *116* (6), 4209-4216.

21. Hunter, R., *Zeta Potential In Colloid Science*. Academic Press: London: 1981.

22. Li, D., *Electrokinetics In Microfluidics*. Elsevier/Academic Press: 2004.

23. Schäfer, B.; Nirschl, H., Distinction between Electrostatic and Electrokinetic Effects on the Permeability of Colloidal Packed Beds. *Chemical Engineering & Technology* **2005,** *28* (8), 862-866.

24. Xu, P.; Zhang, Q.; Qian, H.; Qu, W., Effect of Sodium Chloride Concentration on Saturated Permeability of Remolded Loess. *Minerals* **2020,** *10* (2).

25. Santiago, M.; Pagay, V.; Stroock, A. D., Impact of electroviscosity on the hydraulic conductance of the bordered pit membrane: a theoretical investigation. *Plant Physiol* **2013,** *163* (2), 999-1011.

26. Hsu, W. L.; Daiguji, H.; Dunstan, D. E.; Davidson, M. R.; Harvie, D. J., Electrokinetics of the silica and aqueous electrolyte solution interface: Viscoelectric effects. *Adv Colloid Interface Sci* **2016,** *234*, 108-31.

27. Hsu, W.-L.; Harvie, D. J. E.; Davidson, M. R.; Dunstan, D. E.; Hwang, J.; Daiguji, H., Viscoelectric Effects in Nanochannel Electrokinetics. *The Journal of Physical Chemistry C* **2017,** *121* (37), 20517-20523.

28. Joly, L.; Ybert, C.; Trizac, E.; Bocquet, L., Hydrodynamics within the electric double layer on slipping surfaces. *Phys Rev Lett* **2004,** *93* (25), 257805.

29. Chang, C.-C.; Yang, R.-J.; Wang, M.; Miau, J.-J.; Lebiga, V., Liquid flow retardation in nanospaces due to electroviscosity: Electrical double layer overlap, hydrodynamic slippage, and ambient atmospheric CO2 dissolution. *Physics of Fluids* **2012,** *24* (7).

30. Soong, C. Y.; Hwang, P. W.; Wang, J. C., Analysis of pressure-driven electrokinetic flows in hydrophobic microchannels with slip-dependent zeta potential. *Microfluidics and Nanofluidics* **2009,** *9* (2-3), 211-223.

31. Rezaei, M.; Azimian, A. R.; Pishevar, A. R.; Bonthuis, D. J., Viscous interfacial layer formation causes electroosmotic mobility reversal in monovalent electrolytes. *Phys Chem Chem Phys* **2018,** *20* (35), 22517-22524.

32. Celebi, A. T.; Cetin, B.; Beskok, A., Molecular and Continuum Perspectives on Intermediate and Flow Reversal Regimes in Electroosmotic Transport. *The Journal of Physical Chemistry C* **2019,** *123* (22), 14024-14035.

33. Probstein, R. F., *Physicochemical Hydrodynamics*. John Wiley & Sons: 2005.

34. Karniadakis, G. B. k., A.; Aluru,N., *Microflows And Nanoflows*. Springer-Verlag New York: New York, 2005.

35. Kasianowicz, J. J.; Brandin, E.; Branton, D.; Deamer, D. W., Characterization of individual polynucleotide molecules using a membrane channel. *Proceedings of the National Academy of Sciences* **1996,** *93* (24), 13770-13773.

36. Ravi Kumar, M. N. V.; Bakowsky, U.; Lehr, C. M., Preparation and characterization of cationic PLGA nanospheres as DNA carriers. *Biomaterials* **2004,** *25* (10), 1771-1777.

37. Manzano, M.; Vallet-Regí, M., Mesoporous Silica Nanoparticles for Drug Delivery. *Advanced Functional Materials* **2019,** *30* (2).

38. Kaasalainen, M.; Makila, E.; Riikonen, J.; Kovalainen, M.; Jarvinen, K.; Herzig, K. H.; Lehto, V. P.; Salonen, J., Effect of isotonic solutions and peptide adsorption on zeta potential of porous silicon nanoparticle drug delivery formulations. *Int J Pharm* **2012,** *431* (1-2), 230-6.

39. Kowalczyk, S. W.; Hall, A. R.; Dekker, C., Detection of local protein structures along DNA using solid-state nanopores. *Nano Lett* **2010,** *10* (1), 324-8.

40. Han, A.; Creus, M.; Schurmann, G.; Linder, V.; Ward, T. R.; de Rooij, N. F.; Staufer, U., Label-free detection of single protein molecules and protein-protein interactions using synthetic nanopores. *Anal Chem* **2008,** *80* (12), 4651-8.

41. Li, W.; Liu, J.; Zhao, D., Mesoporous materials for energy conversion and storage devices. *Nature Reviews Materials* **2016,** *1* (6).

42. Huang, J.; Qiao, R.; Sumpter, B. G.; Meunier, V., Effect of diffuse layer and pore shapes in mesoporous carbon supercapacitors. *Journal of Materials Research* **2011,** *25* (08), 1469-1475.

43. Dekker, C., Solid-state nanopores. *Nat Nanotechnol* **2007,** *2* (4), 209-15.

44. Howorka, S.; Cheley, S.; Bayley, H., Sequence-specific detection of individual DNA strands using engineered nanopores. *Nat Biotechnol* **2001,** *19* (7), 636-9.

45. Lan, W.-J.; Holden, D. A.; Liu, J.; White, H. S., Pressure-Driven Nanoparticle Transport across Glass Membranes Containing a Conical-Shaped Nanopore. *The Journal of Physical Chemistry C* **2011,** *115* (38), 18445-18452.

46. Neumcke, B., Ion flux across lipid bilayer membranes with charged surfaces. *Biophysik* **1970,** *6* (3), 231-240.

47. Huang, K.-D.; Yang, R.-J., Electrokinetic behaviour of overlapped electric double layers in nanofluidic channels. *Nanotechnology* **2007,** *18* (11).

48. Kirby, B. J., *Micro-Nanoscale Fluid Mechanics Transport in Microfluidic Devices*. Cornell University: New York, 2010.

49. Israelachvili, J. N.; Adams, G. E., Measurement of forces between two mica surfaces in aqueous electrolyte solutions in the range 0–100 nm. *Journal of the Chemical Society, Faraday Transactions 1: Physical Chemistry in Condensed Phases* **1978,** *74* (0).

50. Pashley, R. M.; Israelachvili, J. N., Dlvo and hydration forces between mica surfaces in Mg2+, Ca2+, Sr2+, and Ba2+ chloride solutions. *Journal of Colloid and Interface Science* **1984,** *97* (2), 446-455.

51. Shubin, V. E.; Kékicheff, P., Electrical Double Layer Structure Revisited via a Surface Force Apparatus: Mica Interfaces in Lithium Nitrate Solutions. *Journal of Colloid and Interface Science* **1993,** *155* (1), 108-123.

52. Chapel, J. P., Electrolyte Species Dependent Hydration Forces between Silica Surfaces. *Langmuir* **1994,** *10* (11), 4237-4243.

53. Butt, H.-J., Measuring electrostatic, van der Waals, and hydration forces in electrolyte solutions with an atomic force microscope. *Biophysical Journal* **1991,** *60* (6), 1438-1444.

54. Kekicheff, P.; Spalla, O., Long-Range Electrostatic Attraction between Similar, Charge-Neutral Walls. *Phys Rev Lett* **1995,** *75* (9), 1851-1854.

55. Pericet-Camara, R.; Papastavrou, G.; Borkovec, M., Effective Charge of Adsorbed Poly(amidoamine) Dendrimers from Direct Force Measurements. *Macromolecules* **2009,** *42* (5), 1749-1758.

56. Yeh, L. H.; Zhang, M.; Qian, S., Ion transport in a pH-regulated nanopore. *Anal Chem* **2013,** *85* (15), 7527-34.

57. Ma, Y.; Yeh, L.-H.; Qian, S., pH-regulated ionic conductance in a nanopore. *Electrochemistry Communications* **2014,** *43*, 91-94.

58. Mei, L.; Yeh, L.-H.; Qian, S., Buffer anions can enormously enhance the electrokinetic energy conversion in nanofluidics with highly overlapped double layers. *Nano Energy* **2017,** *32*, 374-381.

59. Yeh, L.-H.; Ma, Y.; Xue, S.; Qian, S., Gate manipulation of ionic conductance in a nanochannel with overlapped electric double layers. *Sensors and Actuators B: Chemical* **2015,** *215*, 266-271.

60. Ma, Y.; Yeh, L. H.; Lin, C. Y.; Mei, L.; Qian, S., pH-regulated ionic conductance in a nanochannel with overlapped electric double layers. *Anal Chem* **2015,** *87* (8), 4508-14.

61. Yeh, L. H.; Chen, F.; Chiou, Y. T.; Su, Y. S., Anomalous pH-Dependent Nanofluidic Salinity Gradient Power. *Small* **2017,** *13* (48).

62. Ma, Y.; Guo, J.; Jia, L.; Xie, Y., Entrance Effects Induced Rectified Ionic Transport in a Nanopore/Channel. *ACS Sens* **2018,** *3* (1), 167-173.

63. Cheng, Z.; Ning, Z.; Zhang, W.; Ke, S., Theoretical investigation of electroviscous flows in hydrophilic slit nanopores: Effects of ion concentration and pore size. *Physics of Fluids* **2020,** *32* (2).

64. Jing, D.; Bhushan, B., Electroviscous effect on fluid drag in a microchannel with large zeta potential. *Beilstein J Nanotechnol* **2015,** *6*, 2207-16.

65. Yeh, L.-H.; Ma, Y.; Xue, S.; Qian, S., Electroviscous effect on the streaming current in a pH-regulated nanochannel. *Electrochemistry Communications* **2014,** *48*, 77-80.

66. Jia, M.; Kim, T., Multiphysics simulation of ion concentration polarization induced by nanoporous membranes in dual channel devices. *Anal Chem* **2014,** *86* (15), 7360-7.

67. Cao, L.; Xiao, F.; Feng, Y.; Zhu, W.; Geng, W.; Yang, J.; Zhang, X.; Li, N.; Guo, W.; Jiang, L., Anomalous Channel-Length Dependence in Nanofluidic Osmotic Energy Conversion. *Advanced Functional Materials* **2017,** *27* (9).

68. Nosrati, R.; Hadigol, M.; Raisee, M.; Nourbakhsh, A., Numerical Modeling of Electroosmotic Nanoflows with Overlapped Electric Double Layer. *Journal of Computational and Theoretical Nanoscience* **2012,** *9* (12), 2228-2239.

69. Golovnev, A.; Trimper, S., Steady state solution of the Poisson–Nernst–Planck equations. *Physics Letters A* **2010,** *374* (28), 2886-2889.

70. Holt, J. K.; Park, H. G.; Wang, Y.; Stadermann, M.; Artyukhin, A. B.; Grigoropoulos, C. P.; Noy, A.; Bakajin, O., Fast mass transport through sub-2-nanometer carbon nanotubes. *Science* **2006,** *312* (5776), 1034-7.

71. Verweij, H.; Schillo, M. C.; Li, J., Fast mass transport through carbon nanotube membranes. *Small* **2007,** *3* (12), 1996-2004.

72. Sen, T.; Barisik, M., Size dependent surface charge properties of silica nano-channels: double layer overlap and inlet/outlet effects. *Phys Chem Chem Phys* **2018,** *20* (24), 16719-16728.

73. Baldessari, F.; Santiago, J. G., Electrokinetics in nanochannels: part I. Electric double layer overlap and channel-to-well equilibrium. *J Colloid Interface Sci* **2008,** *325* (2), 526-38.

74. Yan, Y.; Sheng, Q.; Wang, C.; Xue, J.; Chang, H.-C., Energy Conversion Efficiency of Nanofluidic Batteries: Hydrodynamic Slip and Access Resistance. *The Journal of Physical Chemistry C* **2013,** *117* (16), 8050-8061.

75. Chang, C.-C.; Yang, R.-J., Electrokinetic energy conversion in micrometer-length nanofluidic channels. *Microfluidics and Nanofluidics* **2009,** *9* (2-3), 225-241.

76. Chein, R.; Liao, C.; Chen, H., Electrokinetic energy conversion efficiency analysis using nanoscale finite-length surface-charged capillaries. *Journal of Power Sources* **2009,** *187* (2), 461-470.

77. Zhang, Y.; He, Y.; Tsutsui, M.; Miao, X. S.; Taniguchi, M., Short channel effects on electrokinetic energy conversion in solid-state nanopores. *Sci Rep* **2017,** *7*, 46661.

78. Vlassiouk, I.; Smirnov, S.; Siwy, Z., Ionic selectivity of single nanochannels. *Nano Lett* **2008,** *8* (7), 1978-85.

79. Lyklema, J., *Fundamentals of Interface and Colloid Science: Solid Liquid Interfaces*. Academic Press: 1995; Vol. 2.

80. Kim, S. I.; Kim, S. J., Analysis of the electroviscous effects on pressure-driven flow in nanochannels using effective ionic concentrations. *Microfluidics and Nanofluidics* **2017,** *22* (1).

81. Hoffmann, J.; Gillespie, D., Ion correlations in nanofluidic channels: effects of ion size, valence, and concentration on voltage- and pressure-driven currents. *Langmuir* **2013,** *29* (4), 1303-17.

82. Elton, G. A. H., Electroviscosity. I. The flow of liquids between surfaces in close proximity. *Proceedings of the Royal Society of London. Series A. Mathematical and Physical Sciences* **1948,** *194* (1037), 259-274.

83. Wang, M.; Kang, Q.; Ben-Naim, E., Modeling of electrokinetic transport in silica nanofluidic channels. *Anal Chim Acta* **2010,** *664* (2), 158-64.

84. Jamaati, J.; Niazmand, H.; Renksizbulut, M., Pressure-driven electrokinetic slip-flow in planar microchannels. *Int J Therm Sci* **2010,** *49* (7), 1165-1174.

85. Andrade, E. N. D. C. D., C., The effect of an electric field on the viscosity of liquids. *Proceedings of the Royal Society of London. Series A. Mathematical and Physical Sciences* **1946,** *187* (1010), 296-337.

86. Andrade, E. N. D. C. D., C., The effect of an electric field on the viscosity of liquids. II. *Proceedings of the Royal Society of London. Series A. Mathematical and Physical Sciences* **1951,** *204* (1079), 449-464.

87. Zhao, C.; Yang, C., Electrokinetics of non-Newtonian fluids: a review. *Adv Colloid Interface Sci* **2013,** *201-202*, 94-108.

88. Jing, D.; Song, J.; Sui, Y. I., Hydraulic and Thermal Performances of Laminar Flow in Fractal Treelike Branching Microchannel Network with Wall Velocity Slip. *Fractals* **2020,** *28* (02).

89. Jing, D.; Song, S.; Pan, Y.; Wang, X., Size dependences of hydraulic resistance and heat transfer of fluid flow in elliptical microchannel heat sinks with boundary slip. *International Journal of Heat and Mass Transfer* **2018,** *119*, 647-653.

90. Ren, Y.; Stein, D., Slip-enhanced electrokinetic energy conversion in nanofluidic channels. *Nanotechnology* **2008,** *19* (19), 195707.

91. Bandopadhyay, A.; Hossain, S. S.; Chakraborty, S., Ionic size dependent electroviscous effects in ion-selective nanopores. *Langmuir* **2014,** *30* (24), 7251-8.

92. Jing, D.; Pan, Y.; Wang, X., The non-monotonic overlapping EDL-induced electroviscous effect with surface charge-dependent slip and its size dependence. *International Journal of Heat and Mass Transfer* **2017,** *113*, 32-39.

93. Navier, C. L. M. H., Mémoire sur les lois du mouvement des fluides. *Mem. Acad. Sci. Inst.* **1823**, 389-416.

94. Celebi, A. T.; Barisik, M.; Beskok, A., Surface charge-dependent transport of water in graphene nano-channels. *Microfluidics and Nanofluidics* **2017,** *22* (1).

95. Bocquet, L.; Barrat, J. L., Hydrodynamic boundary conditions and correlation functions of confined fluids. *Phys Rev Lett* **1993,** *70* (18), 2726-2729.

96. Bocquet, L.; Barrat, J. L., Hydrodynamic boundary conditions, correlation functions, and Kubo relations for confined fluids. *Phys Rev E Stat Phys Plasmas Fluids Relat Interdiscip Topics* **1994,** *49* (4), 3079-3092.

97. Barrat, J.-L.; Bocquet, L., Large Slip Effect at a Nonwetting Fluid-Solid Interface. *Physical Review Letters* **1999,** *82* (23), 4671-4674.

98. Marry, V.; DufrÊChe, J. F.; Jardat, M.; Turq, P., Equilibrium and electrokinetic phenomena in charged porous media from microscopic and mesoscopic models: electro-osmosis in montmorillonite. *Molecular Physics* **2003,** *101* (20), 3111-3119.

99. Huang, D. M.; Sendner, C.; Horinek, D.; Netz, R. R.; Bocquet, L., Water slippage versus contact angle: a quasiuniversal relationship. *Phys Rev Lett* **2008,** *101* (22), 226101.

100. Sofos, F.; Karakasidis, T.; Liakopoulos, A., Parameters Affecting Slip Length at the Nanoscale. *Journal of Computational and Theoretical Nanoscience* **2013,** *10* (3), 648-650.

101. Ramos-Alvarado, B.; Kumar, S.; Peterson, G. P., Hydrodynamic slip in silicon nanochannels. *Phys Rev E* **2016,** *93* (3), 033117.

102. Zhang, C.; Chen, Y., Slip behavior of liquid flow in rough nanochannels. *Chemical Engineering and Processing: Process Intensification* **2014,** *85*, 203-208.

103. Yen, T.-H.; Soong, C.-Y., Effective boundary slip and wetting characteristics of water on substrates with effects of surface morphology. *Molecular Physics* **2015,** *114* (6), 797-809.

104. Barisik, M.; Beskok, A., Wetting characterisation of silicon (1,0,0) surface. *Molecular Simulation* **2013,** *39* (9), 700-709.

105. Nguyen, C. T.; Barisik, M.; Kim, B., Wetting of chemically heterogeneous striped surfaces: Molecular dynamics simulations. *AIP Advances* **2018,** *8* (6).

106. Joly, L.; Ybert, C.; Trizac, E.; Bocquet, L., Liquid friction on charged surfaces: from hydrodynamic slippage to electrokinetics. *J Chem Phys* **2006,** *125* (20), 204716.

107. Malekidelarestaqi, M.; Mansouri, A.; Chini, S. F., Electrokinetic energy conversion in a finite length superhydrophobic microchannel. *Chemical Physics Letters* **2018,** *703*, 72-79.

108. Jing, D.; Bhushan, B., Effect of boundary slip and surface charge on the pressure-driven flow. *J Colloid Interface Sci* **2013,** *392*, 15-26.

109. Pan, Y.; Bhushan, B., Role of surface charge on boundary slip in fluid flow. *J Colloid Interface Sci* **2013,** *392*, 117-121.

110. Rahmati, A. R.; Akbari, O. A.; Marzban, A.; Toghraie, D.; Karimi, R.; Pourfattah, F., Simultaneous investigations the effects of non-Newtonian nanofluid flow in different volume fractions of solid nanoparticles with slip and no-slip boundary conditions. *Thermal Science and Engineering Progress* **2018,** *5*, 263-277.

111. Niu, J.; Fu, C.; Tan, W., Slip-flow and heat transfer of a non-newtonian nanofluid in a microtube. *PLoS One* **2012,** *7* (5), e37274.

112. Ferrás, L. L.; Nóbrega, J. M.; Pinho, F. T., Analytical solutions for Newtonian and inelastic non-Newtonian flows with wall slip. *Journal of Non-Newtonian Fluid Mechanics* **2012,** *175-176*, 76-88.

113. Sunarso, A.; Yamamoto, T.; Mori, N., Numerical Analysis of Wall Slip Effects on Flow of Newtonian and Non-Newtonian Fluids in Macro and Micro Contraction Channels. *Journal of Fluids Engineering* **2007,** *129* (1), 23-30.

114. Ellahi, R., Effects of the slip boundary condition on non-Newtonian flows in a channel. *Communications in Nonlinear Science and Numerical Simulation* **2009,** *14* (4), 1377-1384.

115. Lu, F.; Wu, S. H.; Hung, Y.; Mou, C. Y., Size effect on cell uptake in well-suspended, uniform mesoporous silica nanoparticles. *Small* **2009,** *5* (12), 1408-13.

116. Trewyn, B. G.; Nieweg, J. A.; Zhao, Y.; Lin, V. S. Y., Biocompatible mesoporous silica nanoparticles with different morphologies for animal cell membrane penetration. *Chemical Engineering Journal* **2008,** *137* (1), 23-29.

117. Zhang, Q.; Liu, F.; Nguyen, K. T.; Ma, X.; Wang, X.; Xing, B.; Zhao, Y., Multifunctional Mesoporous Silica Nanoparticles for Cancer-Targeted and Controlled Drug Delivery. *Advanced Functional Materials* **2012,** *22* (24), 5144-5156.

118. Bowen, W. R.; Doneva, T. A.; Stoton, J. A. G., The use of atomic force microscopy to quantify membrane surface electrical properties. *Colloids and Surfaces A: Physicochemical and Engineering Aspects* **2002,** *201* (1-3), 73-83.

119. Agboola, O.; Maree, J.; Mbaya, R.; Kolesnikov, A.; Sadiku, R.; Verliefde, A.; D'Haese, A., Microscopical characterizations of nanofiltration membranes for the removal of nickel ions from aqueous solution. *Korean Journal of Chemical Engineering* **2015,** *32* (4), 731-742.

120. Hilal, N.; Al-Zoubi, H.; Darwish, N. A.; Mohammad, A. W., Characterisation of nanofiltration membranes using atomic force microscopy. *Desalination* **2005,** *177* (1-3), 187-199.

121. Lee, K. P.; Arnot, T. C.; Mattia, D., A review of reverse osmosis membrane materials for desalination—Development to date and future potential. *Journal of Membrane Science* **2011,** *370* (1-2), 1-22.

122. Buonomenna, M. G., Nano-enhanced reverse osmosis membranes. *Desalination* **2013,** *314*, 73-88.

123. Yakin, F. E.; Barisik, M.; Sen, T., Pore Size and Porosity Dependent Zeta Potentials of Mesoporous Silica Nanoparticles. *The Journal of Physical Chemistry C* **2020,** *124* (36), 19579-19587.

124. Zhou, Y.; Quan, G.; Wu, Q.; Zhang, X.; Niu, B.; Wu, B.; Huang, Y.; Pan, X.; Wu, C., Mesoporous silica nanoparticles for drug and gene delivery. *Acta Pharm Sin B* **2018,** *8* (2), 165-177.

125. Chowdhury, S., Pore size and surface chemistry effects on the transport of hydrophobic and hydrophilic solvents through mesoporous γ-alumina and silica MCM-48. *Journal of Membrane Science* **2003,** *225* (1-2), 177-186.

126. Hartmann, M., Ordered Mesoporous Materials for Bioadsorption and Biocatalysis. *Chemistry of Materials* **2005,** *17* (18), 4577-4593.

127. Takahashi, H.; Li, B.; Sasaki, T.; Miyazaki, C.; Kajino, T.; Inagaki, S., Immobilized enzymes in ordered mesoporous silica materials and improvement of their stability and catalytic activity in an organic solvent. *Microporous and Mesoporous Materials* **2001,** *44-45*, 755-762.

128. Moerz, S. T.; Huber, P., pH-Dependent Selective Protein Adsorption into Mesoporous Silica. *The Journal of Physical Chemistry C* **2015,** *119* (48), 27072-27079.

129. Cheah, W.-K.; Sim, Y.-L.; Yeoh, F.-Y., Amine-functionalized mesoporous silica for urea adsorption. *Materials Chemistry and Physics* **2016,** *175*, 151-157.

130. Kim H.J., L. J. E., Shul Y.G., Han H., Mesoporous silica: Polymer composite membrane for direct methanol fuel cell. In *Studies in Surface Science and Catalysis* 2004; Vol. Volume 154, Part C, pp 3036-3043.

131. Lesel, B. K.; Ko, J. S.; Dunn, B.; Tolbert, S. H., Mesoporous LixMn2O4 Thin Film Cathodes for Lithium-Ion Pseudocapacitors. *ACS Nano* **2016,** *10* (8), 7572-81.

132. Wang, F.; Yang, J.; Wu, K., Mesoporous silica-based electrochemical sensor for sensitive determination of environmental hormone bisphenol A. *Anal Chim Acta* **2009,** *638* (1), 23-8.

133. Jimbo, T.; Tanioka, A.; Minoura, N., Characterization of an Amphoteric-Charged Layer Grafted to the Pore Surface of a Porous Membrane. *Langmuir* **1998,** *14* (25), 7112-7118.

134. Jimbo, T.; Higa, M.; Minoura, N.; Tanioka, A., Surface Characterization of Poly(acrylonitrile) Membranes Graft-Polymerized with Ionic Monomers As Revealed by ζ Potential Measurement. *Macromolecules* **1998,** *31* (4), 1277-1284.

135. Causserand, C.; Nyström, M.; Aimar, P., Study of streaming potentials of clean and fouled ultrafiltration membranes. *Journal of Membrane Science* **1994,** *88* (2-3), 211-222.

136. Nyström, M.; Pihlajamäki, A.; Ehsani, N., Characterization of ultrafiltration membranes by simultaneous streaming potential and flux measurements. *Journal of Membrane Science* **1994,** *87* (3), 245-256.

137. Teixeira, M.; Rosa, M.; Nystrom, M., The role of membrane charge on nanofiltration performance. *Journal of Membrane Science* **2005,** *265* (1-2), 160-166.

138. Revil, A.; Pezard, P. A.; Glover, P. W. J., Streaming potential in porous media: 1. Theory of the zeta potential. *Journal of Geophysical Research: Solid Earth* **1999,** *104* (B9), 20021-20031.

139. Revil, A.; Schwaeger, H.; Cathles, L. M.; Manhardt, P. D., Streaming potential in porous media: 2. Theory and application to geothermal systems. *Journal of Geophysical Research: Solid Earth* **1999,** *104* (B9), 20033-20048.

140. Ishido, T.; Pritchett, J. W., Numerical simulation of electrokinetic potentials associated with subsurface fluid flow. *Journal of Geophysical Research: Solid Earth* **1999,** *104* (B7), 15247-15259.

141. Glover, P. W. J.; Walker, E.; Jackson, M. D., Streaming-potential coefficient of reservoir rock: A theoretical model. *Geophysics* **2012,** *77* (2), D17-D43.

142. Abendroth, R., Surface charge development of porous silica in aqueous solution. *The Journal of Physical Chemistry* **1972,** *76* (18), 2547-2549.

143. Karlsson, M.; Craven, C.; Dove, P. M.; Casey, W. H., Surface Charge Concentrations on Silica in Different 1.0 M Metal-Chloride Background Electrolytes and Implications for Dissolution Rates. *Aquatic Geochemistry* **2001,** *7* (1), 13-32.

144. Salis, A.; Parsons, D. F.; Bostrom, M.; Medda, L.; Barse, B.; Ninham, B. W.; Monduzzi, M., Ion specific surface charge density of SBA-15 mesoporous silica. *Langmuir* **2010,** *26* (4), 2484-90.

145. Martínez Casillas, D. C.; Longinotti, M. P.; Bruno, M. M.; Vaca Chávez, F.; Acosta, R. H.; Corti, H. R., Diffusion of Water and Electrolytes in Mesoporous Silica with a Wide Range of Pore Sizes. *The Journal of Physical Chemistry C* **2018,** *122* (6), 3638-3647.

146. Goyne, K. W.; Zimmerman, A. R.; Newalkar, B. L.; Komarneni, S.; Brantley, S. L.; Chorover, J., Surface Charge of Variable Porosity Al2O3(s) and SiO2(s) Adsorbents. *Journal of Porous Materials* **2002,** *9* (4), 243-256.

147. Bowen, W. R.; Hughes, D. T., Properties of microfiltration membranes: The surface electrochemistry of anodic film membranes. *Journal of Colloid and Interface Science* **1991,** *143* (1), 252-265.

148. Valetti, S.; Feiler, A.; Trulsson, M., Bare and Effective Charge of Mesoporous Silica Particles. *Langmuir* **2017,** *33* (29), 7343-7351.

149. Zhang, X.; Tartakovsky, D. M., Effective Ion Diffusion in Charged Nanoporous Materials. *Journal of The Electrochemical Society* **2017,** *164* (4), E53-E61.

150. Cooper, S. J.; Bertei, A.; Finegan, D. P.; Brandon, N. P., Simulated impedance of diffusion in porous media. *Electrochimica Acta* **2017,** *251*, 681-689.

151. Jiang, Z.; Stein, D., Charge regulation in nanopore ionic field-effect transistors. *Phys Rev E Stat Nonlin Soft Matter Phys* **2011,** *83* (3 Pt 1), 031203.

152. Boon, N.; van Roij, R., Charge reversal of moisturous porous silica colloids by take-up of protons. *J Colloid Interface Sci* **2012,** *385* (1), 66-72.

153. Le Ravalec, M.; Darot, M.; Reuschlé, T.; Guéguen, Y., Transport properties and microstructural characteristics of a thermally cracked mylonite. *pure and applied geophysics* **1996,** *146* (2), 207-227.

154. Nelson, P. H., Pore-throat sizes in sandstones, tight sandstones, and shales. *AAPG Bulletin* **2009,** *93* (3), 329-340.

155. Song, Y.-Q., Pore sizes and pore connectivity in rocks using the effect of internal field. *Magnetic Resonance Imaging* **2001,** *19* (3-4), 417-421.

156. Javadpour, F.; McClure, M.; Naraghi, M. E., Slip-corrected liquid permeability and its effect on hydraulic fracturing and fluid loss in shale. *Fuel* **2015,** *160*, 549-559.

157. Nguyen, X. P.; Cui, Y. J.; Tang, A. M.; Deng, Y. F.; Li, X. L.; Wouters, L., Effects of pore water chemical composition on the hydro-mechanical behavior of natural stiff clays. *Engineering Geology* **2013,** *166*, 52-64.

158. Jo, H. Y.; Katsumi, T.; Benson, C. H.; Edil, T. B., Hydraulic Conductivity and Swelling of Nonprehydrated GCLs Permeated with Single-Species Salt Solutions. *Journal of Geotechnical and Geoenvironmental Engineering* **2001,** *127* (7), 557-567.

159. Revil, A.; Pessel, M., Electroosmotic flow and the validity of the classical Darcy equation in silty shales. *Geophysical Research Letters* **2002,** *29* (9), 14-1-14-4.

160. Shen, C.; Zhu, J.; Gu, W., Prediction Method for Hydraulic Conductivity considering the Effect of Sizes of Ellipsoid Soil Particles from the Microscopic Perspective. *Advances in Civil Engineering* **2019,** *2019*, 1-24.

161. Yilmaz, G.; Yetimoglu, T.; Arasan, S., Hydraulic conductivity of compacted clay liners permeated with inorganic salt solutions. *Waste Manag Res* **2008,** *26* (5), 464-73.

162. AHUJA, L. R.; CASSEL, D. K.; BRUCE, R. R.; BARNES, B. B., EVALUATION OF SPATIAL DISTRIBUTION OF HYDRAULIC CONDUCTIVITY USING EFFECTIVE POROSITY DATA. *Soil Science* **1989,** *148* (6), 404-411.

163. Koponen, A.; Kataja, M.; Timonen, J., Permeability and effective porosity of porous media. *Physical Review E* **1997,** *56* (3), 3319-3325.

164. Zhang, L.; Wang, M., Modeling of electrokinetic reactive transport in micropore using a coupled lattice Boltzmann method. *Journal of Geophysical Research: Solid Earth* **2015,** *120* (5), 2877-2890.

165. Municchi, F.; Icardi, M., Macroscopic models for filtration and heterogeneous reactions in porous media. *Advances in Water Resources* **2020,** *141*.

166. Bildstein, O.; Claret, F.; Frugier, P., RTM for Waste Repositories. *Reviews in Mineralogy and Geochemistry* **2019,** *85* (1), 419-457.

167. Yeh, G.; Tripathi, V. *HYDROGEOCHEM: A coupled model of HYDROlogic transport and GEOCHEMical equilibria in reactive multicomponent systems*; Oak Ridge National Lab., TN (USA): 1990.

168. Kaufmann, G.; Romanov, D.; Hiller, T., Modeling three-dimensional karst aquifer evolution using different matrix-flow contributions. *Journal of Hydrology* **2010,** *388* (3-4), 241-250.

169. Cheng, A. H.-D., Porochemoelasticity. In *Poroelasticity*, Springer: 2016; pp 703-773.

170. Seigneur, N.; Mayer, K. U.; Steefel, C. I., Reactive Transport in Evolving Porous Media. *Reviews in Mineralogy and Geochemistry* **2019,** *85* (1), 197-238.

171. Hartmann, A.; Goldscheider, N.; Wagener, T.; Lange, J.; Weiler, M., Karst water resources in a changing world: Review of hydrological modeling approaches. *Reviews of Geophysics* **2014,** *52* (3), 218-242.

172. Charlet, L.; Alt-Epping, P.; Wersin, P.; Gilbert, B., Diffusive transport and reaction in clay rocks: A storage (nuclear waste, CO2, H2), energy (shale gas) and water quality issue. *Advances in Water Resources* **2017,** *106*, 39-59.

173. Mazurek, M.; Alt-Epping, P.; Bath, A.; Gimmi, T.; Niklaus Waber, H.; Buschaert, S.; Cannière, P. D.; Craen, M. D.; Gautschi, A.; Savoye, S.; Vinsot, A.; Wemaere, I.; Wouters, L., Natural tracer profiles across argillaceous formations. *Applied Geochemistry* **2011,** *26* (7), 1035-1064.

174. Van Loon, L. R.; Glaus, M. A.; Müller, W., Anion exclusion effects in compacted bentonites: towards a better understanding of anion diffusion. *Applied Geochemistry* **2007,** *22* (11), 2536-2552.

175. Godinez-Brizuela, O. E.; Niasar, V. J., Simultaneous pressure and electro-osmosis driven flow in charged porous media: Pore-scale effects on mixing and dispersion. *J Colloid Interface Sci* **2020,** *561*, 162-172.

176. Bartels, W. B.; Mahani, H.; Berg, S.; Hassanizadeh, S. M., Literature review of low salinity waterflooding from a length and time scale perspective. *Fuel* **2019,** *236*, 338-353.

177. Suijkerbuijk, B.; Sorop, T.; Parker, A.; Masalmeh, S.; Chmuzh, I.; Karpan, V.; Volokitin, Y.; Skripkin, A. In *Low salinity waterflooding at west-salym: Laboratory experiments and field forecasts*, SPE Improved Oil Recovery Symposium, Society of Petroleum Engineers: 2014.

178. Maes, J.; Geiger, S., Direct pore-scale reactive transport modelling of dynamic wettability changes induced by surface complexation. *Advances in Water Resources* **2018,** *111*, 6-19.

179. Salehi, M. M.; Omidvar, P.; Naeimi, F., Salinity of injection water and its impact on oil recovery absolute permeability, residual oil saturation, interfacial tension and capillary pressure. *Egyptian journal of petroleum* **2017,** *26* (2), 301-312.

180. Chen, J.; Fang, Y.; Gu, R.; Shu, H.; Ba, L.; Li, W., Study on pore size effect of low permeability clay seepage. *Arabian Journal of Geosciences* **2019,** *12* (7).

181. Reed, M. H., Calculation of multicomponent chemical equilibria and reaction processes in systems involving minerals, gases and an aqueous phase. *Geochimica et Cosmochimica Acta* **1982,** *46* (4), 513-528.

182. Wang, Y.; Van Cappellen, P., A multicomponent reactive transport model of early diagenesis: Application to redox cycling in coastal marine sediments. *Geochimica et Cosmochimica Acta* **1996,** *60* (16), 2993-3014.

183. Steefel, C. I.; Tournassat, C., Reactive Transport Modeling of Coupled Processes in Nanoporous Media. *Reviews in Mineralogy and Geochemistry* **2019,** *85* (1), 75-109.

184. Li, Q.; Steefel, C. I.; Jun, Y. S., Incorporating Nanoscale Effects into a Continuum-Scale Reactive Transport Model for CO2-Deteriorated Cement. *Environ Sci Technol* **2017,** *51* (18), 10861-10871.

185. Scheibe, T. D.; Murphy, E. M.; Chen, X.; Rice, A. K.; Carroll, K. C.; Palmer, B. J.; Tartakovsky, A. M.; Battiato, I.; Wood, B. D., An analysis platform for multiscale hydrogeologic modeling with emphasis on hybrid multiscale methods. *Ground Water* **2015,** *53* (1), 38-56.

186. Gharasoo, M.; Centler, F.; Regnier, P.; Harms, H.; Thullner, M., A reactive transport modeling approach to simulate biogeochemical processes in pore structures with pore-scale heterogeneities. *Environmental Modelling & Software* **2012,** *30*, 102-114.

187. Yang, Y.; Wang, M., Upscaling scheme for long-term ion diffusion in charged porous media. *Phys Rev E* **2017,** *96* (2-1), 023308.

188. Meakin, P.; Tartakovsky, A. M., Modeling and simulation of pore-scale multiphase fluid flow and reactive transport in fractured and porous media. *Reviews of Geophysics* **2009,** *47* (3).

189. Reuss, F. F., Sur un nouvel effet de l'électricité galvanique. *Mem. Soc. Imp. Natur. Moscou* **1809,** *2*, 327-337.

190. Wiedemann, G. t., Ueber die Bewegung von Flüssigkeiten im Kreise der geschlossenen galvanischen Säule. *Annalen der Physik* **1852,** *163* (11), 321-352.

191. Alizadeh, A.; Jin, X.; Wang, M., Pore-scale Study of Ion Transport Mechanisms in Inhomogeneously Charged Nanoporous Rocks: Impacts of Interface Properties on Macroscopic Transport. *Journal of Geophysical Research: Solid Earth* **2019,** *124* (6), 5387-5407.

192. Goldberg, S., Use of Surface Complexation Models in Soil Chemical Systems. In *Advances in Agronomy Volume 47*, 1992; pp 233-329.

193. Goldberg, S., Application of surface complexation models to anion adsorption by natural materials. *Environ Toxicol Chem* **2014,** *33* (10), 2172-80.

194. van der Heyden, F. H.; Stein, D.; Dekker, C., Streaming currents in a single nanofluidic channel. *Phys Rev Lett* **2005,** *95* (11), 116104.

195. Kang, Q.; Lichtner, P. C.; Zhang, D., An improved lattice Boltzmann model for multicomponent reactive transport in porous media at the pore scale. *Water Resources Research* **2007,** *43* (12).

196. Joekar-Niasar, V.; Schreyer, L.; Sedighi, M.; Icardi, M.; Huyghe, J., Coupled Processes in Charged Porous Media: From Theory to Applications. *Transport in Porous Media* **2019,** *130* (1), 183-214.

197. Robert J. Hunter, R. H. O., R. L. Rowell *Zeta Potential in Colloid Science: Principles and Applications*. Academic Press: Australia.

198. Yeh, L.-H.; Hsu, J.-P.; Qian, S.; Tseng, S., Counterion condensation in pH-regulated polyelectrolytes. *Electrochemistry Communications* **2012,** *19*, 97-100.

199. Yeh, L. H.; Zhang, M.; Joo, S. W.; Qian, S.; Hsu, J. P., Controlling pH-regulated bionanoparticles translocation through nanopores with polyelectrolyte brushes. *Anal Chem* **2012,** *84* (21), 9615-22.

200. Zhao, H.; Zhai, S., The Influence of Dielectric Decrement on Electrokinetics. *J Fluid Mech* **2013,** *724*, 69-94.

201. Qiao, R.; Aluru, N. R., Ion concentrations and velocity profiles in nanochannel electroosmotic flows. *The Journal of Chemical Physics* **2003,** *118* (10), 4692-4701.

202. Qian, S. A., Y., *Electrokinetic Particle Transport In Micro-/Nanofluidics;*. CRC Press: 2012.

203. Polat, M.; Polat, H., Analytical solution of Poisson-Boltzmann equation for interacting plates of arbitrary potentials and same sign. *J Colloid Interface Sci* **2010,** *341* (1), 178-85.

204. McCormack, D.; Carnie, S. L.; Chan, D. Y. C., Calculations of Electric Double-Layer Force and Interaction Free Energy between Dissimilar Surfaces. *Journal of Colloid and Interface Science* **1995,** *169* (1), 177-196.

205. Stein, D.; Kruithof, M.; Dekker, C., Surface-charge-governed ion transport in nanofluidic channels. *Phys Rev Lett* **2004,** *93* (3), 035901.

206. Wang, M.; Kang, Q., Electrochemomechanical energy conversion efficiency in silica nanochannels. *Microfluidics and Nanofluidics* **2009,** *9* (2-3), 181-190.

207. Tessier, F.; Slater, G. W., Effective Debye length in closed nanoscopic systems: a competition between two length scales. *Electrophoresis* **2006,** *27* (3), 686-93.

208. Yang, R. J.; Fu, L. M.; Hwang, C. C., Electroosmotic Entry Flow in a Microchannel. *Journal of Colloid and Interface Science* **2001,** *244* (1), 173-179.

209. Bhattacharyya, S.; Zheng, Z.; Conlisk, A. T., Electro-osmotic flow in two-dimensional charged micro- and nanochannels. *Journal of Fluid Mechanics* **2005,** *540* (-1).

210. Hart, J., Correction to the Viscoelectric Constant. *The Journal of Chemical Physics* **1958,** *29* (4), 960-961.

211. Lyklema, J.; Overbeek, J. T. G., On the interpretation of electrokinetic potentials. *Journal of Colloid Science* **1961,** *16* (5), 501-512.

212. Hunter, R. J., The interpretation of electrokinetic potentials. *Journal of Colloid and Interface Science* **1966,** *22* (3), 231-239.

213. Stigter, D., On the Viscoelectric Effect in Colloidal Solutions1. *The Journal of Physical Chemistry* **1964,** *68* (12), 3600-3602.

214. Freund, J. B., Electro-osmosis in a nanometer-scale channel studied by atomistic simulation. *The Journal of Chemical Physics* **2002,** *116* (5), 2194-2200.

215. Qiao, R.; Aluru, N. R., Scaling of electrokinetic transport in nanometer channels. *Langmuir* **2005,** *21* (19), 8972-7.

216. Hunter, R. J.; Leyendekkers, J. V., Viscoelectric coefficient for water. *Journal of the Chemical Society, Faraday Transactions 1: Physical Chemistry in Condensed Phases* **1978,** *74* (0).

217. mkBazant, M. Z.; Kilic, M. S.; Storey, B. D.; Ajdari, A., Towards an understanding of induced-charge electrokinetics at large applied voltages in concentrated solutions. *Adv Colloid Interface Sci* **2009,** *152* (1-2), 48-88.

218. Bikerman, J. J., XXXIX. Structure and capacity of electrical double layer. *The London, Edinburgh, and Dublin Philosophical Magazine and Journal of Science* **2009,** *33* (220), 384-397.

219. Storey, B. D.; Bazant, M. Z., Effects of electrostatic correlations on electrokinetic phenomena. *Phys Rev E Stat Nonlin Soft Matter Phys* **2012,** *86* (5 Pt 2), 056303.

220. Celebi, A. T.; Beskok, A., Molecular and Continuum Transport Perspectives on Electroosmotic Slip Flows. *The Journal of Physical Chemistry C* **2018,** *122* (17), 9699-9709.

221. Lyklema, J., On the slip process in electrokinetics. *Colloids and Surfaces A: Physicochemical and Engineering Aspects* **1994,** *92* (1-2), 41-49.

222. Jing, D.; Bhushan, B., Quantification of surface charge density and its effect on boundary slip. *Langmuir* **2013,** *29* (23), 6953-63.

223. Li, Y.; Bhushan, B., The effect of surface charge on the boundary slip of various oleophilic/phobic surfaces immersed in liquids. *Soft Matter* **2015,** *11* (38), 7680-95.

224. Hughes, C.; Yeh, L.-H.; Qian, S., Field Effect Modulation of Surface Charge Property and Electroosmotic Flow in a Nanochannel: Stern Layer Effect. *The Journal of Physical Chemistry C* **2013,** *117* (18), 9322-9331.

225. Trefalt, G.; Behrens, S. H.; Borkovec, M., Charge Regulation in the Electrical Double Layer: Ion Adsorption and Surface Interactions. *Langmuir* **2016,** *32* (2), 380-400.

226. Qian, S.; Bau, H. H., Magnetohydrodynamic flow of RedOx electrolyte. *Physics of Fluids* **2005,** *17* (6), 067105.

227. Sabet, S.; Barisik, M.; Mobedi, M.; Beskok, A., An extended Kozeny-Carman-Klinkenberg model for gas permeability in micro/nano-porous media. *Physics of Fluids* **2019,** *31* (11), 112001.

228. Ozgumus, T.; Mobedi, M.; Ozkol, U., Determination of Kozeny Constant Based on Porosity and Pore to Throat Size Ratio in Porous Medium with Rectangular Rods. *Engineering Applications of Computational Fluid Mechanics* **2014,** *8* (2), 308-318.

229. Mobedi, M.; Barisik, M.; Nakayama, A., 16 Heat and Fluid Flow of Gases in Porous Media with Micropores: Slip Flow Regime. **2016**.

230. Nakayama, A., *PC-aided numerical heat transfer and convective flow*. CRC press: 1995.

231. Zhuravlev, L. T., Surface characterization of amorphous silica—a review of work from the former USSR. *Colloids and Surfaces A: Physicochemical and Engineering Aspects* **1993,** *74* (1), 71-90.

232. Hair, M. L.; Hertl, W., Acidity of surface hydroxyl groups. *The Journal of Physical Chemistry* **1970,** *74* (1), 91-94.

233. Andersen, M. B.; Bruus, H.; Bardhan, J. P.; Pennathur, S., Streaming current and wall dissolution over 48 h in silica nanochannels. *J Colloid Interface Sci* **2011,** *360* (1), 262-71.

234. Beck, J. S.; Vartuli, J. C.; Roth, W. J.; Leonowicz, M. E.; Kresge, C. T.; Schmitt, K. D.; Chu, C. T. W.; Olson, D. H.; Sheppard, E. W.; McCullen, S. B.; Higgins, J. B.; Schlenker, J. L., A new family of mesoporous molecular sieves prepared with liquid crystal templates. *Journal of the American Chemical Society* **1992,** *114* (27), 10834-10843.

235. Kresge, C. T.; Leonowicz, M. E.; Roth, W. J.; Vartuli, J. C.; Beck, J. S., Ordered mesoporous molecular sieves synthesized by a liquid-crystal template mechanism. *Nature* **1992,** *359* (6397), 710-712.

236. Kleitz, F.; Choi, S. H.; Ryoo, R., Cubic Ia3d large mesoporous silica: synthesis and replication to platinum nanowires, carbon nanorods and carbon nanotubes. *Chem Commun (Camb)* **2003,** (17), 2136-7.

237. Zhao, D.; Huo, Q.; Feng, J.; Chmelka, B. F.; Stucky, G. D., Nonionic Triblock and Star Diblock Copolymer and Oligomeric Surfactant Syntheses of Highly Ordered, Hydrothermally Stable, Mesoporous Silica Structures. *Journal of the American Chemical Society* **1998,** *120* (24), 6024-6036.

238. Zhao, D.; Feng, J.; Huo, Q.; Melosh, N.; Fredrickson, G. H.; Chmelka, B. F.; D. Stucky, G. D., Triblock Copolymer Syntheses of Mesoporous Silica with Periodic 50 to 300 Angstrom Pores. *Science* **1998,** *279* (5350), 548-552.

239. Yu, C.; Yu, Y.; Zhao, D., Highly ordered large caged cubic mesoporous silica structures templated by triblock PEO–PBO–PEO copolymer. *Chemical Communications* **2000,** (7), 575-576.

240. Kim, T.-W.; Ryoo, R.; Kruk, M.; Gierszal, K. P.; Jaroniec, M.; Kamiya, S.; Terasaki, O., Tailoring the Pore Structure of SBA-16 Silica Molecular Sieve through the Use of Copolymer Blends and Control of Synthesis Temperature and Time. *The Journal of Physical Chemistry B* **2004,** *108* (31), 11480-11489.

241. Sakamoto, Y.; Kaneda, M.; Terasaki, O.; Zhao, D. Y.; Kim, J. M.; Stucky, G.; Shin, H. J.; Ryoo, R., Direct imaging of the pores and cages of three-dimensional mesoporous materials. *Nature* **2000,** *408* (6811), 449-53.

242. dos Santos, S. M. L.; Nogueira, K. A. B.; de Souza Gama, M.; Lima, J. D. F.; da Silva Júnior, I. J.; de Azevedo, D. C. S., Synthesis and characterization of ordered mesoporous silica (SBA-15 and SBA-16) for adsorption of biomolecules. *Microporous and Mesoporous Materials* **2013,** *180*, 284-292.

243. Narayan, R.; Nayak, U. Y.; Raichur, A. M.; Garg, S., Mesoporous Silica Nanoparticles: A Comprehensive Review on Synthesis and Recent Advances. *Pharmaceutics* **2018,** *10* (3).

244. Knezevic, N.; Mladenovic, M.; Zivojevic, K.; Počuča-Nešić, M.; Vojisavljevic, K.; Savic, S., Hard Template Synthesis of Nanomaterials Based on Mesoporous Silica. *Metallurgical and Materials Engineering* **2018,** *24* (4).

245. Gobin, O. C. SBA-16 Materials Synthesis, Diffusion and Sorption Properties. Laval University, 2006.

246. Brakke, K. A., The Surface Evolver. *Experimental Mathematics* **1992,** *1* (2), 141-165.

247. Saada, M. A.; Chikh, S.; Campo, A., Analysis of hydrodynamic and thermal dispersion in porous media by means of a local approach. *Heat and mass transfer* **2006,** *42* (11), 995-1006.

248. Huang, J.; Sumpter, B. G.; Meunier, V., A universal model for nanoporous carbon supercapacitors applicable to diverse pore regimes, carbon materials, and electrolytes. *Chemistry* **2008,** *14* (22), 6614-26.

249. Huang, J.; Sumpter, B. G.; Meunier, V., Theoretical model for nanoporous carbon supercapacitors. *Angew Chem Int Ed Engl* **2008,** *47* (3), 520-4.

250. Lambert, W. J.; Middleton, D. L., pH hysteresis effect with silica capillaries in capillary zone electrophoresis. *Analytical Chemistry* **2002,** *62* (15), 1585-1587.

251. Kalyoncu, G. Investigation of liquid transport in micro and nanoscale porous media at different pore to throat size ratios. Izmir Institute of Technology, 2017.

252. Bazant, M. Z.; Sabri Kilic, M.; Storey, B. D.; Ajdari, A., Nonlinear electrokinetics at large voltages. *New Journal of Physics* **2009,** *11* (7).

VITA

Tümcan ŞEN

EDUCATION

- Ph.D. in Mechanical Engineering, İzmir Institute of Technology (2021)
- Research Master (RM) in Environmental and Applied Fluid Dynamics, von Karman Institute for Fluid Dynamics (2015)
- M.Sc. in Mechanical Engineering, İzmir Institute of Technology (2014)
- B.Sc. in Mechanical Engineering, Middle East Technical University (2011)

RESEARCH INTERESTS

Core areas of the Thermofluids, Micro/Nano flows, Microfluidics, Electrokinetic Phenomena

LANGUAGE

Turkish (Native), English (Full professional proficiency)

PUBLICATIONS

- Yakin, F.E., **Sen, T.** and Barisik, M., **2020**. Pore Size and Porosity Dependent Zeta Potentials of Mesoporous Silica Nanoparticles. *The Journal of Physical Chemistry C*, 124 (36), pp. 19579-19587.
- **Sen, T.** and Barisik, M., **2020**. Slip Effects on Ionic Current of Viscoelectric Electroviscous Flows through Different Length Nanofluidic Channels. *Langmuir* 36(31), pp. 9191-9203.
- **Sen, T.** and Barisik, M., **2019**. Pore connectivity effects on the internal surface electric charge of mesoporous silica. *Colloid and Polymer Science* 297(10), pp. 1365-1373.
- **Sen, T.** and Barisik, M., **2019**. Internal surface electric charge characterization of mesoporous silica. *Scientific reports* 9(1), p.137.
- **Sen, T.** and Barisik, M., **2018**. Size dependent surface charge properties of silica nanochannels: double layer overlap and inlet/outlet effects. *Physical Chemistry Chemical Physics* 20(24), pp.16719-16728.